Flow of Foams

Katgert, G.

Citation
Katgert, G. (2008, December 11). *Flow of Foams*. *Casimir PhD Series*.
Retrieved from https://hdl.handle.net/1887/13329

Flow of Foams

PROEFSCHRIFT

Ter verkrijging van
de graad van Doctor aan de Universiteit Leiden,
op gezag van de Rector Magnificus
Prof. mr. P.F. van der Heijden,
volgens besluit van het College voor Promoties
te verdedigen op donderdag 11 december 2008
klokke 15.00 uur
door

Gijs Katgert
geboren te Leiden
in 1981

Promotiecommissie:

Promotor: Prof. dr. M.L. van Hecke
Overige leden: Prof. dr. N.D. Denkov (*Universiteit Sofia, Bulgarije*)
                Dr. O. Dauchot (*CEA-Saclay, Frankrijk*)
                Prof. dr. D. Bonn (*UvA, Amsterdam*)
                Prof. dr. ir. W. van Saarloos
                Prof. dr. J.M. van Ruitenbeek
                Prof. dr. P. Kes

"Yon foaming flood seems motionless as ice;
Its dizzy turbulence eludes the eye"

William Wordsworth, *Address to Kilchurn Castle*.

Voor mijn ouders

Contents

CHAPTER 1

INTRODUCTION

An aqueous foam consists of gas bubbles dispersed in water which contains a stabilising agent (surfactant). Despite the simplicity of its composition, the properties of a foam are in general quite complex [1]. The static structure and the ageing of a foam is reasonably well understood, while the behaviour of foams under forcing, i.e. the elasticity and the rheology, has only recently received attention. This is at least partly due to the introduction of the jamming phase diagram [2], which has lead to an upsurge of experimental and theoretical work in the entire field of soft condensed matter physics. The rheology of foams, and of emulsions, which are very closely related to foams but consist of bubbles of an immiscible fluid phase instead of a gas, is expected to obey this jamming picture and the absence of solid friction in both systems would allow for a connection between experiment and simulations.

To investigate foam rheology and connect the bulk behaviour with the motion of the individual bubbles, we will investigate monolayers of foam bubbles which float on the surface of a surfactant solution and which allow for direct imaging of the constituent particles.

However, in order to be able to understand the rheology of foams it is necessary that we first understand the microscopic origin of the rheological properties of individual bubbles. Only then can we try to understand the collective behaviour of collections of these bubbles. The following treatment is focussed on foams, but is equally well valid for emulsions, except for a few details, which are discussed in section 1.4.2.

1

1.1 Microscopics: Foam films, stability

In this section we discuss the chemical components that make up a foam and their influence on the various processes that lead to stabilisation and structural evolution of a foam.

1.1.1 Surfactants and surface tension
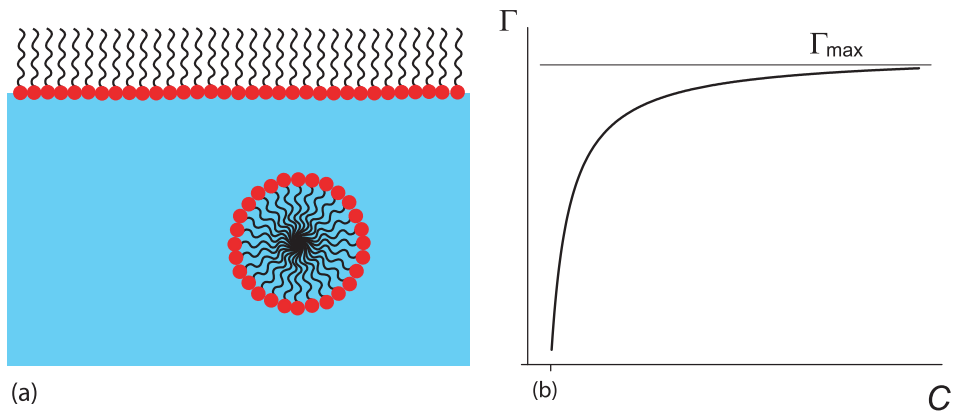
FIGURE 1.1: (a) Surfactant molecules adsorbed at the interface. At the CMC the surface is maximally covered by surfactant molecules and micelles start to form. (b) Langmuir adsorption isotherm, relating the surface concentration Γ to the bulk concentration C [3].

Foam bubbles are generally stabilised against rupture and coalescence by a special class of molecules called surfactants (**surf**ace **act**ive **agents**). These molecules consist of a hydrophilic (polar) head group and a hydrophobic (apolar) tail. When these molecules are dissolved in the water phase they spontaneously adsorb at the interface. The head group sits in the water phase and the tail points towards the oil phase (in case of an emulsion) or the gas phase (in case of a foam). As a result the surfactant molecules lower the surface tension σ of an interface, which can be understood as follows: a surface energy arises because the water molecules at the interface are missing bonds. The liquid seeks to minimise the excess energy associated with these missing bonds and hence minimises its surface area, leading to a surface tension. The surfactants lower the excess
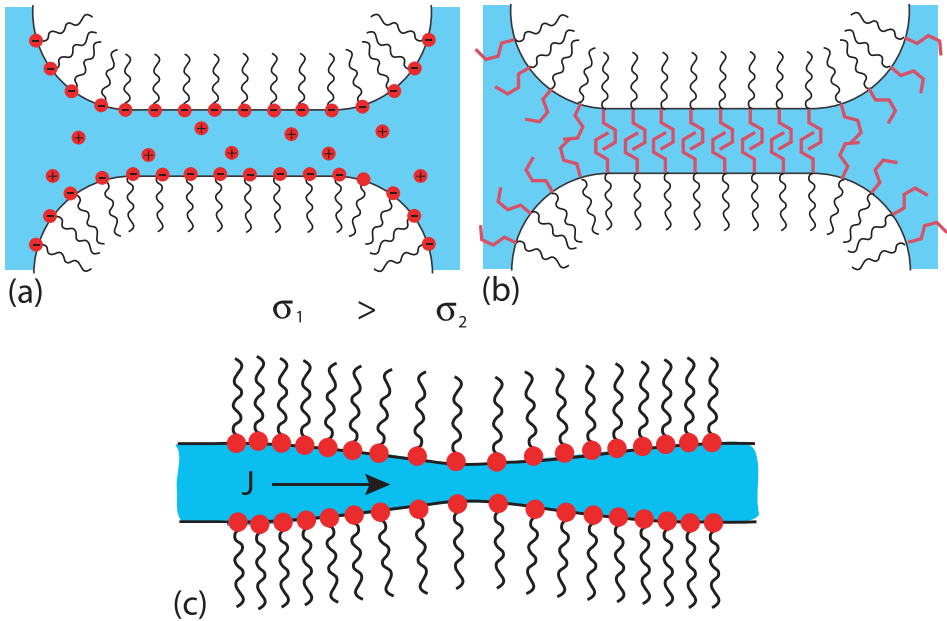
FIGURE 1.2: Static and dynamic foam stabilisation: (a) electrostatic and (b) steric repulsion of the surfactant monolayers provide static foam stabilisation while (c) dynamic stabilisation against fluctuations is guaranteed by the Marangoni effect, which is the coupling between surface tension gradients and flow in the liquid.

energy of missing bonds and hence lower the surface tension.

Besides being polar, the headgroup of a surfactant molecule can be charged or uncharged. Charged surfactants are called *ionic surfactants* and either have a negatively (anionic), a positively (cationic), or both negatively and positively (amphoteric) charged head group. A much used anionic surfactant is Sodium Dodecyl Sulfate (SDS). Uncharged surfactants are called *non-ionic surfactants*. An often used non-ionic surfactant of low molecular weight is polyoxyethylene sorbitan monolaurate, which is better known under its trade name Tween 20. Other important classes of non-ionic surfactants are the synthetic polymeric surfactants such as Pluronic and the natural polymeric surfactants (proteins) such as Bovine Serum Albumin and Casein.

The surface tension σ, the bulk concentration C and the surface con-

centration Γ are related through the Gibbs-Duhem equation for the surface phase [3]:

$$d\sigma = \Gamma k_B T d(\ln C). \tag{1.1}$$

In order to calculate $\sigma(C)$, a model adsorption isotherm is chosen, such as the Langmuir adsorption isotherm shown in Fig. 1.1(b) :

$$\Gamma(C) = \Gamma_{max} \frac{KC}{1 + KC}, \tag{1.2}$$

where K is an adsorption constant. Eq. (1.1) can now be integrated to obtain the dependence of surface tension on bulk concentration.

When increasing the surfactant concentration in the liquid phase (the bulk concentration C), the surface concentration increases according to Eq. (1.1) until the bulk concentration reaches the critical micelle concentration (CMC). By further increasing the bulk concentration, the surfactant molecules form micelles which are spherical shapes or bilayers with the polar heads pointing towards the surrounding liquid and the apolar tails grouped together and shielded against interaction with the fluid by the heads, see Fig. 1.1, in order to minimise binding energy. At the CMC, the chemical potential for surfactants to adsorb at the surface or form micelles is equal and for concentrations above the CMC, the surface concentration can only be increased and hence the surface tension can only be reduced by decrasing the repulsive interaction between the surfactant molecules, for instance by adding electrolyte such that the molecules pack closer at the surface.

The Gibbs surface elasticity, which is in fact a two dimensional elastic modulus (units N/m) and is given by [3]

$$E_G = -\frac{d\sigma}{d(ln\Gamma)}, \tag{1.3}$$

describes the response of the surface tension to variations in the surface concentration. A surfactant layer with a high Gibbs elasticity experiences large changes in surface tension for small variations in surface concentration. Local fluctuations in the surface concentration are energetically strongly unfavourable and result in large stresses. For such a surfactant layer, these fluctuations will mainly be damped by the Marangoni effect, which is the flow of fluid from regions of low surface tension to regions of

high surface tension as a result of the coupling of the surface stress to the fluid below through viscosity.

In order to be able to understand how surfactants stabilise foams we now have to consider the thin soap film between two neighbouring foam bubbles. The thin film consists of two monolayers of surfactant molecules with the bulk phase in between. Both in ionic and in non-ionic surfactants, static stabilisation is achieved by repulsive forces between the surfactant monolayers. For ionic surfactants the repulsive force is electrostatic and is caused by the charged groups at the interfaces , whereas for nonionic surfactants, static stabilisation is achieved by a steric repulsion, which is due to the overlap of the polymer chains, see Fig. 1.2 (a,b).

Dynamic stabilisation against fluctuations in the film thickness is ensured by the Marangoni effect, see Fig. 1.2 (c). If the film locally thins it curves inwards, its area locally increases and the surface tension becomes higher at the dimple but the resulting bulk flow towards the dimple restores the equilibrium thickness. A dimple (thicker region) in the film will by the same mechanism grow further, but the diffusion of surfactant molecules to the dimple will eventually stop this.

1.1.2 Microscopic nature of foam evolution

When no mechanical forcing is applied, foams evolve due to *drainage*, *coarsening* and *coalescence*. Drainage is caused by gravity which leads to a downward flow of the liquid phase, coarsening is caused by gas diffusion between neighbouring bubbles, while rupture of the flat films may cause coalescence between bubbles. We will now discuss how these processes are affected by the constituents of the foam.

Drainage. An increase of viscosity of the liquid phase, for instance by adding glycerol, can help to decrease the drainage velocity, but the speed at which a foam drains is mainly affected by the composition of the surfactants at the interfaces. We have introduced the Gibbs elasticity above, and connected to this we can define a surface elastic modulus as well as a surface viscosity that describe the energy cost of the stretching and shearing of interfaces. These moduli depend on how easily surfactant molecules diffuse from the bulk to the interfaces and vice versa, and the interfaces are either said to be *mobile* (low E_G, ≈ 0 mN/m) or *immobile* (high E_G, ≈ 50 mN/m). A flow of bulk liquid along a soap film couples to the surfactant molecules and results in surface tension gradients. If the film is
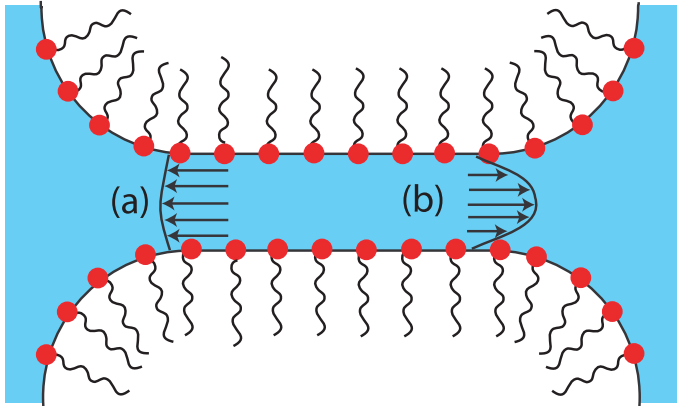
FIGURE 1.3: (a) Plug flow of liquid in thin film due to mobile surfactants: the flow slips with respect to the foam films. (b) Poiseuille flow of liquid in thin film due to immobile surfactants: the liquid experiences a no-slip boundary condition at the foam films and energy is dissipated in the shear flow near the interface.

stabilised by mobile surfactants, an uniform surface tension can easily be restored by diffusion of bulk surfactant molecules to the interface and diffusion on the surface of adsorbed molecules. There is little dissipation at the interfaces and the liquid exhibits plug flow. Immobile surfactants have a far lower diffusivity and resist flow, so the liquid flow velocity decreases steeply close to the interface, resulting in high dissipation and a Poiseuille flow profile. Foams stabilised by immobile surfactants hence drain much slower than foams stabilised by mobile surfactants. At the end of the 90's, a controversy between foam researchers at Harvard [4] and Trinity College [5] in Dublin over the drainage velocity in foams was resolved only when they realised that the different experimental results might well be due to the different dishwashing liquids used. Indeed, it turned out that the American brand Dawn has a lower surface viscosity, which is a quantity that phenomenologically describes the influence of a high Gibb's elasticity in the film, than its European counterpart Fairy (known as Dreft in the Netherlands).

Coarsening. The diffusion of water soluble gasses through the thin soap films separating bubbles leads to coarsening. This is because the capillary pressure inside the smaller bubbles in a foam is higher than in the larger

bubbles (see section 1.2.2), so that gas will mainly diffuse from the smaller to the larger bubbles. As a result, the larger bubbles will grow while the smaller bubbles shrink. A common choice of gas to slow down the coarsening process is C_2F_6, which is almost insoluble in water. A much more soluble but frequently used gas is N_2, which still performs better than air and CO_2 which easily diffuse through the foam films. Note that diffusion by soluble gases can be halted by the addition of only trace amounts of insoluble gases: the soluble gasses easily diffuse from the smaller to the larger bubbles, but since the insoluble gasses remain where they are, the concentration of insoluble gas in the smaller bubbles increases, which quickly leads to a balancing diffusion from the larger to the smaller bubbles to restore the equilibrium in gas concentration between the bubbles. This is the same mechanism that drives osmosis in cells.

Coalescence. Bubbles end their existence by rupture or coalescence with a neighbour. If the films become thin due to drainage, thermal fluctuations will eventually lead to fluctuations in the film thickness that cannot be restored anymore and will lead to rupture of the films. A way to promote rupture is by adding anti-foaming agents to the foam. These consist of oil droplets or solid particles that attach to the thin films and then due to their wetting properties, lead to a retraction of the foam film and hence to rupture. Trying to do the laundry with dishwashing soap will, due to the absence of anti-foaming agents, result in large amounts of foam in and around your washing machine. However, this could be avoided simply by adding some cooking oil.

1.2 Mesoscopics: Shape, Forces and Pressures

In the following section, we will consider the various pressures and forces that are exerted on single bubbles and foam films. We will begin by stating the rules describing a static foam configuration. Then we discuss how bubbles are deformed by compression of other bubbles or by drainage of liquid from the foam, and we discuss the forces that a bubble experiences when it is moving with respect to another bubble or a solid wall. We finally discuss the flotation forces that bubbles experience when floating at an interface, and that hence only apply to two-dimensional foams.
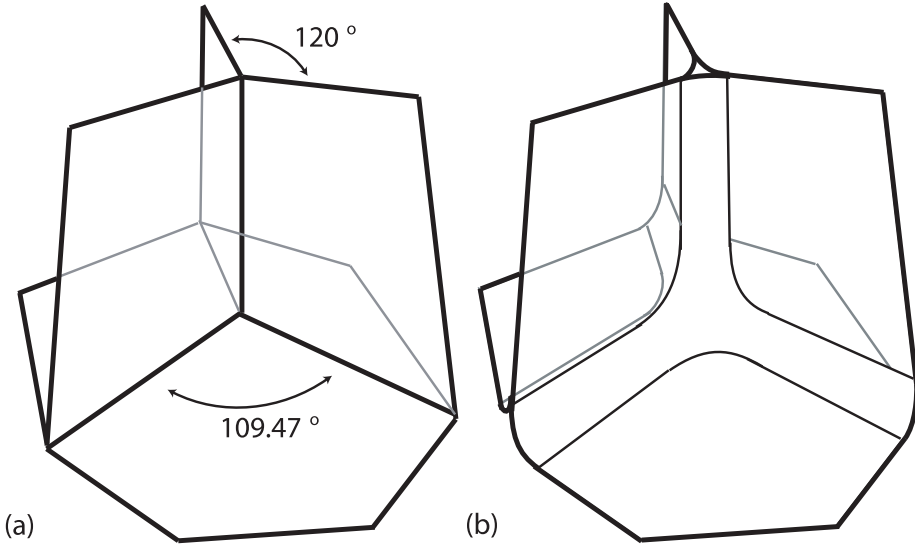
FIGURE 1.4: (a) The first and second rule of Plateau illustrated with a dry foam. Any three soap films meet at 120° angles, while three of such vertices meet in a fourfold node at an angle of 120°. (b) The same view, but for a wetter foam: the Plateau borders are decorated with circular segments .

First we need to introduce the bubble volume fraction ϕ defined as:

$$\phi_l = \frac{V_g}{V_l + V_g}, \tag{1.4}$$

with V_l and V_g are the volumes of liquid and gas respectively. In foam research people often use the liquid fraction $\phi_l = 1 - \phi$ to characterize their foam. Note that we will use the volume fraction ϕ throughout this work, to facilitate the connection with simulation results and granular experiments. A *wet* foam contains a high volume fraction of liquid and the bubbles are only weakly deformed. A typical volume fraction for a commercial three-dimensional foam such as Gilette shaving foam is $\phi = 0.80$. At $\phi = 0.64$ the foam loses its rigidity (unjams) [6, 7] and for yet lower ϕ one speaks of *bubbly liquids*. A *dry* foam consists essentially of a network of thin films and typically $\phi \approx 0.99$.

For three-dimensional foams, this liquid fraction is a well defined quantity. However, both experimentalists and theorists often retreat to two

dimensions [8–12] to study foams. The question is whether a two-dimensional liquid fraction can be defined as well. In numerical studies of two-dimensional foams, where the bubbles are represented by discs, this is no problem. Experimentally, however, this geometry is only achievable with Langmuir foams, which are monolayers of molecules that float at the surface of a liquid and aggregate into two dimensional discs. Due to the simplicity of production and imaging, physicists often prefer to work with monolayers of foam bubbles instead. However, these bubbles extend in three dimensions and since they are more or less spherical, a two-dimensional liquid fraction would strongly depend on the height at which one decides to make a slice through the bubble layer.

In this thesis we describe work performed with two-dimensional foams. We will describe the characterisation of ϕ in quasi two-dimensional foams in much more detail in chapter 4, and we will also show that in order to convincingly explain our findings we have to take into account the physics at the (three dimensional) bubble scale.

1.2.1 Plateau rules

We consider a three dimensional dry foam to establish the geometric rules at equilibrium, see Fig. 1.4(a) which where first described by Joseph Plateau. The first rule states that exactly three soap films always meet at so-called Plateau borders at angles of 120°. The second rule states that four of these Plateau borders meet at nodes under angles of 109.47°. These rules are a direct consequence of the fact that the surface tension of all films should balance at equilibrium. If we consider a two dimensional foam, i.e., a collection of lines that are pulled by surface tension, only Plateau's first rule applies. For slightly wetter foams, Plateau's rules still hold exactly, but the vertices are "decorated" with curved segments that are dictated by the Laplace pressure across the film. For still wetter foams the decorations of the vertices start to overlap and Plateau's rules no longer apply: for example, fourfold vertices become stable [1].

1.2.2 Capillary and Disjoining pressure

The shape of a liquid-gas interface is governed by the Laplace equation, which relates the pressure drop across the interface — which is called the Laplace or capillary pressure — to the surface tension σ and the principal

radii of curvature R_1 and R_2 of the interface:
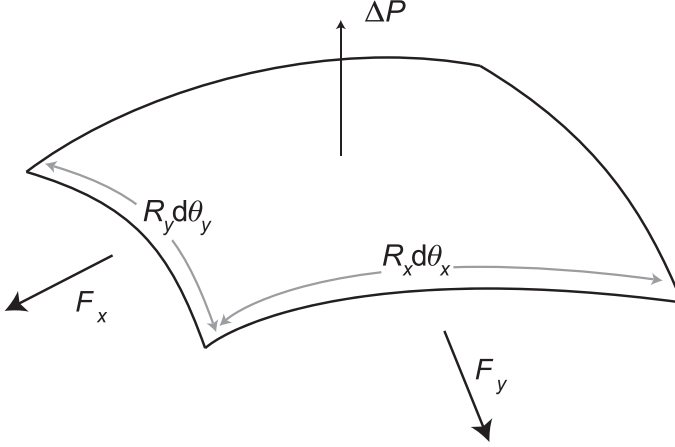
FIGURE 1.5: Illustration of surface element under a pressure gradient. If the surface curves the perpendicular component of the force due to surface tension cancels the pressure gradient.

$$P_c = P_{gas} - P_{liq} = \sigma(\frac{1}{R_1} + \frac{1}{R_2}). \tag{1.5}$$

This equation can be understood by considering an infinitesimally small surface on which surface tension acts and along which a pressure gradient ΔP exerts a force, see Fig. 1.5. The resulting force $\Delta P R_x d\theta_x R_y d\theta_y$ can only be balanced by a surface tension if the surface is curved. In that case the out of plane component of the force due to surface tension balances the pressure gradient.The restoring forces due to the surface tension pulling in the x and y directions are given by:

$$F_x \cdot \sigma \sin d\theta_x = R_y d\theta_y \cdot \sigma \sin d\theta_x \approx R_y d\theta_y \cdot \sigma d\theta_x, \tag{1.6}$$
$$F_y \cdot \sigma \sin d\theta_y = R_x d\theta_x \cdot \sigma \sin d\theta_y \approx R_x d\theta_x \cdot \sigma d\theta_y. \tag{1.7}$$

Balancing the force due to the pressure gradient with the restoring force due to surface tension yields:

$$\Delta P = \frac{F_x + F_y}{R_x d\theta_x R_y d\theta_y}, \tag{1.8}$$

and since $R_x = R_1$ and $R_y = R_2$ we arrive at Eq. (1.5). For a spherical bubble $R_1 = R_2$ and the capillary pressure reduces to:

$$P_c = \frac{2\sigma}{R}. \tag{1.9}$$

The consequence of Eq. (1.9) is that the gas pressure inside bubbles is inversely proportional to their size, which leads to diffusion from the smaller to the larger bubbles. This is the mechanism behind coarsening. An elegant and rigorous derivation of Eq. (1.5) is given in chapter 2 of [3]. A few additional remarks about the radii of curvature are made in Appendix 1.A.

One other pressure plays an important role at gas-liquid interfaces, and to introduce it let us consider a bubble that is pressed against a solid wall by some external force(See Fig. 1.6(a)). A flattened film results, of which we will determine the size as a function of force in Section 2.2.1, and for small deformations the pressure inside the bubble is still determined by the undeformed radius of the bubble:

$$P_{gas} = P_{liq} + P_c = P_{liq} + \frac{2\sigma}{R}. \tag{1.10}$$

At the flattened film the radius of curvature R is infinite and hence the capillary pressure is zero. There Eq. (1.10) cannot hold and a new force comes into play once the distance between the bubble and the wall becomes sufficiently small. At the film this **disjoining pressure** Π, which is a function of the film thickness h, balances the pressure difference across the surface:

$$P_{gas} = P_{liq} + \frac{2\sigma}{\infty} + \Pi(h). \tag{1.11}$$

The disjoining pressure results from the attractive and repulsive forces in the thin film, of which the electrostatic and steric repulsion have already been mentioned. An overview of surface forces that can contribute to the disjoining pressure is given in [13]. For aqueous films the disjoining pressure is often a superposition of electrostatic repulsion and a van der Waals attraction. A typical shape of the $\Pi(h)$ dependence in this case is shown in Fig. 1.6(b). For very short distances a short range Born repulsion is added.

From Eq. (1.11) it is clear that at equilibrium $P_c = \Pi(h)$ so the equilibrium film thicknesses are given by the roots of this equation. As shown in Fig. 1.6(b), there are three equilibrium film thicknesses. At point 1, the
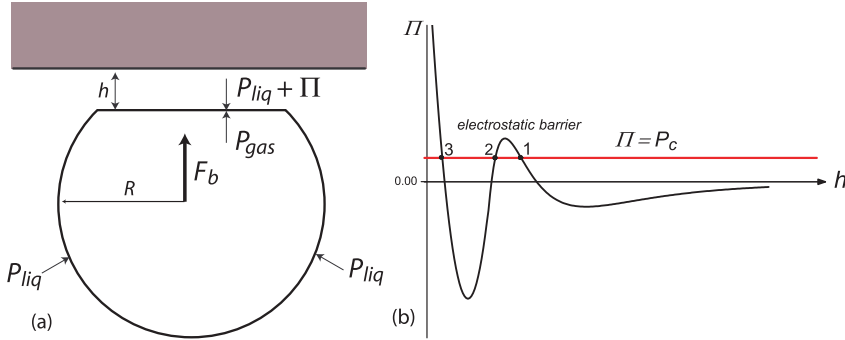
FIGURE 1.6: (a) Pressure balance for deformed bubble, pushed against a solid boundary by buoyancy. At the flattened facet the radius of curvature is ∞ and P_c needs to be balanced by a disjoining pressure Pi. (b) Disjoining pressure isotherm. The horizontal line corresponds to equilibrium film thicknesses. Point 1 and 2 represent *common* and *Newton black film* thicknesses.

film is called *common black film* and there it is stabilised by double layer repulsion. A common black film is defined as being at least thinner than 1/4 of the wavelength of visible light but thicker than 7 nm. Point 2 is an unstable equilibrium and is never observed in experiment and Point 3 corresponds to the *Newton black film*, which is stabilised by the short range Born repulsion. Newton black films are thinner than 7 nm.

1.2.3   Bubble deformation

Bubble deformation by compression

If a bubble is pressed against another bubble or a solid or liquid interface, at equilibrium (or quasi-equilibrium) the driving force is balanced by the disjoining pressure in the resulting thin film [14]:

$$\pi r_c^2 \Pi = F, \tag{1.12}$$

where πr_c^2 is the area of the flat film. Note that at quasi-equilibrium, for a thinning film, this disjoining pressure can also contain a viscous pressure contribution. The liquid and gas pressures cancel when integrated over the bubble surface and do not result in forces. In principle a transversal tension, which is due to the surface tension imbalance at r_c (where

the bubble surface curvature suddenly changes) should be included in Eq. (1.12). However, this tension is generally considered to be negligibly small [3, 14].

In Fig. 1.6(a) the bubble is driven upwards by buoyancy and the force balance reads:

$$\pi r_c^2 \Pi = F = \frac{4}{3}\pi R_0^3 \Delta\rho g, \qquad (1.13)$$

with R_0 the bubble radius, $\Delta\rho$ the density difference between gas and liquid phase and g the gravitational acceleration.

We will now derive an expression for the force on the bubble in terms of measurable quantities such as the bubbles radius R_0, the surface tension σ and the radius of the deformed facet r_c. From Eq. (1.11) we know that for small r_c, such that the gas pressure remains constant, the disjoining pressure Π is balanced by the capillary pressure P_c. We can thus rewrite Eq. (1.12):

$$F = \pi r_c^2 P_c = \pi r_c^2 \frac{2\sigma}{R_0}. \qquad (1.14)$$

In an experimental situation [15, 16] the interparticle force F_{ij}, which is the sum of the forces F_i on particle i and F_j on particle j, can hence be deduced from the size of the flattened film separating the two bubbles pressing against each other by the above reasoning (See Fig. 1.7):

$$F_{ij} = F_i + F_j = \pi r_c^2 \Pi = \pi r_c^2 [(P_c)_i + (P_c)_j] = \pi r_c^2 2\sigma \frac{R_i + R_j}{R_i R_j}. \qquad (1.15)$$

The compressive force can be related not only to the area of the deformed facet, but also to the deformation itself, through a force law. To extract this force law for the bubbles, we can consider the deformation $\delta\xi$ [17], where $\xi = (R_0 - Z)/R_0$ is a dimensionless measure of compression (See Fig. 1.8). For small deformations, to linear order in $\delta\xi$:

$$r_c^2 \approx 2R_0^2 \delta\xi. \qquad (1.16)$$

We can now insert this in Eq. (1.14) and obtain

$$F \approx 4\pi\sigma R_0 \delta\xi. \qquad (1.17)$$

To good approximation, the interaction between bubbles can thus be taken as a repulsive harmonic potential. If a bubble is compressed by many neighbouring bubbles and the deformed surface area becomes large, this approximation breaks down and the interbubble interaction becomes stiffer than harmonic [17].
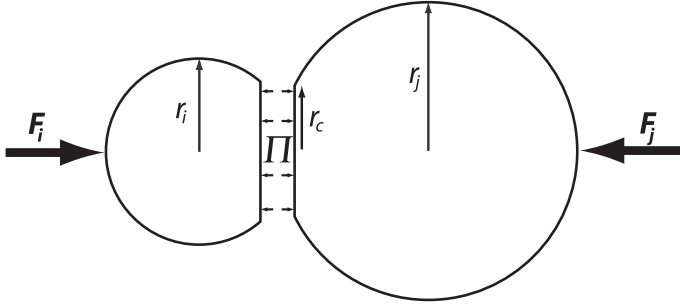
FIGURE 1.7: Illustration of the relation between force on bubbles and deformed facet: the exterted forces F_i, F_j are balanced by the disjoining pressure Π, which can be expressed in terms of the Laplace pressure P_c.

Bubble compressed by buoyancy

If a bubble is trapped under a solid boundary and pushed upwards, and hence deformed by gravity, we can extract r_c by combining Eqs. (1.13) and (1.14), provided that the bubble radius is smaller than the capillary length $\kappa^{-1} = \sqrt{\frac{\sigma}{\rho g}}$. In this case we find:

$$r_c = \sqrt{\frac{2}{3}} \frac{R_0^2}{\sqrt{\frac{\sigma}{\rho g}}} = \sqrt{\frac{2}{3}} \frac{R_0^2}{\kappa^{-1}}. \tag{1.18}$$

However, when the bubble radius is larger than κ^{-1} the bubbles adopt a "pancake" shape with the length of the short axis given by $2\kappa^{-1}$. In that case the contact radius can be found by considering that the bubble volume is conserved after deformation: $\frac{4}{3}\pi R_0^3 = 2\pi r_c^2 \kappa^{-1}$. Hence:

$$r_c = \sqrt{\frac{2}{3}} \frac{R_0^{3/2}}{\kappa^{-1/2}}. \tag{1.19}$$

These scalings were measured to hold approximately in [18] but here we will show they are exact and excellently match experimental data. We measured the contact radius as a function of R_0, by blowing N bubbles of a certain radius R_0. Since the bubbles are not spherical as they float at an interface, we determine this radius by measuring the amount of space they occupy in an upright tube of 1x1x20 cm, see Fig. 1.9(b). We then tilt
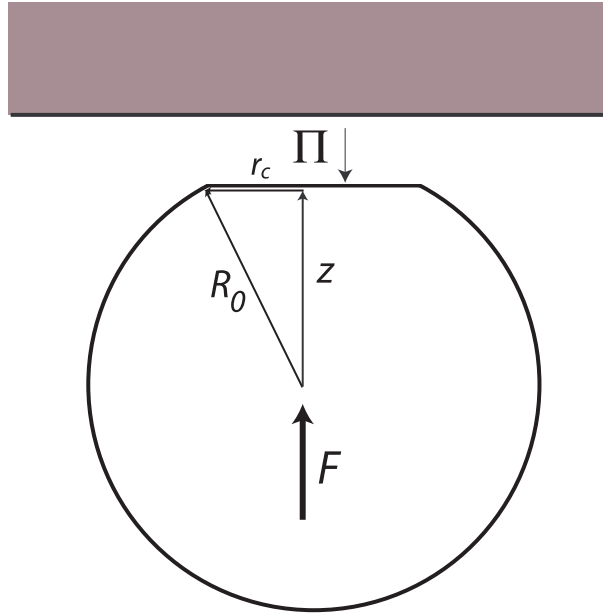
FIGURE 1.8: Pressure balance for deformed bubble: the dimensionless overlap $\xi \equiv (R_0 - z)/R_0$ can be expressed in terms of r_c.

the tube by 90 degrees and measure r_c by looking at the reflection of a light source by the flattened facet. We used Dawn as surfactant, for which we measured $\sigma = 28 \pm 1$ mN.m^{-1}. The results are plotted in Fig. 1.9(a): the theoretical expression fits excellently to the data for $\kappa^{-1} = 1.62 \pm 0.02$ mm, which is within error bars to the result $\kappa^{-1} = 1.64 \pm 0.06$ mm obtained from measuring σ.

Finally we remark that if the density difference between the bubble phase and the liquid phase is small (as can be the case for emulsions), bubbles remain essentially undeformed. This can easily be seen from Eq. (1.18): r_c scales quadratically with bubble radius.

Bubble deformation by drainage

Liquid mainly drains from the foam via the Plateau borders. As a consequence, due to the decreasing liquid fraction, the foam bubbles deform and the Plateau border radius of curvature decreases, see Fig. 1.10, re-
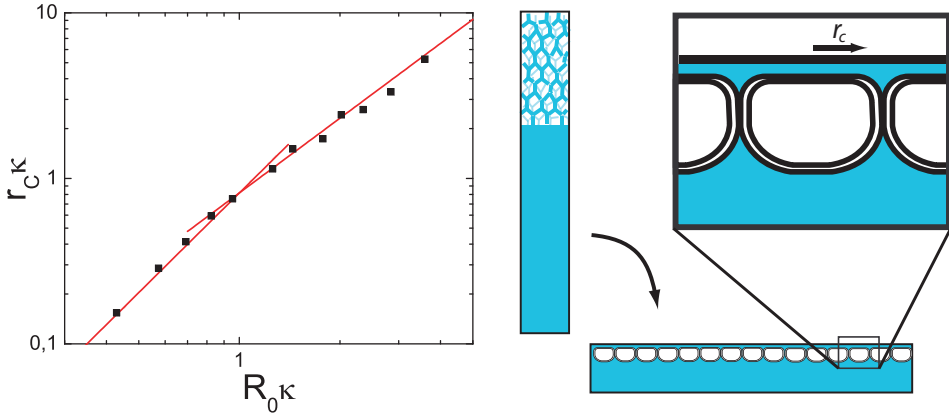
FIGURE 1.9: (a) Measured dependence of the radius of the flattened contact normalised by the capillary length versus the undeformed bubble radius normalised by the capillary length. Solid lines are the theoretical results from Eqs. (1.18) and (1.19) for $\kappa = 1.62$ mm.

sulting in an increase in the capillary pressure. To good approximation, the gas pressure inside the bubbles remains constant and hence the liquid pressure in the Plateau border must decrease to satisfy the Laplace equation. The resulting pressure gradient between the foam films and the Plateau border causes liquid to be sucked from the thin films separating the bubbles, where the liquid pressure is higher, to the Plateau border where the pressure is lower, which leads to thinning.

1.2.4 Viscous drag forces

Bubbles that move with respect to other bubbles or a wall experience viscous drag forces due to the resistance to flow of liquid in the thin films separating the bubble from a neighbour or a wall. This resistance to flow is linked to the concepts of surface elasticity or viscosity we have introduced before. The interaction between a moving bubble and a wall has been extensively studied, both theoretically [19–21] and experimentally [18, 20–22]. The frictional force F_{bw} turns out to scale as:

$$F_{bw} \propto (Ca)^n, \tag{1.20}$$

16
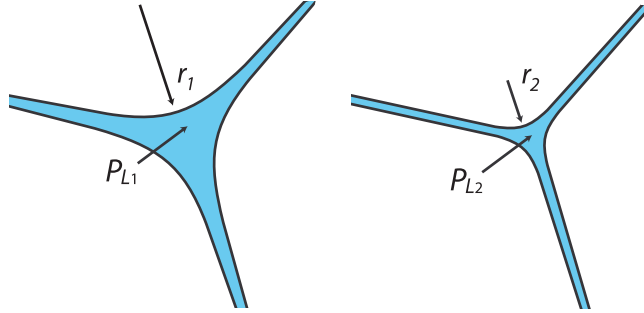
FIGURE 1.10: Due to drainage of the fluid the Plateau border radius of curvature decreases. This leads to a decrease in the liquid pressure and as a result, liquid is sucked from the films, leading to thinning.

with Ca the capillary number, describing the ratio of viscous and surface tension contributions to the force, given by $(Ca) = \eta v/\sigma$, with, η the viscosity, v the relative bubble speed and σ the surface tension. The power law index n depends on the mobility of the surfactants that stabilize the foam films: for mobile bubble surfaces, i.e for bubble surfaces that have very low E_G, $n = \frac{2}{3}$, whereas for immobile surfaces (where E_G is high) $n = \frac{1}{2}$ [20]. The model can be refined further by including the liquid fraction of the foam in terms of the relative size of the deformed film separating the bubble and the wall: r_c/r_{PB}, where PB denotes Plateau border. For all practical purposes though, the viscous drag can be assumed to scale as in Eq. (1.20) with n somewhere between $\frac{1}{2}$ and $\frac{2}{3}$.

The viscous friction between bubbles sliding past each other is much less studied, and is often taken to scale linearly with the velocity difference between bubbles [10, 23]. A theoretical study of the viscous drag in dry monodisperse foams under shear yields a viscous drag force that scales with $Ca^{2/3}$ [24], hinting that the mechanism of viscous dissipation between bubbles that slide past one other is the same as for a bubble slipping past a wall. A very recent theoretical analysis of layers of bubbles in an ordered bcc structure [25], reveals that for immobile foams the viscous

drag force between bubbles scales as:

$$F_{bb} \propto (Ca)^{0.5}. \tag{1.21}$$

We will come back to the scaling of the viscous dissipation in much greater detail in Chapter 2.

1.2.5 Capillary forces on floating bubbles

Bubbles floating at an air/water interface will in general experience lateral forces due to the fact that neighbouring bubbles deform the water surface. The origin and functional form of these forces will be discussed in the next section. The derivation is most easily carried out for solid particles, but is equally valid for foam bubbles and emulsion droplets. The deformation of an interface $\zeta(x, y)$ in the vicinity of a floating particle is due to the requirement that the surface tension balances with gravity while simultaneously the interfacial tensions balance at the three-phase contact line. This requires the liquid phase to meet the particle under a certain angle, which results in a deformation of the surface.

Flotation forces

Two types of lateral capillary forces exist, of which we present an overview in Fig. 1.11: a capillary flotation force, which is caused by the deformation of the liquid interface due to the weight (or buoyancy) of a floating body and a capillary immersion force, which occurs if particles are partially immersed in a liquid layer and which is due to wetting of the particle. Both forces are attractive if the contact angles at the particles are of the same sign, and repulsive if they are of different sign.

Since our particles float at the surface of a deep basin of soapy solution, for our system the only relevant capillary force is the flotation force. To calculate this force we follow [3]. In this book the authors provide an excellent summary of work performed by Kralchevsky and co-workers that expands and refines the approach first taken by Nicholson [26], which is called the *linear superposition approximation (LSA)*.

Consider a particle floating at the interface between two immiscible fluids. The origin is fixed at the particle position. The force due to gravity (which consists of the particle weight as well as buoyant forces) is balanced by the vertical component of the surface tension integrated over the
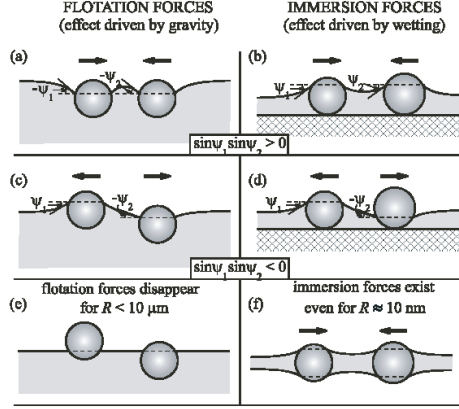
FIGURE 1.11: Flotation and immersion forces compared. Depending on the contact angle, the forces can either be attractive or repulsive. Foam bubbles will always attract, as in (a). *Figure taken from [3].*

three-phase contact (tpc) line, as is shown in Fig. 1.12:

$$F_{g(1)} = 2\pi\sigma r_1 \sin \psi_1, \qquad (1.22)$$

where r_1 i the radius of the tpc line. Now we bring in particle 2 from infinity ($\zeta = 0$) to a distance L, where it is located at $\zeta(L)$ below the horizontal plane due to the meniscus created by particle 1. The work carried out by the gravitational force to bring particle 2 from $z = 0$ down to $z = -\zeta(L)$ is:

$$\Delta W_g = -F_{g(2)}\zeta(L) = -2\pi\sigma r_2 \sin \psi_2 \zeta(L). \qquad (1.23)$$

Introducing the capillary charge $Q \equiv r \sin \psi$ this can also be written as:

$$\Delta W_g = -2\pi\sigma Q_2 \zeta(L). \qquad (1.24)$$

Thus, before we can obtain the force on the particle from W we first have to find an expression for the meniscus deformation around particle 1. This deformation is given by Eq. (1.51) in appendix 1.A:

$$\nabla_{II} \cdot \left(\frac{\nabla_{II}\zeta}{\sqrt{1+ \mid \nabla_{II}\zeta \mid^2}} \right) = [P_2(\zeta) - P_1(\zeta)]/\sigma, \qquad (1.25)$$
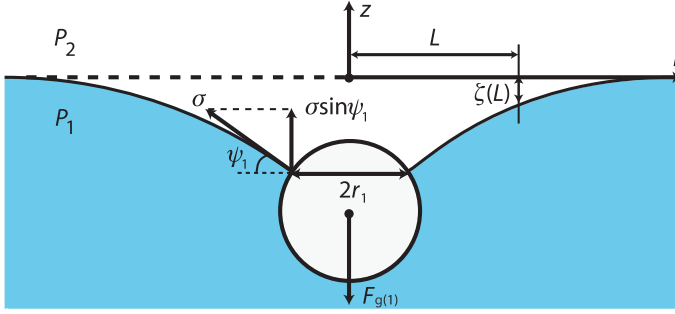
FIGURE 1.12: The force balance for a heavy spherical particle: the force due to gravity acting on the particle is balanced by the vertical component of the surface tension integrated over the three-phase contact line.

with

$$\nabla_{II} \equiv \mathbf{e}_x \frac{\partial}{\partial x} + \mathbf{e}_y \frac{\partial}{\partial y}. \tag{1.26}$$

If the buoyant and gravity forces are considerably smaller than the interfacial tension force, that is, if the Bond number $\rho g R^2 / \sigma < 1$, the surface deformations around the particle are small [27]. In this case $| \nabla_{II}\zeta |^2$ becomes negligible and equation 1.51 reduces to:

$$\nabla^2_{II}\zeta = [P_2(\zeta) - P_1(\zeta)]/\sigma. \tag{1.27}$$

Now the pressures at both sides of the interface ζ can be expressed in the following form [27]:

$$P_1(\zeta) = P_1^{(0)} - \rho_1 g\zeta, \qquad P_2(\zeta) = P_2^{(0)} - \rho_2 g\zeta. \tag{1.28}$$

Here ρ_1 and ρ_2 are the densities of the respective fluid phases, and $P_{1,2}^{(0)}$ are the pressures of the respective fluid phases at $\zeta_\infty = 0$. Inserting 1.28 in 1.27 we end up with:

$$\nabla^2_{II}\zeta = \kappa^2\zeta, \qquad \kappa^2 = \frac{\Delta\rho g}{\sigma}, \qquad \Delta\rho = \rho_1 - \rho_2, \tag{1.29}$$

where $q\kappa$ is the inverse capillary length encountered before, $\kappa = \sqrt{\frac{\Delta\rho g}{\sigma}}$.

If this equation is written in cylindrical coordinates it reduces to the modified Bessel equation, whose solution is for small meniscus slope [28]:

$$\zeta(r) = AK_0(\kappa r) \qquad (1.30)$$

with K_0 a modified Bessel function of zeroth order. The constant A can be determined [29]: $A = r_1 sin\psi_1 = Q_1$ with ψ the three phase contact angle.

Inserting Eq. (1.30) in Eq. (1.24) we end up with

$$\Delta W_g = -2\pi\sigma Q_1 Q_2 K_0(\kappa L). \qquad (1.31)$$

Now, we know that

$$F = -\frac{d\Delta W_g}{dL}; \qquad \frac{dK_0}{dx} = -K_1(x), \qquad (1.32)$$

so the capillary flotation force obeys:

$$F = -2\pi\sigma Q_1 Q_2 \kappa K_1(\kappa L). \qquad (1.33)$$

It is intrinsic to the approximation that the LSA loses its validity for small inter-particle distances. It has been claimed in [30] that the LSA considerably underestimates the capillary attraction. However, recent numerical calculations [28] have shown that for small slope angles, the linear superposition approximation remains valid within 2 % up to particle contact. The authors furthermore show that for many particle systems, the forces are pair-additive.

Dependence of flotation force on particle size

The linearisation of Eq. (1.51) is only allowed if $R_0^2\kappa^2 \ll 1$. This condition is found by equating F_g with the surface tension force, as described above. For an air/water interface $\kappa^{-1} = 2.7$ mm. Furthermore it is shown in section 8.1.2 of [3] that: $Q \propto R_0^3$, with R_0 the droplet radius. Therefore the R_0 dependence for the flotation force is:

$$F \propto (R_0^6/\sigma)K_1(\kappa L) \qquad (1.34)$$

This means that for bubbles close to each other a decrease of the surface tension, for instance by adding surfactant, increases the force. On the other hand the long range force, which is hidden in the Bessel function, then decreases. It also implies the flotation force becomes smaller than kT and thus smaller than the Brownian force for $R_0 < 5$-10 μm.
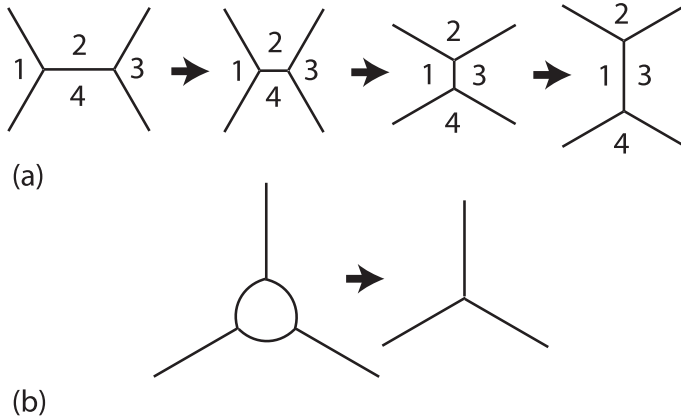
FIGURE 1.13: ((a) T1 process in a 2D foam: the film between bubbles 2 and 4 shrinks to 0, after which the unstable fourfold vertex is resolved by creating a new film between bubble 1 and 3. (b) T2 process in a 2D foam: a small bubble located at the vertex of three larger films disappears due to coarsening.

1.3 Macroscopics: structure, rearrangements and rheology

This section deals with the macroscopic behaviour of a foam under externally imposed stresses or strains. We will explore connections between the micro- and mesoscopic concepts introduced before and the macroscopic behaviour.

1.3.1 Foam structure

If one blows bubbles of one size on the surface of a soapy solution, the bubbles will, due to the flotation forces discussed above, attract and order in a hexagonal packing [31]. A foam consisting of same-sized bubbles is called a monodisperse foam and will order for bubble size variation (polydispersity) up to 10%. For larger polydispersity, a disordered foam results.

In the beginning of Section 1.2 we briefly discussed the volume fraction ϕ. For a two-dimensional hexagonal packing of discs, the jamming or rigidity loss point is at $\phi = 0.909$ [32]. A disordered disc packing, however,

jams at $\phi = 0.842$ [33]. Although in real foams bubbles mutually attract and are three-dimensional objects, we include these numbers here to highlight the structural differences between ordered and disordered foams.

A three-dimensional disordered foam unjams at $\phi = 0.64$, but a three-dimensional monodisperse foam will again form crystalline lattices at much higher volume fractions, depending on the lattice structure, which can be either FCC or BCC [34].

1.3.2 Structural rearrangements and visco-elastic behaviour

The response of a bubble to deformations and the viscous dissipation between two bubbles during flow was discussed in section 1.2. How these forces at the bubble scale translate to the bulk scale is largely unknown and constitute the focus of this thesis, but as a result of the interplay of these nonlinear interactions and the disordered flow of the foam, the bulk response of a foam is highly nontrivial. For small applied strains, bubbles want to restore their equilibrium surface area, and foams respond elastically, i.e.like a solid [1]. If the strain is increased the foam deforms plastically: it relaxes the stresses through bubble rearrangements [1, 32]. For large and continuously applied strains, the foam flows irreversibly with bubbles rearranging continuously [35, 36]. The flow of foams is often measured in oscillatory rheological measurements [7, 37, 38] and fit to certain flow models, which we will describe in the following section.

For a dry foam the bubble rearrangements through which a foam flows are well defined, and two elementary topological processes have been identified that drive the structural evolution of the foam: the T1 and T2 processes, see Figs. 1.13(a)+(b). A T1 process denotes the neighbour swapping of bubbles and is most easily explained for a two dimensional foam, see Fig. 1.13(a): the facet between bubbles 2 and 4 shrinks to zero, resulting in a fourfold vertex. In such a vertex the surface tensions cannot be stably oriented; this instability is resolved with the creation of a new facet between bubble 1 and 3. The T2 process corresponds to the disappearance of a small bubble located at a vertex due to coarsening, see Fig. 1.13(b), and is hence not connected to stress induced evolution of the foam. For wet foams, topological rearrangements seem less well defined, although attempts have been made to treat wet foams within this picture of topological rearrangements by simply considering a wet foam as a dry foam, the vertices of which are decorated with circular arcs [32, 39]. It remains

an open question whether considering the flow of foams entirely through T1 processes is a valid tool for realistic, experimental foams.

Elastic, viscous and visco-elastic response

For an elastic medium, the shear stress τ and the shear strain γ are related through:

$$\tau = G\gamma, \tag{1.35}$$

with G the shear modulus. For a fluid that is sheared between two plates with a strain rate $\dot{\gamma}$ the relation between stress and strain reads:

$$\tau = \eta\dot{\gamma}, \tag{1.36}$$

with η the viscosity.

As was discussed before, foams exhibit both solid and liquid properties and are hence said to be visco-elastic materials. The simplest way to describe this visco-elastic behaviour in terms of a relation between the strains and the stresses is by simply combining both expressions for the stresses. The two simplest procedures to do so are due to Kelvin and Maxwell and are obtained by modeling the elastic response by a spring with stiffness G and the viscous response by a dashpot, characterized by η. In the Maxwell model the spring and the dashpot are placed in series and since the total strain is the sum of the strains on the dashpot and spring, we can write:

$$\gamma = \gamma_1 + \gamma_2 = \frac{\tau}{G} + \frac{\tau}{\eta} \cdot t. \tag{1.37}$$

The Maxwell model captures the behaviour of a fluid under a step stress, with an instaneous elastic response plus a permanent creep flow.

The Kelvin model models a different kind of response and can thus be applied to different systems. In this model, the spring and the dashpot are placed in parallel and this time the stresses over each element are added up, resulting in:

$$\tau = \tau_1 + \tau_2 = G\gamma + \eta\dot{\gamma}. \tag{1.38}$$

More complex models involve many springs and dash-pots, can deal with both step stresses and step strains and are used to model more realistic systems [40–43].

Rheometry and complex shear modulus

If one is interested in the rheological response of a viscoelastic medium over a wide range of time scales, sweeping a periodically varying strain over many decades in frequency yields the desired information, as opposed to imposing a step strain or step stress as in the models discussed above. Imposing a periodically varying strain:

$$\gamma = \gamma_0 \sin \omega t \tag{1.39}$$

yields a stress:

$$\tau = \tau_0 \sin(\omega t + \delta). \tag{1.40}$$

The phase shift δ can be understood by considering the response of purely elastic material, for which $\delta = 0$, and that of a viscous fluid for which:

$$\tau = \eta \dot{\gamma} = \eta \gamma_0 \omega \cos \omega t = \tau_0 \sin(\omega t + \frac{\pi}{2}), \tag{1.41}$$

hence $\delta = \frac{\pi}{2}$. For a visco-elastic material, the phase-shift will be somewhere between 0 and $\frac{\pi}{2}$ and the stress can be written as:

$$\tau = \tau_0 \sin(\omega t + \delta) = (\tau_0 \cos \delta) \sin \omega t + (\tau_0 \sin \delta) \cos \omega t. \tag{1.42}$$

This shows that there are two components to the stress, one in phase with the deformation and one with a phase difference of 90°. One then defines the *storage* and the *loss* modulus G' and G'' as:

$$G' = \frac{\tau_0}{\gamma_0} \cos \delta \equiv G_0 \cos \delta, \tag{1.43}$$
$$G'' = G_0 \sin \delta \tag{1.44}$$

and write the stress as:

$$\tau = \gamma_0 (G' \sin \omega t + G'' \cos \omega t). \tag{1.45}$$

The storage modulus G' is the amplitude of the in-phase component of the response and is a measure of the energy that is reversibly stored in the material, hence the elastic energy, while the loss modulus G'' is the out-of-phase component and denotes the viscous dissipation per oscillation. Writing the strain as $\gamma = \gamma_0 \exp(i\omega t)$, the complex shear modulus becomes:

$$G^* = G' + iG''. \tag{1.46}$$

Constitutive equations

Rheometrical data are often fit to constitutive equations. For Newtonian fluids, the constitutive equation is simply Eq. (1.36). However, to account for the solid-like behaviour, foam rheology is often fit to the Bingham model [44], which accounts for the experimentally observed fact that below a certain stress, called the yield stress, the foam does not flow but responds elastically. The Bingham model reads:

$$\tau = \tau_Y + \mu\dot{\gamma}, \tag{1.47}$$

with τ_Y the yield stress and μ the consistency. The model has a linear dependence of the stress with the strain rate, like a Newtonian fluid.

The Herschel-Bulkley model [45]is similar to the Bingham model, but allows for a non-linear scaling of the viscosity:

$$\tau = \tau_Y + \mu\dot{\gamma}^n. \tag{1.48}$$

If $n > 1$ the material exhibits *shear-thickening* behaviour, that is, it becomes more viscous the faster its driven. On the other hand, if $n < 1$, as is the case for foams [20, 46, 47], the material is *shear-thinning*: it flows more easily for higher driving rates. While the inclusion of a yield stress term in a constitutive equation describing foam rheology appears to be a natural way to describe the elastic response of the system, a microscopic justification for linear or non-linear scaling of the foam viscosity is at present lacking.

1.4 Experiments and numerics on foams and emulsions

1.4.1 Experiments

The first experiments on foam and emulsion rheology stem from the eighties, and since then physicists have mainly studied the rheology of three-dimensional foams and emulsions in Taylor-Couette geometries [32, 35, 38, 46, 48–51]. While these measurements have shed light on the highly non-trivial bulk properties of foams and emulsions, relationships between bulk rheology and behaviour at the bubble scale remained elusive. Recent results, obtained using novel imaging techniques such as DWS [52]

x-ray tomography [53] and confocal microscopy [15, 16] start to elucidate this highly non-trivial connection between local and bulk scale. However, many questions remain unanswered, and we hope these can be addressed by performing experiments on two-dimensional foams. An overview of two-dimensional foam flow experiments is given in chapter 2.

1.4.2 Numerics

The numerical modeling of foam statics and rheology is carried out using a wide variety of techniques, all of which capture part of the rheological behaviour. One of the first simulations was carried out with the PLAT code [33], in which a foam is constructed by creating a Voronoi tessellation and relaxing it to equilibrium, all the while satisfying the Laplace pressure equation for each bubble. The wetness is varied by repeating this procedure while replacing the vertices by circular arcs, and finally this foam of variable wetness is sheared. The strain is increased in small increments and the foam is allowed to relax to static equilibrium between each increment. Such a foam is said to be in the *quasistatic limit*.

The structure of a dry foam can be generated by the surface minimisation routine Surface Evolver, developed by Ken Brakke [54], which is intrinsically quasistatic and which can be adapted to simulate shear flow of dry foams. The vertex model [55] is also limited to dry foams, since it models the Plateau-borders as straight lines, but it includes a linear viscous dissipation in the foam films. The viscous froth model [56], developed recently, can be implemented either in the Surface Evolver framework or in the PLAT code to explicitly describe the presence of confining glass plates through a viscous drag force acting on the entire Plateau border.

The soft disc or bubble model [23, 57, 58] focusses on wet foam behaviour, as it models foam bubbles as spheres that repel each other harmonically and experience a viscous drag proportional to their velocity difference when sliding past each other. It predicts a Bingham behaviour for the rheology and since ϕ can be varied, it uncovers non-trivial scaling of the bulk and shear moduli B and G with ϕ.

Finally, the cellular Potts model [59], in which bubbles are represented by patches of numbers that obey certain rules involving the numerical values of neighbouring patches, is well suited to simulate coarsening in dry foams [60] and has in a few instances been modified to accomodate

the simulation of shear flow [61].

These simulation techniques can each be used to model only parts of the foam behaviour encountered in experiment. For instance, the distribution of stress drops in bubble raft experiments has been found to be in agreement with predictions made in the bubble model [8]. Foams simulated as a collection of vertices — i.e a dry foam — in a Couette geometry display shearbanding, both in quasistatic [62] simulations and in viscous froth [11] simulations, similar to the flow behaviour observed in experimental dry foams. In the viscous froth simulation, however, the exerted rate of strain determines the location of the shearband (and hence of the T1 events): for infinitely slow shear the T1's are located at the cylinder that is not rotated whereas for higher strain rates the T1's are located close to the rotating cylinder.

1.4.3 Differences between foams and emulsions

While emulsions and foams share many properties, these systems exhibit a few differences, which we will now discuss At the smallest scale, the interfacial rheology of the adsorbed monolayers of soap molecules is different because the fluid inside emulsions droplets can flow, hence dissipating energy [3], whereas in foams the air inside bubbles does not dissipate energy.

Furthermore, experimentally three-dimensional emulsions can be made in such a way that they transmit light by index matching the bulk and the dispersed liquid [15, 16]. As a result, the three-dimensional structure can be probed directly with confocal microscopy. In addition, emulsion droplets can also be density matched with the bulk fluid to eliminate of the effects of gravity.

The main difference between emulsions and foams is due to the size of the constituent particles: as a result of the way emulsions are produced, and to meet stability requirements, emulsion droplets are often in the micrometer size range, resulting in Brownian motion. At that scale emulsion systems are most directly related to colloidal systems: for instance, they undergo a glass transition at $\phi = 0.58$ [46]

A phenomenon which occurs in emulsions is flocculation: in absence of a confining pressure, emulsion droplets still deform and form extended connected conglomerates called flocs, due to long-range attractive forces, caused by depletion attractions [63]. Whether such a depletion attraction

might exist in foams stabilised with surfactant solutions well above the CMC is an open question. Finally a few remarks about differing jargon between emulsions and foams: Coarsening is often called *Ostwald ripening* in emulsions. Drainage is referred to as *creaming*.

Appendix 1.A Laplace equation of capillarity

The shape of a liquid surface is governed by the Laplace equation of capillarity, written here in Cartesian coordinates:

$$\frac{(1+\zeta_y^2)\zeta_{xx} - 2\zeta_{xy}\zeta_x\zeta_y + (1+\zeta_x^2)\zeta_{yy}}{(1+\zeta_x^2+\zeta_y^2)^{3/2}} = [P_2(\zeta) - P_1(\zeta)]/\sigma, \qquad (1.49)$$

where ζ_i denotes derivatives with respect to the i-th coordinate, P_j is the pressure of phase j and σ is the interfacial tension. A very elegant derivation of (1.49) is given in chapter 2 of [3]. Writing the left hand side of (1.49) more elegantly we arrive at:

$$2H\sigma = P_2(\zeta) - P_1(\zeta) \qquad (1.50)$$

with H given by:

$$H \equiv \nabla_{II} \cdot \left(\frac{\nabla_{II}\zeta}{\sqrt{1+ \mid \nabla_{II}\zeta \mid^2}} \right), \qquad (1.51)$$

$$\nabla_{II} \equiv \mathbf{e}_x \frac{\partial}{\partial x} + \mathbf{e}_y \frac{\partial}{\partial y}. \qquad (1.52)$$

H is a basic quantity in differential geometry called the *mean curvature*. This quantity can also be expressed through the principle radii of curvature of the surface R_1 and R_2:

$$H = -\frac{1}{2}\left(\frac{1}{R_1} + \frac{1}{R_2} \right). \qquad (1.53)$$

Inserting this in (1.50) we recover the familiar form of the Laplace equation:

$$\sigma \left(\frac{1}{R_1} + \frac{1}{R_2} \right) = P_2(\zeta) - P_1(\zeta). \qquad (1.54)$$

LINEAR SHEAR OF TWO DIMENSIONAL FOAMS

In this chapter, we first review recent research on the rheology of two dimensional foams. We then describe experiments to unravel the connection between local and global behaviour in a two-dimensional foam. To this end we have focused on average velocity profiles in ordered and disordered two-dimensional foams which are covered by a glass plate, and which are linearly sheared. We show that the shape of these profiles can be understood by a model that takes into account viscous dissipation at the bubble scale. We verify our claims by rheometrical measurements. Our results strongly suggest that disorder leads to anomalous scaling of the drag forces: for bidisperse two-dimensional foams, the functional form of the averaged dissipation between bubbles differs markedly from the dissipation between two bubbles moving with constant speed with respect to each other.

2.1 Overview of the field

Experimentally, the rheology of three-dimensional foams (and emulsions) has been studied extensively, mainly in oscillatory strain ([37] and references therein), but recently, the rheology of monolayers of foam bubbles has received increasing attention [8, 9, 12]. Three experimental configurations can be encountered in the literature: the *bubble raft*, see Fig. 2.1(a) where bubbles float freely at the surface of a soapy solution [31], a liquid-
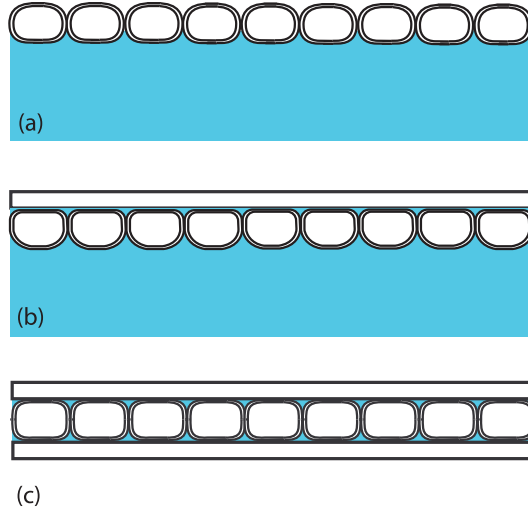
Figure 2.1: Various geometries used in (quasi) two-dimensional foam rheology experiments: (a) freely floating bubble raft, (b) bubble layer confined between liquid surface and glass plate, (c) Hele-Shaw cell: bubble layer confined between two glass plates.

glass setup where bubbles are sandwiched between a glass plate and the surface of the soapy solution [64,65], see Fig. 2.1(b) and the *Hele-Shaw cell*, see Fig. 2.1(c), where bubbles are squashed between two glass plates [9].

These configurations have a number of advantages over three-dimensional systems. First, drainage is absent since the systems extendo only in a horizontal plane. Second, in contrast to three-dimensional foams, which are opaque and which one can only probe with diffusive wave scattering [37] and X-ray tomography [53], the position of all bubbles can be tracked at all times. By doing so, one can investigate the connections between the behaviour of the individual bubbles and the global flow.

In what follows we will describe experiments on the rheology of two-dimensional foams, and therefore we will first discuss recent literature on the rheological behaviour of the above-mentioned systems.

The determination of the static, elastic properties of two dimensional foams, such as the scaling of the shear moduli with packing fraction, is largely an unexplored terrain, even though much theoretical effort has been devoted to precisely that part of foam physics [1]. Instead, experi-

mentally, various groups have looked at shear startup and steady flow of two dimensional foams [8, 9, 12, 66, 67]. The analysis of such experiments comprises for a large part of a host of different statistical measures such as the distribution of stress drops [8, 36, 71], statistical properties of bubble motions such as velocity fluctuations [9, 68] and the spatial distribution of T1 events [66, 69, 70]. While each experiment was analysed in a different way, in all experiments averaged velocity profiles have been measured. Due to the variation in experimental geometries that have been employed, connecting results remains difficult, as we will discuss in the next section.
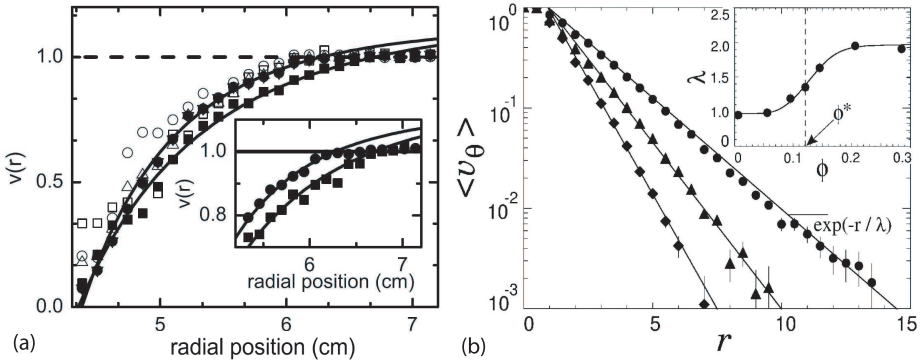
FIGURE 2.2: (a) Velocity profiles of bubble raft in Couette geometry (outer cylinder rotating) for 2 different rates of strain: $\Omega = 5 \times 10^{-3}$ (■) and $\Omega = 8 \times 10^{-4}$ (●). Inset zooms in on region of discontinuity. Open symbols are not relevant in our discussion (Figure reproduced from [68]). (b) Velocity profiles for bi-disperse foam between two glass plates (inner cylinder rotating): $\phi = 0.95$ (◆), $\phi = 0.85$ (▲), $\phi = 0.80$ (●). Profiles are fitted with $\exp(-r/\lambda)$, the inset shows variation of λ with $1 - \phi = \phi_l$ (Figure reproduced from [9].)

Velocity profiles

The flow of foams has been studied in a Taylor-Couette geometry, which consists of two concentric cylinders with the foam in between, in both the Hele-Shaw [9] and bubble raft [8, 68] configuration. Lauridsen, Twardos and Dennin [8, 68, 71] drove a polydisperse bubble raft by a rotating outer

cylinder at low strain rates and measured the averaged velocity profile of the foam and the stress on the inner cylinder as a function of strain rate. The averaged velocity profile exhibits a discontinuity in the strain rate, see Fig. 2.2(a): away from the outer (driving) wheel the azimuthal velocity is constant and equal to the angular velocity of the outer cylinder, until at some $\dot{\gamma}$-dependent critical radius r_c the velocity profile discontinuously starts decaying. The decaying part was well fitted by with a velocity profile expected for a Herschel-Bulkley fluid, for which we repeat the constitutive relation here

$$\tau = \tau_Y + \mu\dot{\gamma}^n, \tag{2.1}$$

The authors find $n = 0.45$ for $\Omega = 8 \times 10^{-4}$ and $n = 0.33$ for $\Omega = 5 \times 10^{-3}$ [68]. In this experiment, the packing fraction ϕ was fixed at 0.9.

Debrégeas, Tabuteau and Di Meglio sheared a bidisperse foam in a Hele-Shaw cell at low strain rates (within a velocity range in which the shape of the velocity profiles was found to be independent of the strain rate). Away from the driving cylinder, the azimuthal velocity was seen to decay exponentially. The authors also varied the liquid content in the cell, and hence ϕ, and observed the localisation length to grow for decreasing packing fraction, see Fig. 2.2(b).

Although both systems are similar in that the distribution of T1 events is proportional to the gradient $\frac{\partial v_\theta}{\partial r}$ [62, 68], the differences between the experiments, such as the discontinuous versus continuous velocity profiles, are more pronounced. This is surprising, since both experiments are performed at low rotation velocity and the experimental setups are very similar, apart from the upper and lower boundaries.

Recent developments

We try to understand the rheology of foams through measurements of averaged velocity profiles. Some recent papers have guided our thoughts on this subject. It has long been stated that, if one is measuring at sufficiently low strain rates and the associated timescale is slower than all kinematic relaxation times, the presence of confining boundaries, such as in the Hele-Shaw cell, should not matter. In this regime the experiments were said to be performed in the *quasistatic limit* [9, 66, 72, 73]. The rate independence of the velocity profiles at low strain rates was then invoked as proof that the system was in this limit. In a recent paper, however,

(a)

(b)
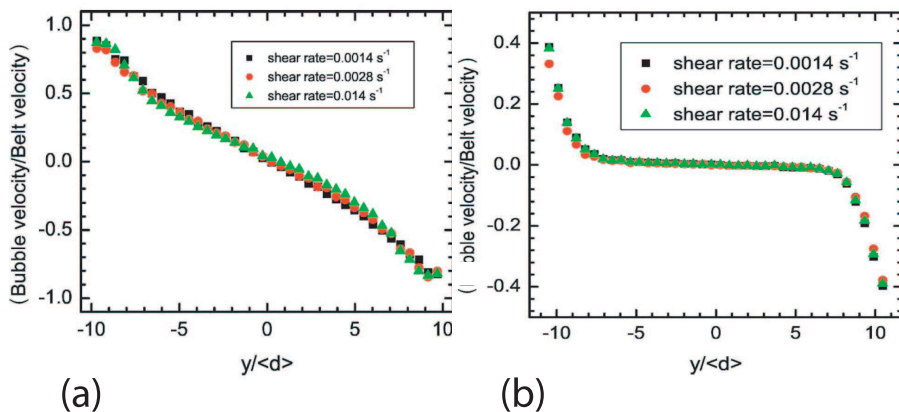
FIGURE 2.3: (a) Averaged velocity profiles for linearly sheared bubble raft, rescaled by driving velocity. (b) averaged velocity profiles for linearly sheared foam layer between glass plate and liquid, rescaled by driving velocity. Note the slip with respect to the driving bands. Figures reproduced from [66].

the influence of these boundaries on the shape of velocity profiles in shear flows of two-dimensional foams has been examined [66]. A mono-disperse foam at fixed ϕ_l was sheared linearly by two counter-propagating conveyor belts. The foam layer was either floating freely or confined between a glass plate and the liquid surface. For both geometries, the resulting velocity profile exhibits rate independence, but its shape is strongly dependent on the boundary: for the bubble raft, the averaged velocity profile is quasi-linear, see Fig. 2.3(a), resembling plane-Couette flow of Newtonian liquids, but the confined foam shows exponentially decaying shear bands, see Fig. 2.3(b). We have already seen that the flow of bubbles along a solid boundary (the top plate) leads to dissipation, and this apparently influences the dynamics of the bubbles.

An analytical model, taking into account this viscous friction with respect to a boundary, is proposed in [10]. The foam is described as a Bingham fluid experiencing a frictional body force which depends linearly on the velocity, allowing for analytical treatment of the problem. The result-

ing stress balance reads as follows:

$$\beta v = \frac{\partial}{\partial y} \left(\tau_Y \tanh(\gamma/\gamma_Y) + \eta \dot{\gamma} \right), \tag{2.2}$$

with a strain dependent yield stress τ_Y that saturates at the yield strain. For large strains (or steady shear) and relatively high strain rates the velocity profiles converge to exponential decay, but for vanishing friction coefficient (i.e in the case of a bubble raft) the decay length is of the order of the system size and the flow profile closely resembles a Newtonian flow profile. The exponentially decaying velocity profiles in the case of an additional wall drag can hence be understood as a result of the balance of the body force (the wall drag exerted on the foam bubbles) with enhanced gradients in the local velocities, resulting in gradients in the local strain rate.

2.2 Linear shear of two dimensional foams

We induce a linear shear flow in a two-dimensional foam. We record averaged velocity profiles and by fitting these profiles to solutions of a drag force balance model we can investigate the viscous stresses inside the foam. The scaling with strain rate of these viscous stresses can be compared to the scaling of the local bubble drag, as well as with the global flow curve, though rheometry.

2.2.1 Experimental details

We create a bidisperse monolayer of foam bubbles of 1.8 and 2.7 mm diameter on the surface of a reservoir of soapy solution, consisting of 80% by volume demineralized water, 15% glycerol and 5% Blue Dawn dishwashing agent (Proctor & Gamble), by bubbling nitrogen through the solution via syringe needles of variable aperture. We measure the bath surface tension σ with the pendant drop method [74] and find $\sigma = 28$ mN/m. We measure the dynamic viscosity η with a Cannon Ubbelohde viscometer and find $\eta = 1.8$ mPa.s.

Setup

The bubbles are contained inside an aluminum frame (400 x 230 mm) which can be leveled with the liquid surface and can support the glass boundary to which the bubbles bridge once it is in place. The glass boundary consists of 3 glass plates with slits to accommodate two PMMA wheels of radius 195 mm and thickness 9.5 mm. The gap between the liquid surface and the glass plates is fixed at 2.25 ± 0.01 mm, such that the packing fraction is fixed. We will show in chapter 4, that for this gap the packing fraction is $\phi = 0.965 \pm 0.005$. The wheels, which are grooved to provide a no-slip boundary for the bubbles, can be lowered into and raised out of the solution through the slits. The wheels are connected to two Lin Engineering stepper motors, each driven by microstepping driver, and are rotated in opposite directions. As a result, the layer of bubbles is sheared with a driving velocity $v_0 = \omega r_0$ in the plane of the bubbles, see Fig. 2.4(b). At any point along the line where the wheels contact the foam bubbles the horizontal component of the driving velocity is given by $v_0 = \omega r_1 \cos \phi$. But $r_1 = \frac{r_0}{\cos \phi}$ and hence $v_0 = \omega \frac{r_0}{\cos \phi} \cos \phi = \omega r_0$ and the foam is driven with this velocity all along the contact line of 230 mm, see Fig. 2.4(b).

No motion is observed due to the vertical component of the radial velocity, although bubbles do leave the system, while being pinned to the wheels, at the edges of the slits. However, no holes are produced in the two dimensional foam layer as a result of this, either because at high driving velocities the bubbles reenter the system before rupturing while traveling on the wheel, or because at low velocities bubbles from outside the shearing region are pushed inwards due to the bubble surplus at the edges. The resulting driving velocity gives rise to a global strain rate $\dot{\gamma} = 2v_0/W$, where W denotes the gap between the wheels, which can be varied between 5 and 10 cm.

Imaging and Analysis

The velocity profiles are obtained from images which we record by a Foculus BW 432 CCD camera equipped with a Tamron 28-300 telezoom objective. A typical image is shown in Fig. 2.5. To improve the brightness and obtain images in which the bubbles are represented by circles (see Fig. 2.4(c) for an example), the foam is lit laterally by two fluorescent tubes, each driven by high frequency ballasts to prevent flickering in the
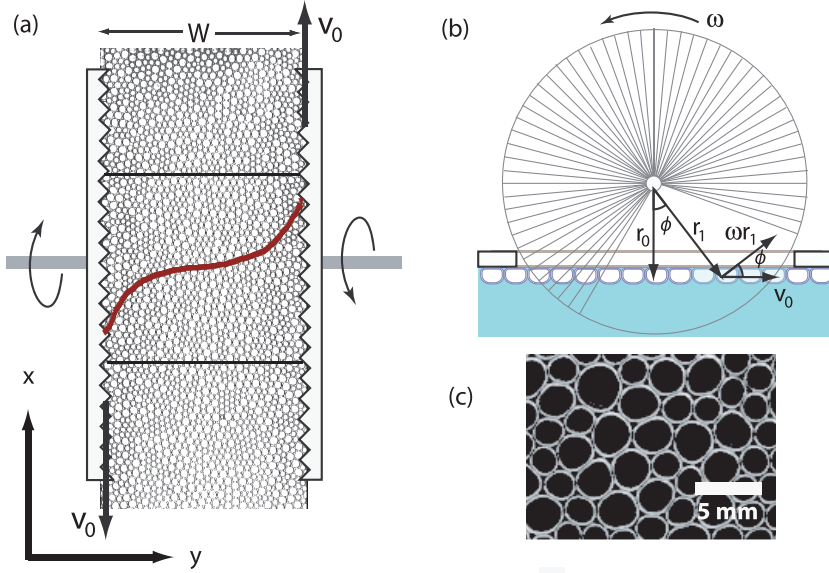
FIGURE 2.4: (a) Schematic topview of the experimental setup. W represents the gap width and the two horizontal lines indicate the edge of the region over which the velocity profiles are calculated. The red curve depicts one such profile.(b) sideview of shearing wheels. The slits in the glassplate are drawn for clarity. Explanation of the x independence of v_x at the liquid surface. (c) Experimental image of the foam, the scalebar represents 5 mm.

images. The bottom of the reservoir is covered with a black plate to improve contrast. The frame rate is fixed such that the displacement at the wheels is fixed at 0.15 mm between frames and we take 1000 frames per run, corresponding to a strain of 3.75 for a 4 cm gap. In the images, 1 pixel corresponds to approximately 0.1 mm.

We obtain the velocity profiles through particle tracking and a Particle Image Velocimetry-like technique: for each y-value, we calculate the cross-correlation $(X_n)^2$ between the corresponding image line $P_n(x)$ of length m and the same image line $P_{n+1}(x)$ in the next frame shifted by an amount τ:

$$X_n(\tau)^2 = \sum_{i=0}^{m-\tau} P_n(i)P_{n+1}(i+\tau). \tag{2.3}$$
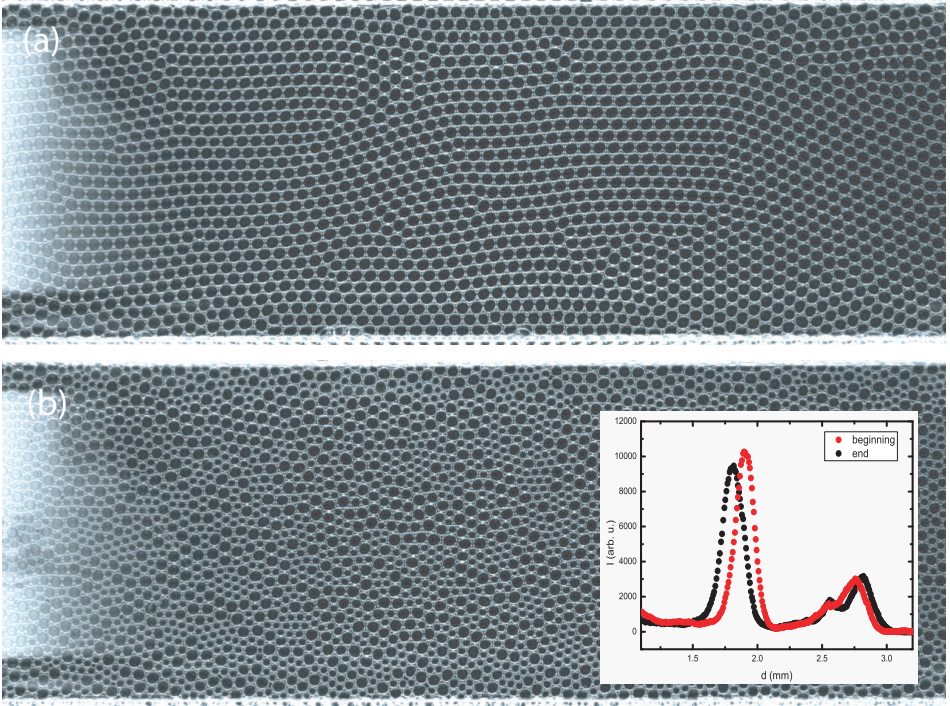
FIGURE 2.5: (a) Images of sheared regions for both (a) monodisperse and (b) bidisperse foams. Inset shows size distribution and coarsening over the duration of an experimental run for bidisperse foams.

We can then proceed in two ways. One option is to, for each y-value, add up all cross-correlations from all frames and calculate the average displacement $\Delta x(y)$ per frame by fitting a parabola to the resulting sum of cross-correlations and taking the peak value of that parabola:

$$\Delta x(y) = \max\left(\sum_{n=0}^{999}(X_n(\tau))^2\right). \tag{2.4}$$

Alternatively, we can fit a parabola to each cross-correlation separately and obtain the average displacement by averaging the maxima of all individual parabolas:

$$\Delta x(y) = \sum_{n=0}^{999}\max\left((X_n(\tau))^2\right). \tag{2.5}$$

39

By comparing to average velocity profiles obtained by particle tracking [75], we find that the latter procedure gives the closest match to the tracking velocity profiles, and we have employed that procedure throughout. We restrict ourself to the central 60 mm of the shearing region, see Fig. 2.4(a), to avoid effects caused by the recirculation of the foam at the edges of the wheels. We thus obtain both spatially (in the x-direction) and temporally averaged velocity profiles. Note that for disordered foams the flow is strongly intermittent, with large fluctuations in bubble velocities and positions. Nevertheless, we obtain smooth reproducible velocity profiles with the above method.
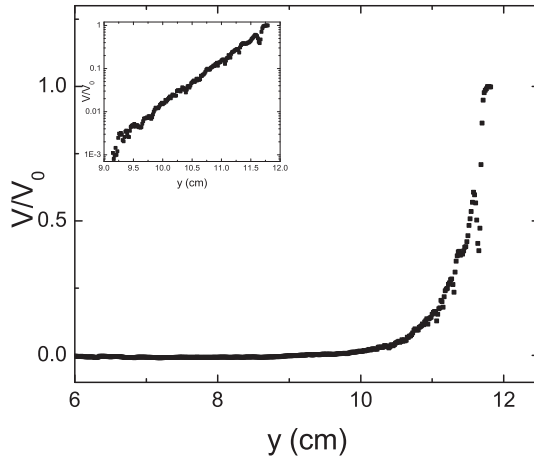
FIGURE 2.6: Flow at the liquid surface in the absence of bubbles, as imaged by depositing silver powder. Inset: same profile on lin-log scale, showing exponential decay away from the boundaries.

We check that the drag on the foam bubbles due to flow of the bulk liquid underneath is negligible by measuring the velocity profile of bubbles floating on a very shallow layer of bulk fluid. In this case the fluid surface velocity is decreased due to the no-slip boundary condition at the reservoirs bottom. This does not alter the profiles. We furthermore measure the velocity profile of the liquid surface itself at the same fluid level as in the foam experiments (≈ 3.5 cm) by imaging the flow of silver particles that were sprinkled on the liquid surface, see Fig. 2.6. We observe an exponentially decreasing velocity profile at the fluid surface, which implies

that even if the fluid drag were of the order of the other drags acting on the bubbles, it would not significantly alter the flow profiles except near the wheels.

To check whether coarsening occurs we measure the bubble size distribution by measuring the surface area of the rings in the images. We obtain sharply peaked size distributions, see inset in Fig. 2.5(b), that show about 3 % coarsening over the duration of the runs, which corresponds to about 2 hours.

2.2.2 Results

Disordered foams

We now focus on averaged velocity profiles in disordered two-dimensional foams. These foams are produced by bubbling a fixed flow rate of nitrogen through syringe needles of 2 different inner diameters, such that bubbles of 1.8 $\pm$0.1 and 2.7 $\pm$0.2 mm result. The bubbles are gently mixed with a spoon until a disordered monolayer results. For gap widths of 5, 7 and 9 cm, we drive the foam at 6 different velocities, spanning 2.5 decades: $v_0 =$ 0.026, 0.083, 0.26, 0.83, 2.6 and 8.3 mm/s.

Note that we perform the sweep in driving velocities from fast to slow and that we preshear the system for one full wheel rotation, to start with bubbles covering the wheel. This is done to ensure the packing fraction remains constant during the strain rate sweep; when the entire circumference of the wheel is covered with bubbles a balance results between bubbles dragged out of the system and injected back in. If we would sweep from slow to fast driving rates, this balance is not achieved, resulting in a packing fraction that decreases during the experiment. To fix the packing fraction, we fix the gap between glass plate and liquid surface at 2.25 $\pm$ 0.01 mm.

Results are plotted in Fig. 2.7: the profiles exhibit shearbanding, and for all gap widths the profiles become increasingly shear banded at increasing driving velocities. The slowest runs at $W = 5$ cm yield essentially linear velocity profiles. We suggest that this is due to the small gap width, which results in overlapping shear banded profiles resembling a linear profile, and we will present a model in section 2.2.3 that supports this conclusion.. This is further illustrated in Fig. 2.7(d): there we plot the velocity profile for a driving velocity of 0.26 mm/s for all three gap widths

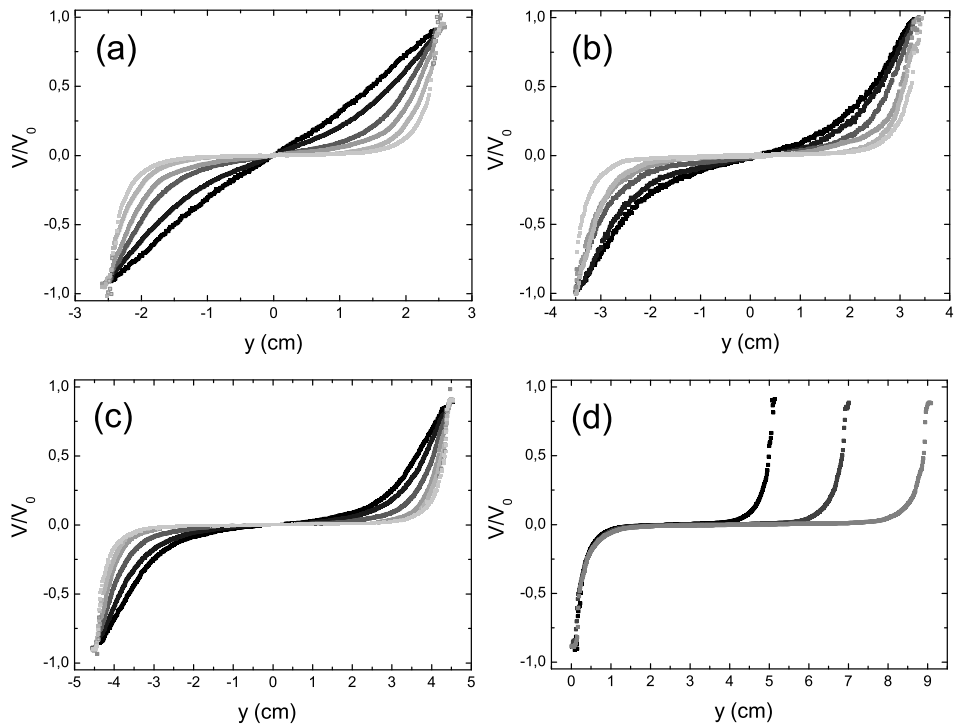FIGURE 2.7: Profiles for a gap width $W = 5$ (a) 7 (b) and 9(c) cm. From black to light grey, $v_0 = 0.026$ mm/s, 0.083 mm/s, 0.26 mm/s, 0.83 mm/s, 2.6 mm/s and 8.3 mm/s. For all gap widths we observe that the localisation near the driving wheels increases for increasing driving velocity. (d) Profiles at 2.6 mm/s for all three gap widths. Regardless of the gap width all profiles decay at the same rate.

together, which clearly shows that for all widths, the velocity profiles decay at the same rate. Fig. 2.7(d) thus hints that in this experiment the driving velocity at the edges, instead of the overall shear, sets the velocity profiles. Therefore the local response to forcing will provide the key towards understanding the shape of these profiles. Note finally that the profiles do not exhibit slip with respect to shearing wheels, except for the fastest runs.

2.2.3 Model

We now propose a model to account for the shear banding behaviour discussed above. We ignore the elastic energies in the system and only consider the viscous drags. The relevant drag forces in our system have already been discussed in section 1.2.4 and we will do so once more: F_{bw}, the drag force per bubble sliding past a solid wall, scales as

$$F_{bw} = f_{bw}(Ca)^{2/3} = f_{bw} \left(\eta v / \sigma \right)^{2/3}, \qquad (2.6)$$

with η the bulk viscosity, σ the surface tension and f_{bw} a constant with dimensions of force. Typically $f_{bw} \propto \sigma r_c$ [18], with r_c the radius of the deformed contact between bubble and wall. We remind the reader that for bubbles in a soapy solution, the 2/3 scaling with Ca only holds for surfactants that are mobile [20], see section 1.2.4. Results from [4] strongly indicate that this is indeed the case for Dawn, and we will later confirm that this scaling applies to our system.

The drag force between 2 bubbles sliding past each other has not received much attention up to now, although [24] provides indirect evidence that it scales like F_{bw}, i.e. $F_{bb} \propto (\eta \Delta Ca)^\zeta$, with $\Delta Ca \equiv \eta \Delta v / \sigma$. In a very recent paper it is explicitly shown that it scales indeed as $(\Delta Ca)^\zeta$, [25]. The authors find $\zeta = 0.5$, although various physico-chemical peculiarities, as well as the range of Ca one measures in, can alter this exponent. Note that the physical mechanism leading to this scaling is markedly different from that leading to the nontrivial scaling of the bubble-wall drag: the viscous drag between a bubble and a wall is due to the variations in thickness of the thin film separating the two, whereas in this case it is actually the size of the deformed facet that changes when two bubbles come into contact and slide past each other.

Taking all of this into consideration, it seems reasonable to assume

that:

$$F_{bb} = f_{bb} \left(\eta \Delta v / \sigma \right)^{\zeta},$$ (2.7)

again with $f_{bb} \propto \sigma \kappa_c$, with κ_c the radius of the deformed contact between bubbles.
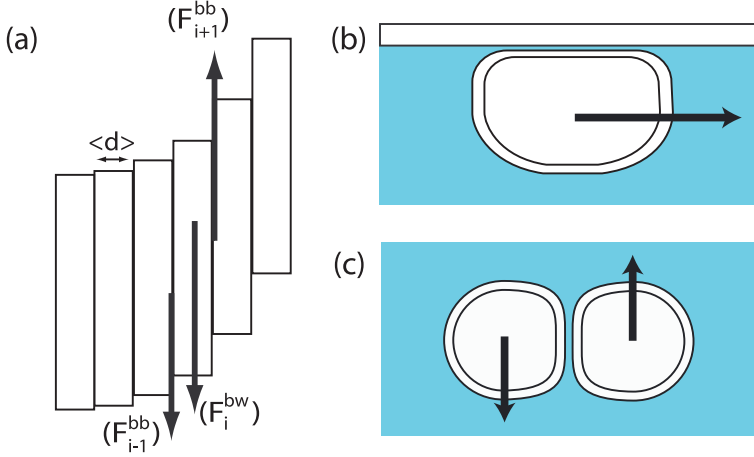
FIGURE 2.8: Illustration of drag balance model. The shear region is divided in lanes labeled i which all experience a drag force de to the top plate and due to both neighboring lanes. Illustration of the films around which the viscous drag forces act.

We now assume that at every y-position in the shearing region the average drag forces per bubble $\overline{F}_{bw}$ and $\overline{F}_{bb}$ scale in a similar way with velocity as the individual drag forces. In particular, we will assume that $\overline{F}_{bw} = f_{bw}(Ca)^{2/3}$, but that $\overline{F}_{bb} = f_Y + f_{bb}(\Delta Ca)^{\beta}$. We thus leave the possibility open that the averaged bubble-bubble drag forces scale differently from the drag froces experienced by single sliding pairs of bubbles. We divide our shearing region in lanes labeled i and assume that on every lane the time-averaged top plate drag per bubble $\overline{F}_{bw}^{i}$ balances with the time-averaged viscous drag per bubble due to the lane to the left ($\overline{F}_{bb}^{i}$) and right ($\overline{F}_{bb}^{i+1}$), see Fig. 2.8:

$$\overline{F}_{bb}^{i+1} - \overline{F}_{bw}^{i} - \overline{F}_{bb}^{i} = 0.$$ (2.8)

We assume that the averaged drag forces scale similar to the bubble drag force, but allow for a yield drag term in the interbubble drag, to remain consistent with rheometrical data presented later on and to reflect the elastic barrier bubbles have to overcome before they slide past each other, and write:

$$\overline{F}^i_{bw} = f_{bw}(\eta v_i/\sigma)^{2/3} \, , \tag{2.9}$$
$$\overline{F}^i_{bb} = f_Y + f_{bb}\left[(\eta/\sigma)(v_i - v_{i-1})\right]^\beta \, , \tag{2.10}$$
$$\overline{F}^{i+1}_{bb} = f_Y + f_{bb}\left[(\eta/\sigma)(v_{i+1} - v_i)\right]^\beta \, . \tag{2.11}$$

Note that assuming similar behaviour between the averaged drag forces and the local drag forces is a rather strong statement, given that, due to the intermittent and disordered bubble motion, the instantaneous bubble velocities are fluctuating and not necessarily pointing in the x-direction.

Inserting the expressions from Eq. (2.11) into Eq. (2.8) and defining $k = f_{bw}/f_{bb}$ we arrive at:

$$k\left(\frac{\eta v_i}{\sigma}\right)^{2/3} = \left(\frac{\eta}{\sigma}\right)^\beta \left[(v_{i+1} - v_i)^\beta - (v_i - v_{i-1})^\beta\right] \, . \tag{2.12}$$

Note that the yield drag contributions cancel, which is a particular advantage of the linear geometry we work in.

To actually solve Eq. (2.12) numerically, it turns out we need to take into account the discrete nature of both the bubbles and the pixels in the images, as the distance in Eq. (2.12) between the v_i's is not arbitrary, but set by the average bubble diameter $\langle d \rangle$. The forward difference on the bubble scale is

$$v_{i+1} - v_i = \langle d \rangle \cdot \frac{\partial v}{\partial y}\Big|_{y=y_i}, \tag{2.13}$$

in differential form. In the images, however, the velocities are separated by the pixel size p. One can of course reverse Eq. (2.13) and write

$$\frac{\partial v}{\partial y}\Big|_{y=y_i} = \frac{1}{p}(v_{i'+1} - v_{i'}) \tag{2.14}$$

to end up with the forward difference on the pixel scale. Combining Eqs. (2.13) and (2.14) and recognising that the full forward difference of Eq. (2.12) is given by

$$(v_{i+1} - v_i)^\beta - (v_i - v_{i-1})^\beta = \langle d \rangle^{1+\beta} \cdot \frac{\partial}{\partial y}\left(\frac{\partial v}{\partial y}\right)^\beta\Big|_{y=y_i}, \tag{2.15}$$

we can write Eq. (2.12) in a form that is suited for numerical integration:

$$\frac{k}{(\langle d \rangle / p)^{1+\beta}} \cdot \left(\frac{\eta v_i}{\sigma} \right)^{2/3} = \left(\frac{\eta}{\sigma} \right)^{\beta} \left[(v_{i+1} - v_i)^{\beta} - (v_i - v_{i-1})^{\beta} \right] \ . \qquad (2.16)$$

2.2.4 Fits

Procedure

We compare all 18 runs to solutions of the model. We focus on the central part of the data where $|v| < 3/4 v_0$ to avoid the considerable edge effects near the shearing wheels (for instance the bumps in the low-velocity profiles in Fig. 2.7(a) and the slip with respect to the wheel in the fast runs). Since the shape of the velocity profiles is set by the local velocity, we assume this is a valid procedure, and will not affect the shape of the model solution. We numerically integrate Eq. (2.16) from $y = 0$, where $v = 0$, to the y value for which $v = 3/4 \cdot v_0$, while keeping β and k fixed. The drag force balance should govern the shape of the velocity profiles for all driving rates and gap widths and hence, at fixed β, for all profiles we determine the k value that gives the best fit to the data. The k values exhibit a systematic variation that depends on the value of β one chooses, see Fig. 2.9(f), and by repeating the procedure for a range of β we determine the value for which the variation in k is minimized. We subsequently fix k and β and take these values to hold for all data sets.

Results

We capture the shape of all data sets with high accuracy by fixing k and β, whose values are $k = 3.75$ and $\beta = 0.36 \pm 0.05$ as extracted from Fig. 2.9(f). The results are plotted in Fig. 2.9, and we see that for these values all velocity profiles are adequately fitted except for the slowest runs at $W = 5$ cm. We attribute this to the observation that edge effects extend further into the shearing region for small gaps. Note that the model profiles exhibit linear tails, see Fig. 2.9(e), and that the experimental velocity profiles in the same figure exhibit approximately the same behaviour. We can thus conclude that both the experimental and model profiles do not decay exponentially, in contrast with results found in previous studies [9, 66].
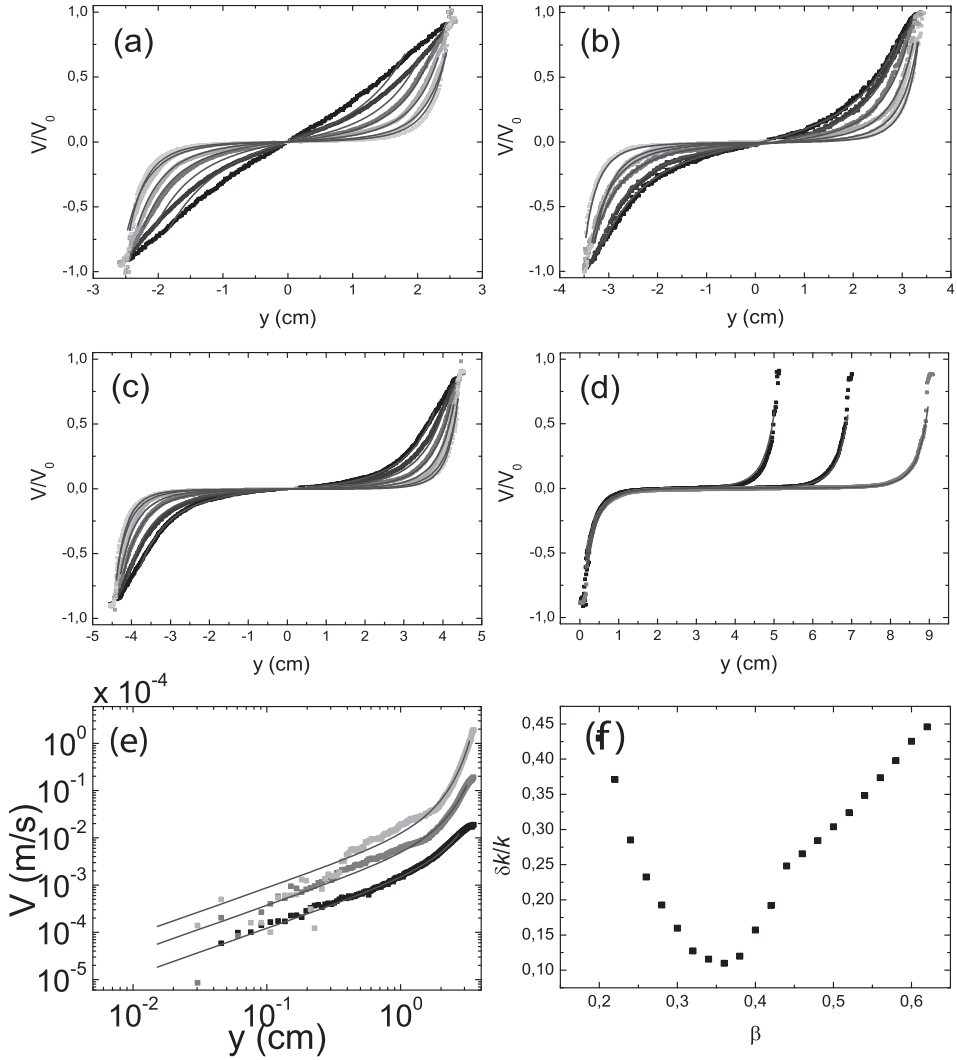
FIGURE 2.9: (a)-(d) Velocity profiles from Fig. 2.7 with model profiles obtained for $k = 3.75$ and $\beta = 0.36 \pm 0.05$. The model profiles fit the experimental data very well, except for the slowest runs at $W = 5$ cm gap. (e) Unrescaled velocity profiles for $V_0 = 0.026$ (black), 0.26 (grey) and 0.26 (light gray) mm/s and corresponding fits plotted on a log-log scale, to highlight the linear tails, in particular in the fit profiles. (f) Variance in k over all 18 runs for the bi-disperse foam as a function of β. A clear minimum at $\beta = 0.36$ can be observed.

2.2.5 Continuum Limit

We can take the continuum limit of Eq. (2.13) which reads:

$$f_{bw} \left(\frac{\eta v}{\sigma} \right)^{2/3} \langle d \rangle^{-1} = \frac{\partial \tau}{\partial y} , \tag{2.17}$$

The top plate drag can be considered as a body force and the interbubble drag force as the divergence of a shear stress τ:

$$\tau = \tau_Y + f_{bb} \left(\frac{\eta \langle d \rangle \dot{\gamma}}{\sigma} \right)^{\beta} , \beta = 0.36, \tag{2.18}$$

where τ_Y is an undetermined yield stress. This is the constitutive equation for a Herschel-Bulkley fluid [45] encountered before. We can now associate the averaged bubble drag force scaling at the local level with the power law scaling of the viscous stress in the Herschel-Bulkley model. The fact that the yield stress does not play a role for our velocity profiles can now be understood in two ways: firstly, since it is a constant it vanishes after taking the divergence of the shear stress, secondly, even though we include a yield stress term at the bubble scale, the contributions from both neighbouring lanes cancel in Eq. (2.12). Note that $\beta = 0.36$ is remarkably close to the power law index $n = 0.40$ found for the bulk rheology of three-dimensional mobile foams [20, 47] already discussed in Sec. 2.3 and to the values $n = 0.33$ and $n = 0.45$ found in [71] which were discussed in section 2.1.

2.3 Rheometrical determination of viscous forces in two-dimensional foams

To validate the assumptions made for the bubble-wall drag and the result obtained for the scaling of the local viscous friction inside the foam, in this section we will investigate the viscous forces that act at the bubble scale by rheometry. We use an Anton Paar DSR 301 rheometer, which can be operated in stress controlled mode and, through a feedback loop, also in strain controlled mode. We use the rheometer in strain controlled mode to investigate $\overline{F}_{bw}$. Moreover, we compare measurements, which we argue to reflect the actual drag force at the single bubble level F_{bb},

with measurements of the averaged viscous drag force on a bubble in a disordered flow of foam $\overline{F}_{bb}$.

2.3.1 Bubble-wall drag

We directly measure the bubble-wall friction with a method that was introduced in [20]. We load a monolayer of bubbles (d = 2.4 ± 0.1 mm) between two PMMA plates of radius R_P = 2 cm. The bubbles are pinned to the lower plate by means of a hexagonal pattern of indentations of size $\mathcal{O}(d)$, and can slip with respect to the smooth upper plate which is connected to the rheometer head. We measure the torque exerted by the bubbles as a function of the angular velocity of the smooth plate.

FIGURE 2.10: Close-up photograph of the rheometrical tool used to measure the bubble-wall drag. The radius r_c is clearly visible in reflected light and is used to extract R_0.

We convert $T(\omega)$ to $\overline{F}_{bw}(Ca)$ in the following way: each bubble exerts a wall stress $\tau_w = \overline{F}_{bw}/\pi R_0^2$ on the smooth plate. We integrate the contribution to the torque of this wall stress over the plate:

$$T = \int_0^{R_P} \tau_w r 2\pi r dr = \int_0^{R_P} \frac{\overline{F}_{bw}}{R_0^2} 2r^2 dr. \qquad (2.19)$$

If we now assume that $\overline{F}_{bw} \propto [Ca]^\alpha = \left[\frac{\eta \omega r}{\sigma}\right]^\alpha$, we can immediately read of

from the data that $\alpha = 0.67$, see Fig. 2.11(a), so inserting this expression in the integral Eq. (2.19) yields:

$$T = \frac{2\overline{F}_{bw}R_p^{3.67}}{3.67R_0^2}.\tag{2.20}$$

Since the bubbles are flattened during the measurement, we can only measure r_c by looking at the reflection of the deformed facet, see Fig. 2.10. We find $r_c = 1.59$ mm. As the bubble radius is smaller than κ^{-1} we can express R_0 in terms of r_c through $R_0^2 = \sqrt{\frac{3}{2}}r_c\kappa^{-1}$ (see chapter 1, section 2.3). Note that this derivation of r_c in terms of R_0 hinges on the assumption that the bubbles are not too deformed, which is not obvious in the rheometrical geometry, but for lack of a more precise relation we use it. We finally rescale the horizontal axis by multiplying ω with $\eta R_p/\sigma$. The resulting curve is plotted in Fig. 2.11(a).

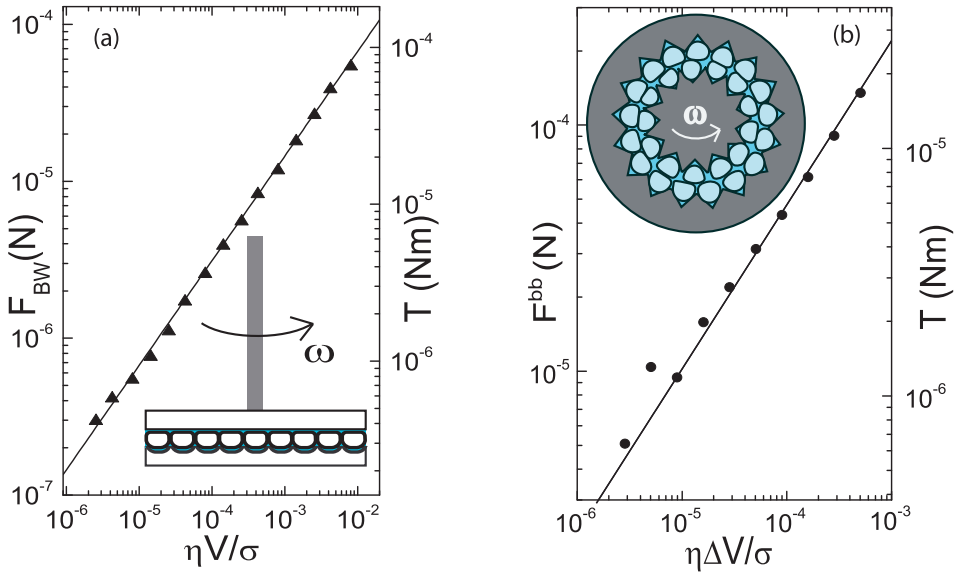FIGURE 2.11: (a) Drag force per bubble exerted on smooth rotated plate as a function of Ca. The solid line represents $0.0015 \pm 0.0001 \cdot (\eta v/\sigma)^{2/3}$. The inset shows experimental geometry. (b) Drag force per bubble exerted by neighbouring, ordered lane of bubbles in a geometry that mimics the ordered sliding of bubble lanes. The solid line represents $0.022 \pm 0.002 \cdot (\eta \Delta v/\sigma)^{2/3}$.

2.3.2 Bubble-bubble drag

Drag at the bubble scale

To measure the power law scaling of the inter-bubble drag we abandon the linear geometry for a moment and actually measure the torque exerted by a foam driven at a strain rate $\dot{\gamma}$ in a cylindrical Couette geometry, which consists of an inner driving wheel, connected to the rheometer head, rotating inside an outer ring. This is a natural geometry to perform rheometry in. We will get back to the peculiarities of foam flow in a cylindrical geometry in chapter 3. The rheometrical experiments are performed with bubble rafts, i.e. foams that are not confined by a top plate, as the additional stresses due to the wall would disturb a clean rheological measurement.

Both boundaries are grooved to ensure a no slip boundary for the bubbles, of which a monolayer floats in the shearing region. We start with measuring $\overline{F}_{bb}$ for the ordered case by keeping the gap between the cylinders such that exactly two layers of bubbles fit in, see the inset of Fig. 2.11(b). The inner radius (r_i) is 1.25 cm and the outer radius (r_o) is 2.5 cm. We deposit 6mm diameter bubbles in the grooves, make sure that all bubbles are strictly pinned and remain in their groove, and vary the rotation rate ω of the inner cylinder over 2.5 decades while measuring the torque averaged over one rotation. The result is plotted in Fig. 2.11(b): even though the torque fluctuates enormously due to the elastic barrier the bubbles have to overcome before they can pass a neighbour, the force per bubble averaged over many such events scales with the dimensionless velocity difference as a power law with index 2/3, just as the wall drag scales with bubble velocity. No signs of a yield stress are observed, and we believe this is due to the fact that all elastic energy that is stored in the bubble deformation is released after yielding, such that one measures purely the viscous drag.

We multiply ω by $\eta r_i/\sigma$ to rescale to the dimensionless velocity difference and we divide the torque by r_i and the number of bubbles pinned at the inner wheel (i.e 10) to obtain the averaged bubble-bubble drag force per bubble in the ordered case, and in these rescaled coordinates we have plotted the results in Fig. 2.11(b).
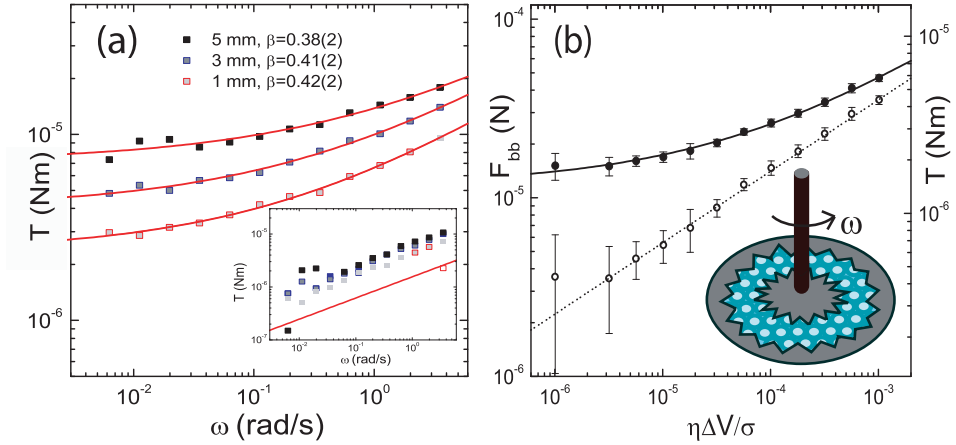
51

FIGURE 2.12: (a) Torque exerted on the inner wheel by a *monodisperse* foam in a Taylor-Couette geometry where the gap is of the order of 6-7 $\langle d \rangle$, for different bubble sizes. Fits are to Herschel-Bulkley model, power law indices β from fits are shown in graph. Inset shows same data with yield torque from fit subtracted, solid line is power law with index 0.4. Surprisingly, the yield stress increases with increasing bubble size. (b) Averaged drag force per bubble in a *bidisperse*, disordered foam. The foam is sheared in a Couette cell of inner radius 1.25 cm, outer radius 2.5 cm (hence a gap of 5 bubble diameters) without a top plate, see inset. We obtain $\overline{F}_{bb} = f_Y + f_{bb}(\Delta Ca)^\beta$, with the yield threshold $f_Y \approx 1.2 \pm 0.5 \times 10^{-5}$ N, $f_{bb} \approx 5.6 \pm 0.9 \times 10^{-4}$ N and $\beta = 0.40 \pm 0.02$ (solid line). Open circles are the same data with the yield torque obtained from the fit subtracted, which are well fit by a pure power-law with exponent 0.4 (dashed line).

From local to bulk viscous drag

We observe that the scaling exponent for the viscous drag at the bubble scale differs markedly from the scaling of the local viscosity inside the bulk foam as extracted from the velocity profiles, e.g., $\zeta = 2/3$ vs. $\beta = 0.36$. We hypothesize this is due to the disordered flow in the foam and will provide supporting evidence in what follows.

Still loading the cell with monodisperse foams with bubble radii of 1, 3 and 5 mm, we increase r_o to 8 cm, such that more layers of bubbles can fit inside the cell. However, since r_i is small, the curvature is high, which forces the foam to deviate from hexagonal packing during rotations. In this way we induce disorder through geometry. The resulting measurements, see Fig. 2.12(b), show clear yield stress behaviour and can be ex-

cellently fit by the Herschel-Bulkley model, yielding for all bubble sizes $\beta \approx 0.4$, which is markedly lower than the 2/3 found for the drag force in ordered lanes above, and close to the 0.36 extracted from the velocity profiles. Surprisingly, the yield stress appears to increase with increasing bubble radius, contrary to the intuition that the yield stress is set by the Laplace pressure and should hence scale in inverse proportion to the bubble radius. We attribute this to the deformation of the bubbles through the capillary flotation force, which is larger for larger bubbles and hence leads to a relatively larger contact size between the bubbles.

In order to convincingly establish a connection between the rheometrical data and the model, we now return to the geometry used for the ordered foams ($r_i = 1.25$ cm and $r_o = 2.5$ cm), and measure the torque exerted on the inner wheel by a *bidisperse* foam with the same bubble sizes as in the linear shear experiment. We obtain a clear confirmation that indeed the disorder changes the power law scaling of $\overline{F}_{bb}$: we again reproducibly measure Herschel-Bulkley behaviour with power law index $\beta \approx 0.40$, as can be seen in Figs. 2.12(b). To convert torques to $\overline{F}^{bb}$, we again divide by the number of bubbles and r_i. Since our outer rough boundary forces the bubble velocity to zero, we can rescale the angular frequency to the dimensionless velocity difference $\eta \Delta v / \sigma$ by assuming a linear velocity profile across the gap, decaying from ωr_i to 0. The gap width is approximately $6 \langle d \rangle$ and hence we can estimate Δv. We extract from the rheological measurements an estimate for the ratio $k = f_{bw}/f_{bb} \approx 2.5 \pm 0.5$. This is close to the value $k = 3.75 \pm 0.5$ estimated from the flow profiles.

2.4 Discussion

The drag forces exerted on the bubbles by the top plate, which at first sight might be seen as obscuring the bulk rheology of the foam, enable us to back out the effective inter-bubble drag forces and constitutive relation of foams from the average velocity profiles. To further appreciate this fact, note that our model yields linear velocity profiles regardless of the exponent β if the body force due to the wall drag is zero.

By comparing the results obtained from the velocity profiles with the rheometrical measurements, we note a remarkable difference between the scaling of the bubble-bubble drag forces at the bubble level, which we have mimicked by strictly ordered bubble rheology, and the scaling at

the bulk level, which we have extracted from the velocity profiles and confirmed by rheometry: we find $F_{bb} \sim (\Delta v)^{2/3}$ at the bubble level and $\overline{F}_{bb} \sim (\Delta v)^{0.36}$ at the bulk level.

One might understand this anomalous scaling as follows: The degree of disorder does not affect the drag forces at the bubble scale, but it does modify the bubble motion. For disordered foams, the bubbles exhibit non-affine and irregular motion — hence they "rub" their neighbouring bubbles much more than when their flow is orderly, and consequently the averaged viscous dissipation is enhanced over what could naively be expected from the local drag forces [76]. This picture is corroborated by recent simulations on the bubble model [23], where one recovers this "renormalisation" of the drag force exponent [77, 78] and rate-dependent flow profiles [78].

In this vein, one could wonder why the drag with the top plate is not changed by the disordered motion of the foam bubbles. We have no definite answer, but we have verified, using tracking of the bubble motion, that the average of the instantenous bubble-plate drag force is very similar to the drag force calculated from applying the Bretherton result to the average velocity:

$$< (\vec{v}/|v|)_x |v|^{2/3} > \approx 0.9 < v_x >^{2/3} \ . \tag{2.21}$$

On the other hand, the bubble-bubble drag force involves velocity *differences*, which therefore are much more broadly distributed, in particular when $\Delta v < v$ — apparently this causes the breakdown of the affine assumption.

Finally, the origin of the edge effects that prevent us from fitting our full experimental curves with the model profiles, might be due to the fluid drag near the wheels, as discussed in section 2.2.1. Alternatively the origin might lie in the absence of a local flow rule near the driving wheels as reported in [79]. One way to resolve this is accommodating non-local behaviour in our model, for instance by incorporating drag terms due to next nearest lanes, similar to the cooperativity length introduced in [79]. Nevertheless, since our model *is* local in spirit, it has enabled us to back out valuable information even though we have not been able to use the full velocity profiles.

2.5 Ordered foams

A final indication that indeed the disordered flow of the bidisperse foam is at the root of the anomalous scaling of the bulk viscosity with shear rate can be given by shearing ordered, monodisperse foams in the linear geometry, as was done in [66]. In this case the bubbles are expected to move affinely with the global shear, in which case one would expect the global viscous drag forces to scale the same as the local one.
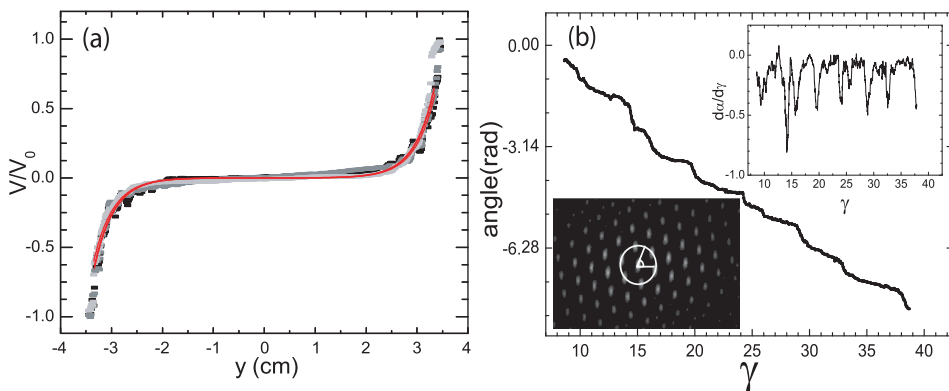

FIGURE 2.13: (a) Velocity profiles for a monodisperse, ordered foam with crystal axis aligned with the wheels. Gap $W = 7$ cm and $v_0 = 0.083$ (black), 0.26 (dark grey) and 0.83 (light grey) mm/s. Solid curves indicate fits to the model with $k = 0.3$, $\alpha = \beta = 2/3$. (b) Angle of the monodisperse foam with respect to the shearing direction as a function of strain (time): the foam remains stationary for considerable strains, after which it rapidly rotates over $\pi/3$. Upper inset shows derivative of main graph to highlight the apparent periodicity of the rotations. Lower inset shows 2D autocorrelation of foam image with the circle located at the first order maxima used to determine the rotation.

We shear a monodisperse, ordered foam with bubbles of size 2.7 mm, produced by blowing nitrogen through one syringe needle at fixed flow rate, at a gap W of 7 cm at $v_0 = 0.083, 0.26$ and 0.83 mm/s. We recover the rate independent and strongly shear banded velocity profiles reported in [66] (see Fig. 2.13). However, it turns out that the orientation of the hexagonal bubble packing with respect to the shearing direction of the foam is crucial for reproducibility: the monodisperse foam orients itself with one of its crystal axes parallel to the shearing boundaries and remains in that state for a considerable time, until it rather rapidly and

collectively rotates over an angle of $\pi/3$ radians until the next crystal axis is aligned with the wheels. We investigate this by taking the 2D-autocorrelation of the foam images taken from a run at 10 cm and measuring the pixel intensity along a circle located at the first order maxima, see inset of Fig. 2.13(b).

By cross correlating the intensity profile of the first image with that of later images, we obtain Fig. 2.13(b): the foam remains stationary for considerable strains, after which it quite rapidly rotates over $\pi/3$ radians and remains stationary again. The upper inset of Fig. 2.13(b) displays the derivative of the angle with time and confirms that stationary periods are interspersed with bursts, during which the foam rapidly rotates, and to which one could maybe even contribute a periodicity.

This remarkable phenomenon is, however, avoided by increasing the aspect ratio of the shearing region. By doing so, the interval between the rotation events is considerably increased and hence one can safely measure in the strictly ordered regime, with the bubbles aligned with the shearing wheels. How this rotation is avoided in [66] we do not know, but if one looks at the experimental images in that paper, one observes that the monodisperse domains only extend over 7 — 8 bubbles due to the presence of defects, thus likely hindering large-scale collective rearrangements, while at the same time leaving enough ordered foam at the shearing boundaries to allow for rate independent shear banding.

As in the case of the bidisperse foams, we fit model profiles to our experimental data. For our model to yield rate independent velocity profiles, the drag forces need to balance in the same ratio for all driving velocities. This can only be achieved if $\beta = 2/3$ since we have already confirmed with rheometry that $\alpha = 2/3$. Indeed we find that the experimental profiles are best fit by model profiles if one fixes $k = 0.3$ and $\beta = 0.67 \pm 0.05$, see Fig. 2.13. The value of k is remarkably small. If we assume that prefactor f_{bw} for the bubble wall drag remains unchanged for the ordered foam, this means that the bubble-bubble drag prefactor f_{bb} is much larger compared to its value for a disordered foam. Note however, that the power law exponent β greatly influences the value of the drag force: for instance, if $\Delta v = 0.001$ m/s, then $(\eta v/\sigma)^{2/3} = 1.6 \times 10^{-3}$, whereas $(\eta v/\sigma)^{0.36} = 3.1 \times 10^{-2}$, which is more than an order of magnitude larger.

Disorder

We now return to the question how disorder sets the rheological behaviour in foam flows. We have shown that the average drag between bubbles scales as $v^{2/3}$ for monodisperse foams, whereas it scales as $v^{0.36}$ for bidisperse foams. On the other hand, at the bubble level, the drag forces scale as $v^{2/3}$ as is evidenced by the rheometrical data presented in 2.11(b). We speculate that this is closely connected to the non-affine behaviour of the bubbles [23, 76, 80]: close to the jamming transition, the shear modulus of the foam becomes anomalously large due to the fact that bubbles fluctuate much more than can be expected from the affine prediction — which is that the bubbles follow the imposed shear — and thus dissipation increases.

In our experiment, this results in an anomalous scaling of the bubble-bubble drag force, which in turn is reflected in the observed rate dependence of the velocity profiles for bidisperse foams. We can thus investigate when the rate dependence of the velocity profiles first occurs by gradually increasing the disorder in a monodisperse foam.

To this end we record velocity profiles in a monodisperse foam made of 2.7 mm size bubbles in which we gradually increase the area fraction of smaller (1.8 mm) bubbles. After mixing the two species we measure velocity profiles at $v_0 = 0.083, 0.26$ and 0.83 mm/s. We already observe the occurrence of rate dependent velocity profiles for small quantities of defects, indicating that rate independent flows are in fact limited to the singular case of completely ordered foams. We have not quantified the amount of disordered motion, but by visual inspection, we already see the swirling patterns, typical of our 50/50 bidisperse foam, occuring at 2 % disorder.
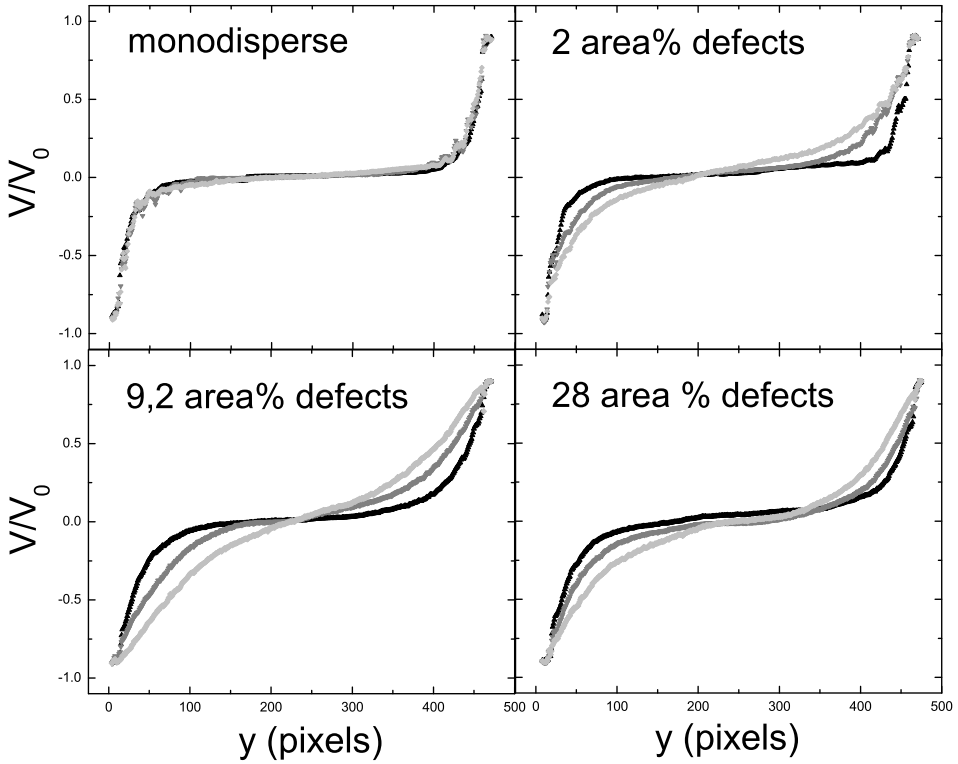
FIGURE 2.14: Velocity profiles for an ordered foam consisting of 2.7 mm bubbles for driving velocities $v_0 = 0.083$ mm/s (light gray), $v_0 = 0.083$ mm/s (dark grey) and $v_0 = 0.083$ mm/s (black) to which defects are added in the form of an increasing area fraction of 1.8 mm bubbles.

RHEOLOGY OF TWO DIMENSIONAL FOAMS IN A TAYLOR-COUETTE GEOMETRY

To test and expand the applicability of the drag force balance model developed in the last chapter, we perform experiments on bidisperse monolayers of foam bubbles, sheared in a Taylor-Couette geometry. In contrast to the linear geometry used in the previous chapter, the Couette geometry allows to study the flow of bubble rafts, i.e., 2D foams not trapped under a top plate. Also, its curved geometry means that the yielding threshold included in the expression for $\overline{F}_{bb}$ should play a role. We record averaged velocity profiles both with and without a bounding glass plate.

Our main finding is that two-dimensional foam flows in a Couette geometry with a top plate exhibit rate dependent and strongly shearbanded flows, whereas bubble raft flows are much less shearbanded and rate independent. We can fit the flows without a top plate to both a power law fluid model and solutions to the drag force balance model provided the local stresses scale with the local strain rate $\dot{\gamma}$ as $\tau = k\dot{\gamma}^{0.21}$. This is corroborated by direct measurements of the local stress-strain rate relation. In contrast, our drag force model fits poorly to the flows with a top plate if $\beta = 0.21$, but we do not succeed in establishing an optimal value of β in that case.

Strikingly, the model fits adequately only if we assume that the yield drag force — of which we should see the effects in the Couette geometry, in

contrast to the linear geometry — is 0 or at least one order of magnitude smaller than what was measured in the previous chapter from the bulk rheometry a two-dimensional foam. This suggests that foams in a Taylor-Couette geometry still flow if the local stress is considerably below the globally measured yield stress.

3.1 Introduction

The flow of two dimensional foams has mainly been studied in Taylor-Couette geometries. For example, Dennin and coworkers have sheared bubble rafts in a Couette geometry with a fixed inner disc and a rotating outer cylinder [8, 71]. Debrégeas has confined foam bubbles in a Hele-Shaw cell and rotated the inner disc, while keeping the outer cylinder fixed [9]. In both cases, shear banded flow profiles where found. However, there has been no clear consensus on the cause of the shear bands in these systems, but clearly both the radial decay of the shear stress in curved geometries and the presence of a top-plate need to be considered. Cheddadi et al. [81] claim the wall drag that results from the top plate is not the main cause of shear banding: instead they attribute the shear banding to the inhomogeneity of the stresses which decay as $1/r^2$, see Appendix 3.A for a derivation. Scheibert et al. [72] instead claim that focusing of the stresses due to the quadrupolar stress field resulting from a T1 lies at the root of the shear banding.

Our strategy for disentangling the roles of wall drag and curvature is to fit flow profiles, obtained for a range of driving rates in Couette geometries with and without a top plate, to the Herschel-Bulkley-like model which described the flow in the linear geometry of chapter 2 in detail. Note that the velocity profiles measured by Gilbreth, Sullivan and Dennin [68] were also with some success fit to solutions of a Herschel-Bulkley constitutive equation, which suggests that our previously developed model might be applicable in the cylindrical geometry as well. An additional hint in that direction is that the continuum model that was postulated by Janiaud et al. [10] to describe two-dimensional foam flows with an additional wall drag, can be applied to the cylindrical geometry [82] and at least qualitatively, Krishan and Dennin [83] have obtained experimental confirmation of a few of their predictions.

Apart from the role of wall drag and curvature, an additional impor-

tant issue is whether the transition from the flowing region to the stationary region is continuous: most earlier literature finds a discontinuous transition between a flowing and a non-flowing part in complex fluids: for instance Dennin and coworkers claim in [71] that the transition is discontinuous. Such discontinuous shear bands are also often observed in polymer systems and have also recently been observed by MRI imaging of the rheology of three-dimensional foams and emulsions [84, 85]. For the curved geometry, a discontinuous transition between the flowing and stationary flow can be seen as a direct consequence of the existence of a finite yield threshold: a part of the system that experiences local stresses below the yield stress will not flow and a region that is above the yield stress will.

For linear geometries as discussed in Chapter 2, the yield stress drops out and no discontinuity is found — similarly Wang, Krishan and Dennin find continuous shear bands in linearly sheared foams [66, 86]. In the curved geometry the yield stress cannot be ignored and if there were an appreciable yield stress we would observe this in our fitting procedure. Moreover, one could expect to see a discontinuity in the experimental velocity profiles providing a clear signature of the presence of a yield stress.

We will measure velocity profiles of two-dimensional foams in a Taylor-Couette geometry. We can study two cases. First, we add a top glass plate to study shear localization in a setup that is very similar to the Hele-Shaw type cell employed by Debrégeas et al. [9]. Second, we will also study flows without top plate, to investigate possibly discontinuous shear banding in a bubble raft geometry akin to the one employed by Dennin and coworkers. Surprisingly, we will see that our system, in stead of resolving these issues, merely raises new ones. First, we find essentially continuous flow profiles and the corresponding fitted values of the yield stress are at least an order of magnitude smaller than what was obtained from rheometry. Second, our power law exponent for systems with and without top plate differ. Third, a close comparison of the local rheology with the global rheology finds puzzling discrepancies.
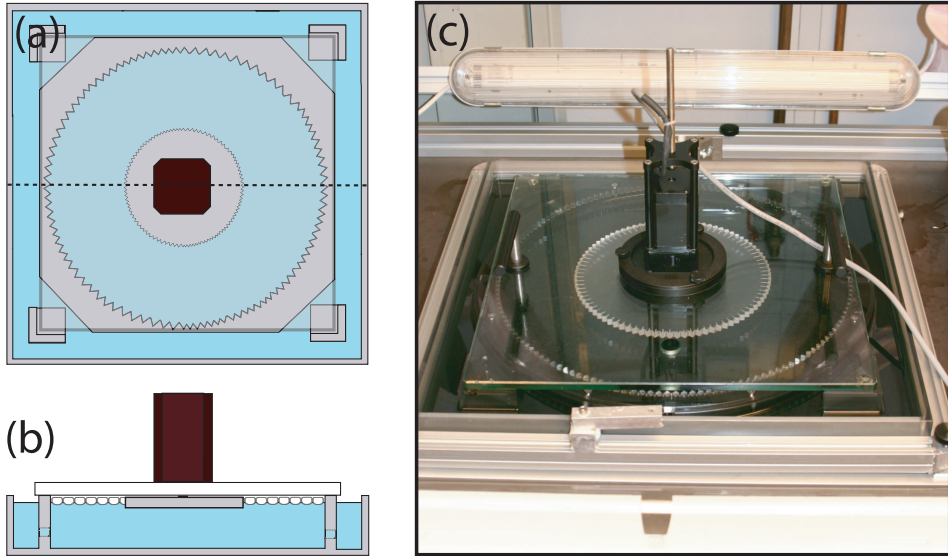
FIGURE 3.1: (a) Schematic top view of Taylor-Couette cell used in this experiment. The outer cylinder, reservoirs and supports for the glass plate have been milled into a PMMA block. (b) Side view: the reservoirs and the bounded area are connected to keep the region underneath the glass plate from draining. The motor is connected to the inner cylinder through the glass plate. (c) Photograph of the experimental setup.

3.2 Experiment

3.2.1 Setup

Our experimental setup consists of a 500 by 500 by 50 mm square PMMA block, into which the outer cylinder, a reservoir and supports for a removable glass plate are milled, see Fig. 3.1. The boundary of the reservoir acts as the outer cylinder (of radius $r_o = 190$ mm) and is grooved with 6 mm grooves. On the glass plate of 405 by 405 by 12 mm, two handles and a casing for a stepper motor are fixed by UV curing glue. The stepper motor (L-5709 Lin engineering) is connected to an inner cylinder of $r_i = 105$ mm radius through a hole in the glass plate. The inner cylinder is grooved like the outer cylinder. The region that is filled with bubbles is in direct contact with the reservoirs outside the glass plate. This is to keep the liquid level underneath the glass plate constant, as fluid that has left the shear-

ing region due to capillary suction will reenter the system in the outside reservoirs.

A bidisperse foam is produced by filling the reservoir with the same soap solution as used previously and immersing syringe needles of two inner diameters, bubbling nitrogen through bothy needles and subsequently thoroughly mixing the resulting bubbles. The resulting bubble sizes are as before: $d_1, d_2 = 1.8, 2.7$ mm. The glass plate, with the inner driving wheel attached, is carefully placed on top of the foam and subsequently, the foam is allowed to equilibrate for a considerable time. Approximately 40 bubble layers are contained within the gap.

3.2.2   Imaging

The foam is lit laterally by 4 fluorescent tubes driven by HF ballasts and images are recorded by a CCD camera (Foculus FO 432BW), equipped with a Tamron 280-300 telezoomlens. The bottom of the reservoir is black, to enhance contrast. The frame rate is fixed such that the angular displacement of the inner cylinder is fixed at 1.12×10^{-3} rad/frame. We record only during steady shear, ensuring that the foam has been sheared considerably before starting image acquisition.

We calculate velocity profiles across the gap between inner and outer wheel by cross correlating arcs of fixed radial distance in subsequent frames over a large angular region. While this improves statistics, it forces us to calculate velocity profiles on curved image lines. However, by defining circular arcs and identifying these with the appropriate pixels, this can easily be done, see Fig. 3.2. We compute averaged velocities over 2000 frames for the slowest runs with a top plate, 10000 frames for the fastest runs with a top plate and over 3000 frames for the bubble raft experiment, to enhance statistics. We check that coarsening, coalescence and rupturing are absent in the runs with a top plate, whereas we cannot rule out the latter two phenomena in the bubble raft experiment. There we merely content ourselves with the absence of holes in our foam during the experiment, which can be achieved by loading the Couette cell with a surplus of foam far away from the imaging region.
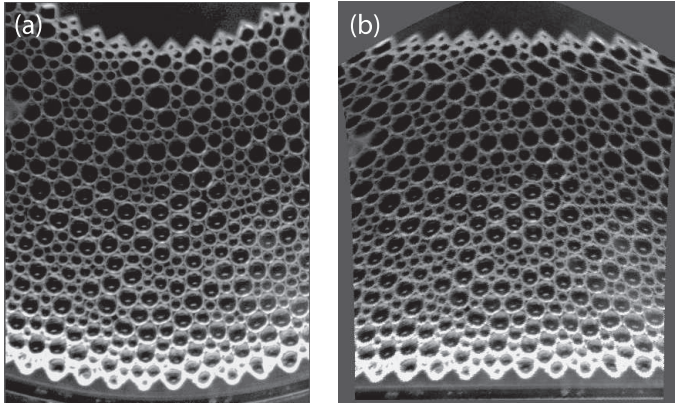
FIGURE 3.2: (a) Raw image as obtained by CCD camera. The local curvature is extracted from the curvature at the inner disc and the outer cylinder, and for every r we define an arc that we match to pixels in the image. If we plot these arcs as straight lines we obtain: (b) the image with correction for curvature. We compute cross correlations between subsequent frames on these straightened image lines.

3.3 Results

We shear the foam, covered with a glass plate at 6 different driving velocities, spanning 2.5 decades. Results are plotted in Fig. 3.3. We have rescaled the velocity profiles with the velocity at r_i to highlight the qualitative changes. We have rescaled the radial coordinate with the average bubble radius $\langle d \rangle$, to hightlight the steep decay of the velocity profiles. We only plot a limited region of r since all velocity profiles are strongly shear banded. When we thus zoom in, we observe that nevertheless, the shape of the velocity profiles depends on the exerted rate of strain, as in the linearly sheared foam: the runs that were recorded at the highest driving velocity exhibit the most shearbanding. This is in strong contrast with the findings by Debrégeas et al. [9], were rate independent profiles were found. This is striking because we operate at essentially the same shear rates and because having only one bounding plate in stead of two, as for the Hele-Shaw cell employed in [9] should matter little as regards the bubble-wall drag force. We do observe approximately exponentially decaying profiles (see inset of Fig 3.3).

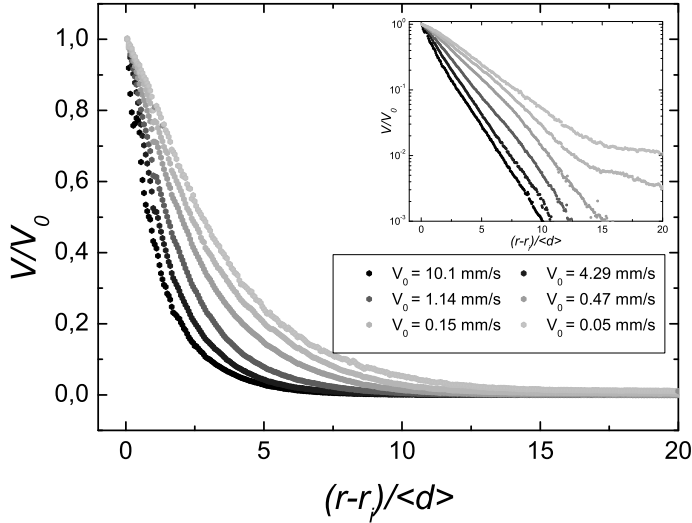The shear banding cannot a priori be attributed to the bubble-wall

FIGURE 3.3: Velocity profiles for two dimensional Taylor-Couette flow of foam with top plate. We see strongly shear banded velocity profiles that furthermore exhibit rate dependence: the faster the driving velocity, the more shear banded the profiles become. Inset highlights approximately exponential decay of velocity profiles.

drag as another inhomogeneity in the stresses due to the curvature is present. However, by comparing to the results in the linear geometry we can venture a guess that in the Couette geometry the rate dependence is again due to the fact that the bubble-bubble drag and the bubble-wall drag scale with different exponents. By applying the drag force balance model to the cylindrical geometry, we will investigate this question in section 3.5.

To be able to perform bubble raft experiments, we place spacers between the supports and the glass plate. By doing so the bubbles are no longer confined. If we now lower the inner wheel, we can shear the foam without drag from the top plate. However, the foam stability is strongly decreased and bubbles will pop after approximately $1\frac{1}{2}$ hours. Nevertheless, the bubbles are sufficiently stable that we can shear the foam at the same shear rates as in the experiments with a bounding glass plate, except for the slowest run. Results are plotted in Fig. 3.4: within experimental
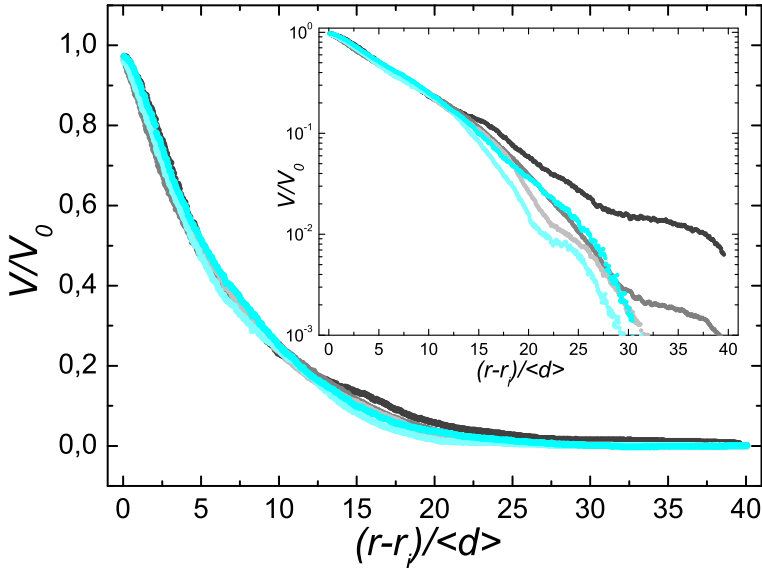
FIGURE 3.4: Velocity profiles for two dimensional Taylor-Couette flow of foam without top plate, the driving velocities are as in Fig. 3.3. We see approximately rate independent velocity profiles, with a curvature that is solely due to the curved geometry. We observe no discontinuous transition in the shear rate, as is evidenced by the log-lin inset, that furthermore highlights exponential decay near the inner disc.

uncertainty the profiles exhibit rate independent velocity profiles. We observe that the velocity profiles are still reasonably shear banded, but this curvature is due to the fact that the stresses decay as $1/r^2$ in the Couette geometry, as we will see later on. We furthermore observe no discontinuous transition between a flowing and a static region as was found by Rodts et al. [84] and Dennin and coworkers [68,71,87] experimentally and Cheddadi et al. theoretically [81].

3.4 Model

In this section we attempt to validate the drag force balance model developed for linear shear of two-dimensional foams by applying it to the circular case. We will proceed as follows: because the geometry has circu-
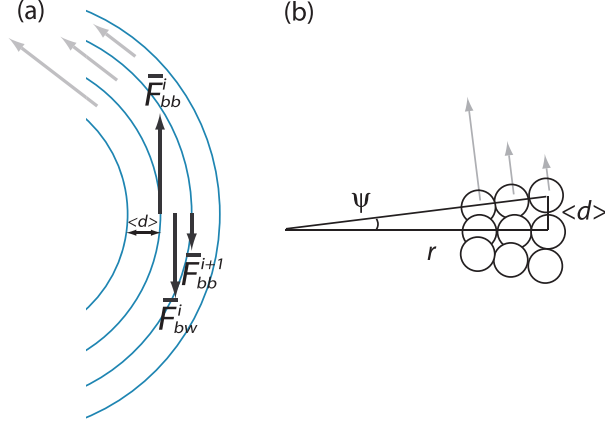
FIGURE 3.5: (a) Illustration of the model defined in Eq. (3.6): the light grey arrows indicate the velocity profile, while the black arrows indicate the resulting drag forces on lane i. (b) Schematic explanation of the additional term $v_i\langle d\rangle/r$ in Eqs. (3.3): bubbles in lane $i+1$ that have advanced by a distance $\langle d\rangle$ will exert a small inward drag force on bubbles in lane i of magnitude $[\sin\Psi \cdot v_i]^\beta$ with $\sin\Psi = \langle d\rangle/r$.

lar symmetry, this time instead of balancing drag forces on neighbouring lanes, we have to balance torques on neighbouring annuli, see Fig. 3.5. To arrive at the torques acting at lane i, we start with the expressions from Eq. (2.11) and adapt them to the circular geometry:

$$\overline{F}^i_{bw} = f_{bw}(\frac{\eta v_i}{\sigma})^{2/3}, \tag{3.1}$$

$$\overline{F}^i_{bb} = f_Y + f_{bb}\left[\frac{\eta}{\sigma}(v_{i-1} - v_i - v_i\langle d\rangle/r)\right]^\beta, \tag{3.2}$$

$$\overline{F}^{i+1}_{bb} = f_Y + f_{bb}\left[\frac{\eta}{\sigma}(v_i - v_{i+1} - v_i\langle d\rangle/r)\right]^\beta. \tag{3.3}$$

In both bubble drag forces a new term $v_i\langle d\rangle/r$ has appeared, and we can explain these in two ways. Firstly, it turns out to be crucial to ensure that the continuum limit of the circular drag force balance model agrees with the Cauchy equilibrium criterion in polar coordinates, see Appendix 3A, that states that a body force acting in the azimuthal direction is balanced

by:

$$\frac{\partial \tau}{\partial r} + \frac{2\tau}{r},\tag{3.4}$$

with τ the stress. Furthermore, the strain rate in polar coordinates reads:

$$\dot{\gamma} = r \frac{d}{dr}\left[\frac{v_\theta(r)}{r}\right] = \frac{dv_\theta(r)}{dr} - \frac{v_\theta(r)}{r}.\tag{3.5}$$

From Eq. (3.5) we can thus already see the necessity of including a term $v_i\langle d\rangle/r$.

Secondly, we can construct a tentative picture of the origin of these forces in the spirit of our drag force balance model. This picture is illustrated in Fig. 3.5(b): due to the curvature, bubbles that have advanced in the θ-direction by a distance $\langle d\rangle$ in lane $i + 1$ will exert a drag force in the inward radial direction, because these bubbles provide a steric hindrance for the bubbles in the i-th lane to move straight on. Similarly, bubbles that lag behind by a distance $\langle d\rangle$ will push the bubble in lane i outward. The radial component of the associated bubble velocity is given by $v\langle d\rangle/r$, thus giving rise to that additional term.

In the circular geometry we balance torques, and hence we balance the force per bubble times the number of bubbles $N^i \equiv 2\pi r/\langle d\rangle$ on rings of circumference $2\pi r$ and width $\langle d\rangle$, the average bubble diameter. The force balance then reads:

$$N^{i-1}2\pi(r - \langle d\rangle/2)\overline{F}_{bb}^i - N^i 2\pi r \overline{F}_{bw}^i - N^{i+1}2\pi(r + \langle d\rangle/2)\overline{F}_{bb}^{i+1} = 0.\tag{3.6}$$

The torque due to the bubble-bubble drag forces is evaluated a distance $\langle d\rangle/2$ from the center of bubble lane i. While this is indeed where this drag force acts, we did not need to specify this in the linear geometry. Again however, it turns out that specifying this distance is crucial to match the continuum limit to Eq. (3.4).

Since the resulting relative velocity vectors deviate by an angle $\Psi = \arcsin(\langle d\rangle/r)$ from the θ-direction, a factor $\sin(90\pm\psi) = \sqrt{1 - (\langle d\rangle/r)^2} \approx 1 - \frac{1}{2}(\langle d\rangle/r)^2$ should be added in the viscous part of the bubble-bubble drags, but this is of higher order in $\langle d\rangle/r$ and we ignore it. The resulting

expression can be written as:

$$(2\pi r)^2 f_{bw} \left[\frac{\eta v_i}{\sigma}\right]^{\frac{2}{3}} = [2\pi(r - \frac{\langle d \rangle}{2})]^2 \left(f_Y + f_{bb} \left[\frac{\eta}{\sigma}(v_{i-1} - v_i(1 + \frac{\langle d \rangle}{r}))\right]^{\beta}\right)$$

$$-[2\pi(r + \frac{\langle d \rangle}{2})]^2 \left(f_Y + f_{bb} \left[\frac{\eta}{\sigma}(v_i(1 - \frac{\langle d \rangle}{r}) - v_{i+1})\right]^{\beta}\right) \quad (3.7)$$

We can rewrite this as follows:

$$k(\frac{\eta v_i}{\sigma})^{2/3} = \left(1 - \frac{\langle d \rangle}{2r}\right)^2 \left[\frac{\eta}{\sigma}(v_{i-1} - v_i(1 + \frac{\langle d \rangle}{r}))\right]^{\beta}$$

$$- \left(1 + \frac{\langle d \rangle}{2r}\right)^2 \left[\frac{\eta}{\sigma}(v_i(1 - \frac{\langle d \rangle}{r}) - v_{i+1})\right]^{\beta}$$

$$- \frac{2 f_Y \langle d \rangle}{f_{bb} r}, \quad (3.8)$$

with $k = \frac{f_{bw}}{f_{bb}}$. We can take the units of length in which we measure - which is the average bubble diameter $\langle d \rangle$ and which we measure in units of the pixel length p - into account explicitly by making the substitution $f_{bb} \to f_{bb}^*$ with $f_{bb}^* = f_{bb}/(\langle d \rangle/p)^{1+\beta}$, which is the scale factor on the left hand side of Eq. (2.16).

3.4.1 Continuum limit

We have already stated that it is crucial to check if our numerical model is physically correct by comparing the continuum limit to Eq. (3.4). If we neglect quadratic terms in $\langle d \rangle/r$ we find from Eq. (3.7) (note that $\lim_{\langle d \rangle \downarrow 0} \langle d \rangle \frac{v_{i-1} - v_i}{\langle d \rangle} = -\frac{\partial v(r)}{\partial r}$):

$$k(\eta v_i/\sigma)^{2/3} = \langle d \rangle \frac{\partial}{\partial r} \left(\frac{\eta \langle d \rangle}{\sigma}(\frac{\partial v(r)}{\partial r} - \frac{v}{r})\right)^{\beta}$$

$$+\frac{2\langle d \rangle}{r} \left[\left\langle \left(\frac{\eta \langle d \rangle}{\sigma}(\frac{\partial v(r)}{\partial r} + \frac{v}{r})\right)^{\beta}\right\rangle + \frac{f_Y}{f_{bb}}\right]. \quad (3.9)$$

From Eq. (3.9), we can immediately deduce that the continuum limit of our model indeed satisfies both Eqs. (3.4) and (3.5) and that

$$\tau = \left(\frac{\eta \langle d \rangle}{\sigma} \dot{\gamma}\right)^{\beta} + \frac{f_Y}{f_{bb}}. \quad (3.10)$$
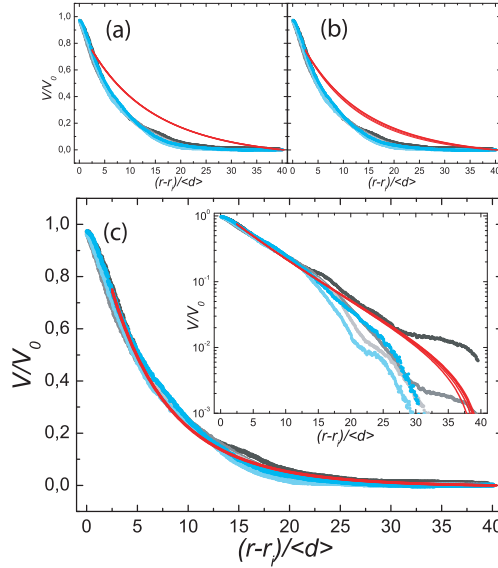
FIGURE 3.6: (a)+(b)+(c): Data from Fig. 3.3. (a)+(b): Solid lines are solutions to the drag force balance model defined in Eq. (3.8), with $k = 0$ since top plate drag is absent, $\beta = 0.36$ and $f_Y = 0$ (a) or $f_Y = 1.2 \times 10^{-5}$ N (b). Clearly, for $\beta = 0.36$ the fits are far off (a), whereas setting f_Y to the value found in Fig. 2.12(b) results in a small rate dependence which is in fact more pronounced for fits with $\beta = 0.20$. (c) Solid lines are model profiles with $\beta = 0.20$ and $f_Y = 0$. Inset shows data on a lin-log scale: both the model and the experimental profiles curve downwards, since they have to obey $v(r_o) = 0$.

Eq. (3.5) shows the necessity of introducing the terms $v_i d/r$ in the drag forces $\overline{F}_{bb}$: it accounts for the curvature term in the ensuing continuum version of the model.

3.5 Fits

3.5.1 Flows without a top plate

We match solutions of our curved drag force balance model Eq. (3.8) to the experimental velocity profiles in the following way. For the case without a top plate, $f_{bw} = 0$ and hence the constant $k = 0$. Thus our model

70

simplifies, and only contains two fit parameters: the exponent β, and the yield force f_Y. Surprisingly, when we take for beta the value obtained from the linear geometry and rheology, $\beta = 0.36$, we have not been able to obtain a convincing fit, see Fig. 3.6(a). Moreover, using in addition the estimate of f_Y from rheology, see Fig. 2.12(b), makes the fits even worse, see Fig. 3.6(b), as it introduces a small rate dependence. However, a good fit to the model can be obtained by taking $\beta = 0.20 \pm 0.02$ and f_Y at least one order of magnitude smaller than the value from Fig. 2.12(b) $\rightarrow f_Y \leq 1.2 \times 10^{-6}$. The yield drag then essentially has no influence on the shape of the model fits and we could as well set it zero.

We show the data, fit to solutions of the model with $\beta = 0.20$, $k = 0$ and $f_Y = 1.2 \times 10^{-6}$ N in Fig. 3.6: the model solutions fit reasonably well to the data and correctly capture the rate-independence for the bubble raft experiment.
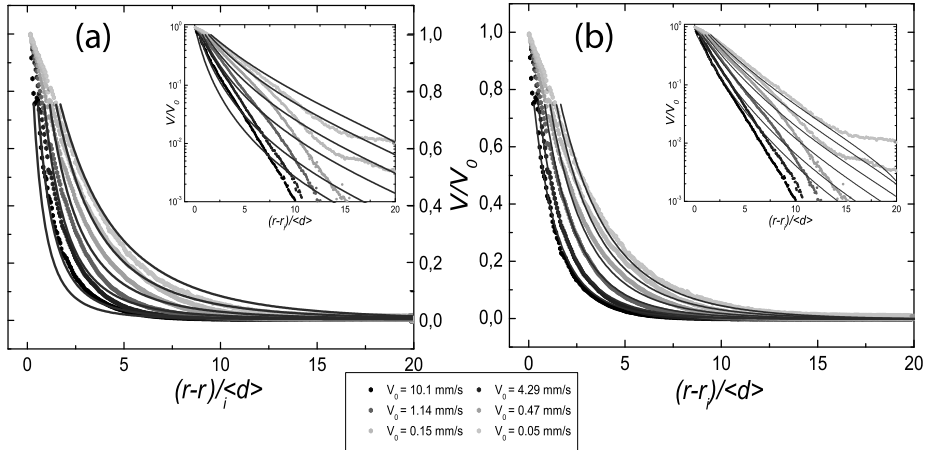
3.5.2 Flows with a top plate

FIGURE 3.7: (a) Same data as in Fig. 3.4. Solid lines are solutions to the drag force balance model defined in Eq. (3.8), with $k =15.5$ $\beta =0.20$ and $f_Y = 0$ N. (b) Again data from Fig. 3.4. Solid lines are solutions to the drag force balance model, with $k =5.5$ $\beta =0.36$ and $f_Y = 0$ N. The quality of the fit is markedly improved.

For the case with a top plate, we have in principle three fit parameters.

To extract the optimal value of β we look for a minimum in the spread of k over all six runs while setting $f_Y = 0$ — setting $f_Y = 1.2 \times 10^{-5}$ yields poor fits. For every $0.30 < \beta < 0.60$ there seems to a rather good fit to all the profiles if k is tuned properly, and only at $\beta < 0.30$ the spread in k-values increases significantly. For $\beta = 0.20$ the model profiles fit downright poorly, Fig. 3.7. We also show fits to the data with k =5.5 and β =0.36 to highlight the fact that we can reproduce the correct trend in rate dependence and obtain rather good fits in the range $0.30 < \beta < 0.60$.

3.6 Local rheology and power-law fluids

As discussed above, the value of the yield drag force f_Y we extracted from our fits is anomalously small compared to the value found from bulk rheometry. This could be either due to the yield stress being much lower locally than what is measured in bulk rheometry [88], consistent with the idea of a static and dynamic yield stress. Another option is that a local stress strain relation is not satisfied throughout the gap, placing severe restrictions on the validity of comparing the experimental velocity profiles with the model profiles. Finally, the yield stress could simply not play a role in these foam flows. Another issue is the conflicting value of the β extracted from our fits and β as established in chapter 2: the bubble raft experimental profiles are best fit with a $\beta = 0.20 \pm 0.02$ which is much lower than $\beta = 0.36$ found in chapter 2.

We will investigate these issues in two ways. The first is by fitting the velocity profiles obtained in the freely flowing bubble raft to the analytical prediction for velocity profiles of power law fluids (hence without a yield stress) in a Couette geometry, to see if a yield stress is needed to fit the velocity profiles. We will then present additional measurements obtained by simultaneously imaging the velocity profiles and measuring the bulk rheometrical response of a two dimensional bubble raft in a Taylor-Couette geometry. This allows us to investigate the local rheology of the foam in the spirit of [79] and connect bulk rheometry with local measurements as well as our model solutions.
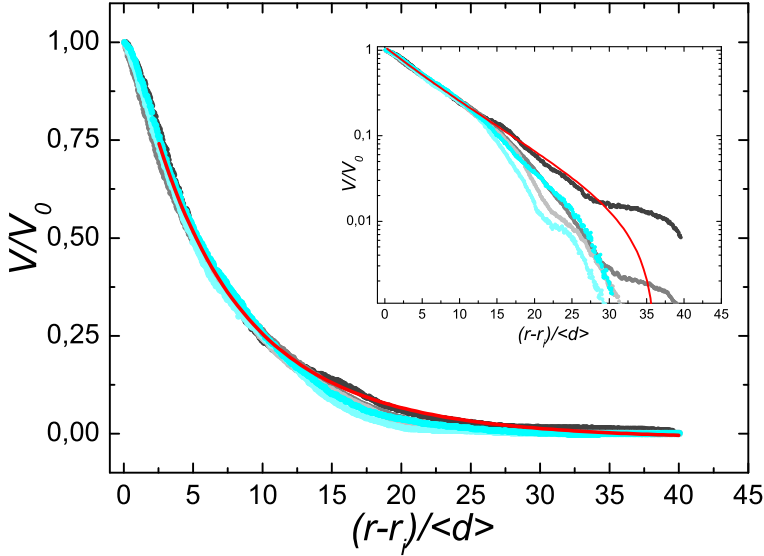
FIGURE 3.8: Velocity profiles for foam without top plate with analytical solution to Eq. (3.11). Note the reasonable agreement, even though this model does not consider a yield stress.

3.6.1   Fit to a power-law fluid model

If the yield stress is assumed to be absent, one can analytically solve the following equation for the stresses in the system:

$$\tau(r) = \frac{T}{r_i r^2} = k \left(\frac{\eta \langle d \rangle}{\sigma} \right)^{\beta} \dot{\gamma}^{\beta} \equiv C \left(r \frac{d}{dr} \frac{v_{\theta}(r)}{r} \right)^{\beta}. \qquad (3.11)$$

The solution to this differential equation is given in Appendix B. We can vary β and obtain an optimal match with the experimental velocity profiles obtained in the shear cell without top plate for $\beta = 0.20$. The analytical velocity profile adequately fits the data and the value of β is in good agreement with the exponent found previously by fitting the model profiles to the experimental data. This strongly indicates that the yield stress has a negligibly low influence on the shape of the velocity profiles and that we can essentially understand the shape of the experimental velocity profiles to stem from the power-law fluid nature of the two dimensional

foam, without accounting for the yield stress. The question remains, how-ever, *why* we do no observe a yield stress and *what* sets the anomalously low exponent.

3.6.2 Rheometry: an anomalous local flow rule

We can try to see if a local flow rule describes the foam rheology throughout the system, as this would validate fitting a local drag force bal-ance model to the experimental profiles as well as show possible non-local effects that might influence the flow in this system. To this end, we shear a bidisperse monolayer of foam bubbles in an Anton Paar DSR 301 rheome-ter. We again employ a Taylor-Couette geometry, but this time we can measure torques on the inner cylinder which is connected to the rheome-ter head (lower inset of Fig. 3.9). We impose five different strain rates, spanning two decades in total and measure the resulting average torque, while simultaneously imaging the bubble motion from which we can cal-culate the averaged velocity profiles. The radii of the inner disc and the outer ring are $r_i = 0.025$ m and $r_o = 0.07$ m. The resulting velocity pro-files are displayed in Fig. 3.9: within experimental uncertainty the profiles are rate independent, as well as strongly localized. Again we observe no discontinuity in the local strain rate.

We fit solutions of the drag force balance model to the velocity profiles and we obtain optimal fits for $\beta = 0.20 \pm 0.02$ and $f_Y = 0$ (red curves in Fig. 3.9). Clearly, these fits do not extend over the whole velocity profile and we will shortly see this is due to the absence of a local flow rule near the inner disc.

We will now calculate local stresses and strain rates throughout the gap of our Couette cell, with a method that was utilised in [79, 85, 89]. From the Cauchy equilibrium condition we know that the stresses in the system are given by (see Appendix 3.A for details):

$$\tau(r) = \tau(r_i) r_i^2 / r^2. \tag{3.12}$$

Furthermore, we can take the appropriate derivative, Eq. (3.5), of the ve-locity profile:

$$\dot{\gamma} = r \frac{d}{dr} \left[\frac{v_\theta(r)}{r} \right] \tag{3.13}$$

to obtain the local strain rate $\dot{\gamma}(r)$. We then have for each r-coordinate a value of the local stress and the local strain rate and we can thus plot
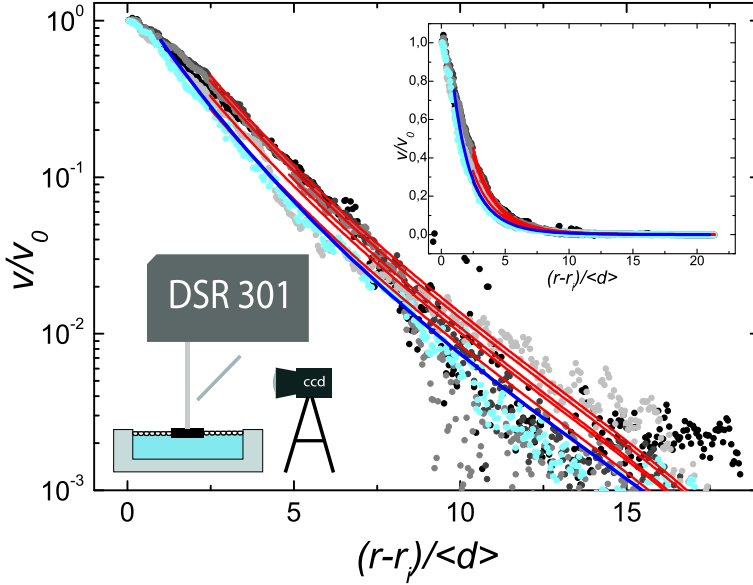
FIGURE 3.9: Averaged velocity profiles plotted on log-lin scale from a bubble raft sheared in Taylor-Couette geometry with inner disc driven by rheometer head. Solid lines: fits to drag force balance model with $\beta = 0.20 \pm 0.02$ and $f_Y = 0$. Upper inset shows same plot on linear scale to highlight the part of the profile where one can fit. Blue curve: Velocity profile for power-law fluid (analytical solution Eq. (3.11)) with $\beta = 0.22$. Lower inset: schematic picture of the setup.

the local stress as a function of the local strain rate, which is displayed in Fig. 3.10. The local rheology of the experimental velocity profiles is given by the five scatter plots ranging from black to light blue.

If there truly were a local flow rule then al these profiles would collapse onto one master curve. However, we can clearly see from Fig. 3.10 that all profiles start to deviate from the flow curve at a point — labeled by a yellow square in Fig. 3.10 — close to the inner cylinder, where the local stresses are high.

A direct consequence is that fitting the velocity profiles with our local drag force balance model at a radial distance that is closer to the inner cylinder than this divergence point is useless. If we, however, restrict ourselves to the parts of the velocity profiles where the local flow rule is obeyed we can excellently fit our experimental data (see Fig. 3.9).
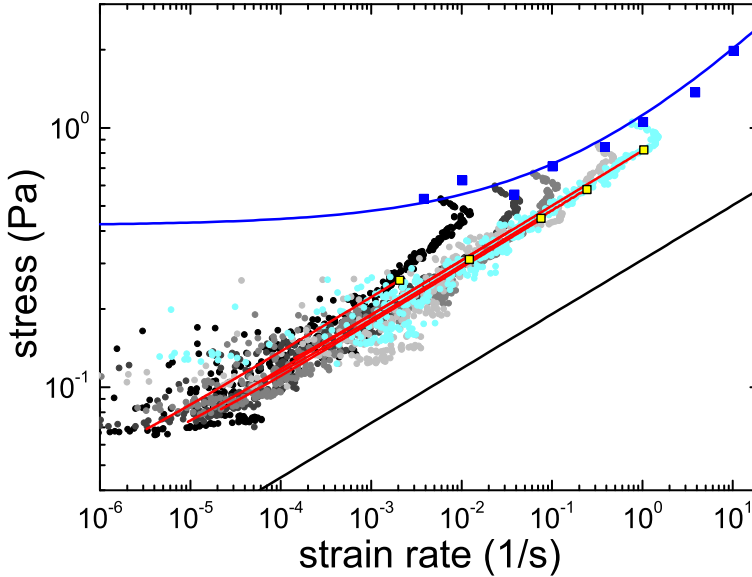
FIGURE 3.10: (b) Local stress-strain relation extracted from velocity profiles in Fig. 3.9: The local strain rate can be calculated from the velocity profiles and the stress is known from the measured torque. Scattered data: local stress-strain relation for experimental profiles. Red solid lines: Model profiles from Fig. 3.9. Yellow squares: maximal value of the local rate at which a local flow rule — and hence the fit — holds. Blue dots: bulk rheometrical measurements. Solid blue line: Herschel-Bulkley fit through bulk data points: $0.42 + 0.7\dot{\gamma}^{0.36}$. Black line: power law with slope 0.21.

The red lines in Fig. 3.10 denote the local stress- strain rate behaviour of the model profiles and not surprisingly, since these profiles are essentially solutions to a power-law constitutive equation (Eq. (3.9), with $f_Y = 0$) they nicely collapse and scale as $\dot{\gamma}_l^{0.21}$ as shown by the solid black line.

The blue squares denote the measured torque at the inner disc for the corresponding velocity profiles plus two additional data points at high shear rate to facilitate fitting a Herschel-Bulkley expression (solid blue line). We cannot image at sufficiently high frame rates to record the flow at these high shear rates and thus we have no information on the local rheology there.

3.7 Discussion

Three things strike the eye in Fig. 3.10: *i)* Both experimental profiles and the model solutions exhibit a local flow rule that reads $\tau \propto \dot{\gamma}^{0.21}$, in clear contradiction with the previously found exponent $\beta = 0.36$. Nevertheless, this value 0.21 is in good agreement with the exponent extracted from fitting an analytical power-law fluid model to the experimental velocity profile. It is also consistent with the optimal fits of the model profiles in both Fig. 3.6(c) and Fig. 3.9.

ii) By plotting the bulk stress and strain rate as measured by rheometry and the corresponding Herschel-Bulkley fit we see that, in the tails of the velocity profile, the foam still flows well below the global yield stress. This confirms the finding that the optimal fits from the drag force balance model were obtained at f_Y at least one order of magnitude lower than the value as found in bulk rheometry: the global extrapolated yield stress in Fig. 3.10 is far above the local stresses, in fact we do not observe a yield plateau for our range of local strain rates.

iii) Due to the large stress and strain rate gradients near the inner disc, one apparently only measures the non-local flow behaviour with the rheometer and one can thus measure a different rheology with the rheometer — $\tau = \tau_Y + k\dot{\gamma}^{0.36}$ — than what actually governs the local flow, which reads $\tau = k\dot{\gamma}^{0.21}$. This finding is in clear contrast with [85] where, for wide-gap Couette rheometers the local and global flow behaviour obey exactly the same constitutive equation. However, the large local strain rates near the inner disc in our experiment might give rise to a non-local rheology in the spirit of Goyon et al. [79], where rearrangements in the shearing zone lead to cooperative flows in the shear bands.

Since measuring an exponent $\beta = 0.36$ seems to be a result of non-typical rheology close to the inner disc, it is an open question why a local strain rate scaling with $\beta = 0.36$ describes *linear* shear flow of two-dimensional foams bounded by a glass plate so well. We hypothesise it might have to do with the type of flow in the foam: optical inspection of foam regions where the local strain rate is very low, evidence qualitatively different behaviour between the bubble raft flow and the liquid-glass flow. A qualitative difference in the fluctuations might well be at the root of this behaviour, and we will present a simple optical technique that seems to support this explanation in chapter 5. This would also explain the poor fit with $\beta = 0.20$ of the rate dependent runs in Fig. 3.6(b).

3.8 Conclusion

We have measured velocity profiles in a two-dimensional foam monolayer, undergoing cylindrical (Taylor-Couette) shear. We have adapted our drag force balance model to the circular geometry and have obtained model fits that adequately fit the experimental data for the foam without a top plate, with a bubble-bubble drag force exponent $\beta = 0.20$, much smaller than was measured in the linear geometry. Also, the yield stress required to obtain good fits is either zero or at least one order of magnitude smaller than the value previously obtained from two-dimensional rheometry. In order to elucidate the role of the yield stress and non-locality on our foam flow we have performed additional rheometry and velocimetry on foams in a smaller Taylor-Couette geometry. From these measurements we can extract the local stress-strain rate relation throughout our sample and we observe a local flow rule $\tau \propto \dot{\gamma}^{0.20 \pm 0.02}$, from which deviations occur close to the inner cylinder that place a bound on the range of the velocity profiles to which we can fit our model. Furthermore, the foam appears to flow at stresses well below the yield stress.

Fitting the analytical expression for velocity profiles for power-law fluids (hence without a yield stress) to the experimental profiles yields a power-law index 0.21, in good agreement with the directly measured local stress-strain rate relation.

Appendices

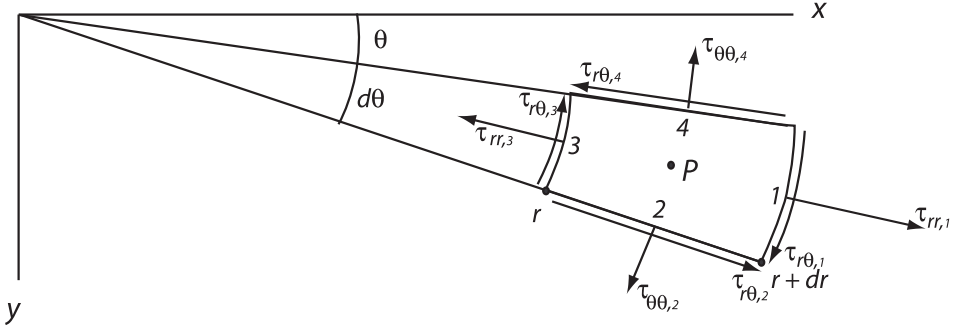## 3.A   Stress and strain rate in polar coordinates

FIGURE 3.11: Infinitesimal element used to derive Cauchy equilibrium in polar coordinates.

A consideration of the stresses and strains in the Couette experiment is best performed in polar coordinates (r, θ), which are related to Cartesian coordinates through

$$r = \sqrt{x^2 + y^2} \quad , \quad \theta = \arctan(y/x), \tag{3.14}$$
$$x = r\cos(\theta) \quad , \quad y = r\sin(\theta) \tag{3.15}$$

3.A.1   Stress equilibrium

We will here follow the excellent geometrical derivation of the Cauchy equilibrium condition for the stresses and strain(rate) in polar coordinates found in [90]. Consider a infinitesimally small element with vertices located at (r, θ), $(r, \theta + d\theta)$, $(r + dr, \theta + d\theta)$ and $(r + dr, \theta)$ (see Fig. 3.11). We can then find the Cauchy equilibrium conditions by looking at the radial and the tangential force balance at P separately.

The radial force on side 1 is $\tau_{rr,1}(r + dr)d\theta$ and similarly the radial force on side 3 is $-\tau_{rr,3}rd\theta$. The normal force on side 2 has a component along the radial direction of $-\tau_{\theta\theta,2}dr\sin(d\theta/2) \simeq -\tau_{\theta\theta,2}drd\theta/2$ as does the normal force on side 4: $-\tau_{\theta\theta,4}drd\theta/2$. The shear stresses result in a force

$(\tau_{r\theta,2} - \tau_{r\theta,4})dr$. If we sum up these forces and include a body force R we obtain the equation of equilibrium in the radial direction:

$$\tau_{rr,1}(r+dr)d\theta - \tau_{rr,3}rd\theta \quad - \quad \tau_{\theta\theta,2}drd\theta/2 - \tau_{\theta\theta,4}drd\theta/2$$
$$+ \quad (\tau_{r\theta,2} - \tau_{r\theta,4})dr + Rrd\theta dr = 0. \quad (3.16)$$

If we divide this by $drd\theta$ we find:

$$\frac{\tau_{rr,1}(r+dr) - \tau_{rr,3}r}{dr} - \frac{\tau_{\theta\theta,2} + \tau_{\theta\theta,4}}{2} + \frac{\tau_{r\theta,2} - \tau_{r\theta,4}}{d\theta} + Rr = 0. \quad (3.17)$$

By taking the limit $dr, d\theta \downarrow 0$ we find the equilibrium condition for the radial stresses:

$$\frac{\partial(r\tau_{rr})}{\partial r} + \tau_{\theta\theta} + \frac{\partial\tau_{r\theta}}{\partial\theta} + rR = 0. \quad (3.18)$$

Dividing by r yields the normally encountered expression:

$$\frac{\partial\tau_{rr}}{\partial r} + \frac{1}{r}\frac{\partial\tau_{r\theta}}{\partial\theta} + \frac{\tau_{rr} - \tau_{\theta\theta}}{r} + R = 0. \quad (3.19)$$

For the tangential stress balance we can perform the exact same analysis and we find the balance to read:

$$(\tau_{\theta\theta,2} - \tau_{\theta\theta,4})dr + (\tau_{r\theta,4} - \tau_{r\theta,2})drd\theta + (\tau_{r\theta,1}(r+dr) - \tau_{r\theta,1}r)d\theta = 0. \quad (3.20)$$

By taking the limit $dr, d\theta \downarrow 0$ we find the tangential stress balance, which reads:

$$\frac{1}{r}\frac{\partial\tau_{\theta\theta}}{\partial\theta} + \frac{\partial\tau_{r\theta}}{\partial r} + 2\frac{\tau_{r\theta}}{r} = 0. \quad (3.21)$$

3.A.2 Strain and strain rate

While the expression for the strain rate can be obtained by straightforward coordinate substitution [91], one can again consider an infinitesimal element that is deformed by an amount w in the radial direction and u in the tangential direction. A detailed derivation is given in [90]. We will restrict ourselves to stating the results. The shear strain $\gamma_{r\theta}$ is given by:

$$\gamma_{r\theta} = \frac{\partial w}{r\partial\theta} + \frac{\partial u}{\partial r} - \frac{u}{r}. \quad (3.22)$$

Due to the rotational symmetry, the first term is 0. If we take the time-derivative we find the shear strain rate:

$$\dot{\gamma}_{r\theta} = \frac{\partial v}{\partial r} - \frac{v}{r} = r\frac{\partial}{\partial r}\left[\frac{v}{r}\right]. \quad (3.23)$$

3.B Velocity profiles for a power-law or a Herschel-Bulkley fluid in a curvilinear geometry

In a Taylor-Couette Geometry with inner and outer radii r_i and r_o, Eq. (3.21) dictates the balance of stresses in the tangential direction. Since the flow has rotational symmetry, all the terms in Eq. (3.19) equal 0 and in the tangential stress balance, $\frac{1}{r}\frac{\partial \tau_{\theta\theta}}{\partial \theta} = 0$. Eq. (3.21) then reads:

$$\frac{\partial \tau_{r\theta}}{\partial r} + 2\frac{\tau_{r\theta}}{r} = 0. \tag{3.24}$$

The solution to this differential equation is given by

$$\tau(r) = \tau(r_i)r_i^2/r^2. \tag{3.25}$$

For a power-law fluid, the stresses are balanced by the local strain rate [68]:

$$\tau(r) = \frac{\tau(r_i)r_i^2}{r^2} = k\dot{\gamma}^\beta = k\left[r\frac{\partial}{\partial r}\left(\frac{v}{r}\right)\right]^\beta. \tag{3.26}$$

This simplifies to:

$$\frac{(\tau(r_i)r_i^2)^{1/\beta}}{r^{2/\beta+1}} = \frac{\partial}{\partial r}\left[\frac{v}{r}\right]. \tag{3.27}$$

Which can be directly integrated, yielding:

$$\frac{v(r)}{r} = \frac{\beta}{-2}\frac{(\tau(r_i)r_i^2)^{1/\beta}}{r^{2/\beta}} + C \tag{3.28}$$

The integration constant C can be evaluated by requiring that $v(r)/r = 0$ at $r = r_0$. Thus we end up with:

$$v(r) = \frac{\beta}{2}(\tau(r_i)r_i^2)^{1/\beta}r\left[\frac{1}{r_o^{2/\beta}} - \frac{1}{r^{2/\beta}}\right] \tag{3.29}$$

We can of course add a yield stress term to the right hand side of Eq. (3.26), to model a Herschel-Bulkley fluid. However, an analytical solution is then no longer available, and one then needs to resort to numerical integration.

PACKING FRACTION AND JAMMING

The experiments described in Chapters 2 and 3 have been performed at a fixed gap between the liquid surface and the glass plate. However, by increasing or decreasing this gap we can vary the packing density of the foam [61, 92]. While the precise relation between the gap and the packing density is nontrivial we can understand the main trend as follows: it is energetically favorable for the bubbles to contact both the glass top plate and the fluid phase. Hence, increasing the gap stretches the bubbles vertically, and more bubbles can be packed per unit area. The change in bubble shape is such that the size of the contacts between bubbles increases, and the liquid fraction in horizontal cross sections decreases — effectively, the liquid fraction goes down, and seen from above, the foam looks 'dry'. Similarly, decreasing the gap leads to pancake shaped, circular bubbles [18] and the foam becomes 'wet'. Clearly, there are limits to the range of available liquid fractions, as the bubbles form multilayers as the gap is increased too much.

As we will explain below, we will quantify the wetness of the foam by an effective packing fraction ϕ, which essentially can be thought of as the 2D packing fraction of the gas bubbles seen in the midplane between fluid surface and top plate. Hence, the dry limit corresponds to $\phi \approx 1$, while the wet limit corresponds to $\phi \approx 0.84$ [23, 33, 93]. In practice, our data is limited to the range $0.855 \lesssim \phi \lesssim 0.975$.

In this chapter, in section 4.1, we first establish how to extract the packing fraction ϕ from the experimental images, and also define an algorithm that determines whether neighboring bubbles are in contact or not. We

then compare the scaling of the contact number Z with packing fraction ϕ, and find, for the first time for a system of frictionless deformable spherical entities, that our data agrees well with the square-root scaling established in the seminal papers of Durian [23] and O'Hern et al. [6].

In section 4.2, we probe the role of the packing density for the flow of foams in the linear shear cell. Clearly, varying the gap, which implies stretching the bubbles, varying their contact area and varying ϕ, should have a significant impact on the shape of the velocity profile, since the size of the deformed facets between neighboring bubbles influences the magnitude of their drag forces. By varying the driving rate in the shear cell for a range of packing fractions, we establish that the exponent governing the averaged bubble-bubble drag forces (β) is independent of ϕ, while the proportionality factor k, which measures the ratio of the pre-factors f_{bb} and f_{bw}, see chapter 2, varies strongly with liquid fraction. We will argue that the main variation in k will be due to variations of the bubble-bubble interactions, characterized by f_{bb}.

In section 4.3, we explore the use of our foam to study aspects of scaling near the jamming transition of frictionless deformable spherical entities. We first study the distribution of free area per bubble by means of a Voronoi area distribution in our foam, we then estimate the inter-bubble contact force distributions and finally present preliminary measurements on the variation of the static shear modulus G with packing fraction ϕ.

4.1 Varying and measuring ϕ

In order to vary ϕ, we vary the gap width between the glass plate and the bulk solution between 3 and 0.2 mm. We do this by adding or retracting fluid from the reservoir. To have a homogeneous gap between the liquid surface and the glass plate, we place additional supports under the glass plate to prevent sagging of the top plate during the runs. We monitor the gap width with a Mitutoyo digital depth gauge. If the gap becomes smaller than 0.2 mm the bubbles unjam [92]. This might be due to the fact that the gap is then of the size of the Plateau borders that connect the flat film between the bubble and the glass plate and the flat film between neighbouring bubbles, and hence the latter vanishes. If the gap becomes larger than 3 mm the foam buckles and develops a three dimensional structure.

If we stay between these limits the system we study is jammed and
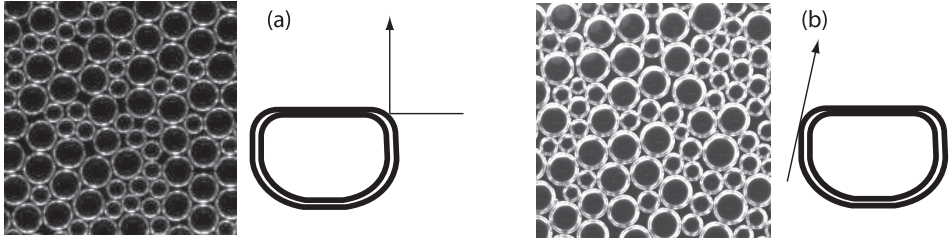
FIGURE 4.1: (a). Images as used in chapter 2 and 3: lateral lighting reflects off the Plateau border and which bubbles do actually touch is unclear. (b) Images obtained by lighting slanted from below. Contacts are now clearly visible.

quasi two-dimensional. However, determining a liquid fraction is not trivial, since various horizontal cuts through the bubble layer will yield different values. Various measures can be employed. First of all, one could try to relate the liquid fraction to the gap between the liquid surface and the glass plate. This distance, however, does not unambiguously set ϕ in our experiment: we observe a large hysteresis effect, i.e., increasing or decreasing the gap to a certain value does not yield the same packing fraction ϕ. We speculate this is due to the fact that the bubbles are not confined in the lateral direction i.e., the bubbles are not contained by side-walls. As a result, ϕ actually depends on both the gap distance and an ill defined confining pressure, which itself may be history dependent.

Another measure that has been derived in [61] relates the measured length of the deformed facets of the bubbles just before a T1 event to ϕ. In our experiments, though, we have found no well defined cut-off for such T1-events. It is not clear how the occurrence of T1-events can precisely be defined, since there is no obvious separation of the deformation scales during and outside of a T1-event.

4.1.1 Direct measure of ϕ from experimental images

In view of the difficulties outlined above, we measure ϕ by direct imaging as the two dimensional area fraction that is occupied by bubbles in our system. The lighting is crucial here, since clearly we image a highly nonlinear medium, and the observed bubble shape is a complex function of its true three dimensional shape. In the previous chapters, the bubbles were lit laterally. As a result, light was reflected towards the camera at the
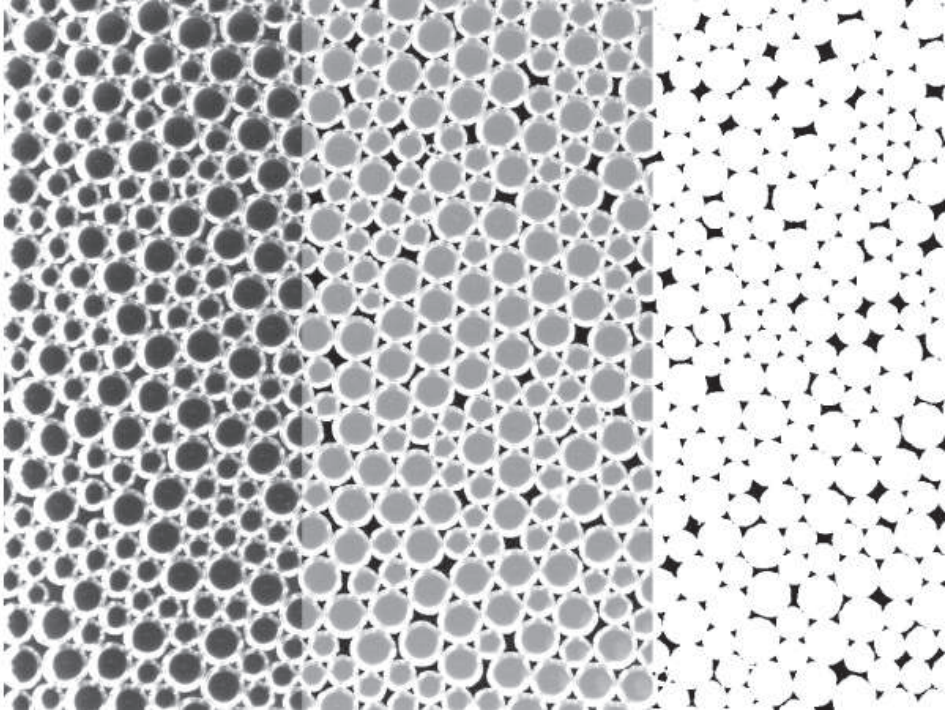
FIGURE 4.2: From left to right (1) Raw image. (2) Raw image with bubble areas superposed. Note the good agreement. (3) Only bubble areas in white.
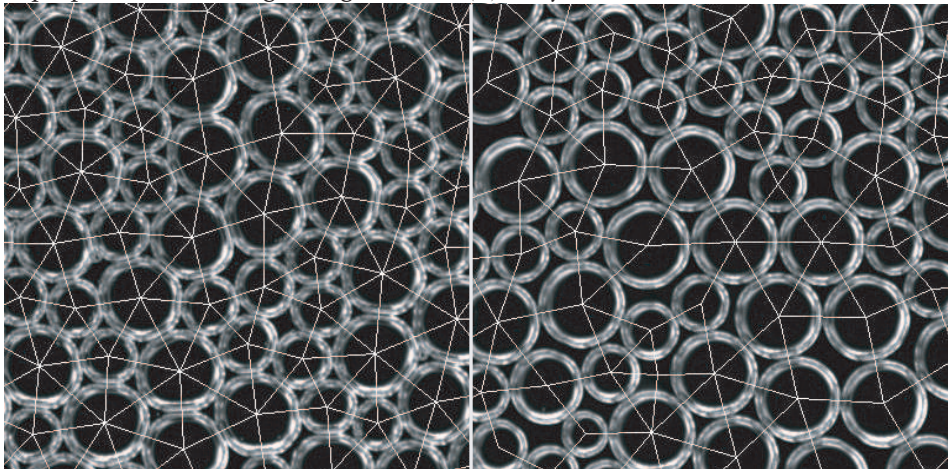

FIGURE 4.3: left-hand image: contacts as determined from Delaunay triangulation for a dry foam $\phi = 0.965$, right-hand image: contacts as determined for a wet foam, $\phi = 0.875$.

point were the Plateau border was under an angle of $45°$ with the vertical, see Fig. 4.1(a), resulting in rings that are smaller than the maximum lateral bubble cross-section. By switching to lighting the bubbles slanted from below we can visualise the full bubble diameter, see Fig. 4.1(b).

The procedure to extract ϕ from the images is illustrated in Fig. 4.2. We first binarise the images, after which both the bubble centers and the interstices appear bright. We remove the interstices by morphological operations. We then invert the binarised image and fill up the remaining bubble contours with a dilated version of the bubble centers. We check that the resulting bright disc optimally matches the original bubble contour, see Fig. 4.2. We then calculate the ratio of white pixels over the total number of pixels and hence obtain a reasonable estimate of ϕ.

We find that in the linear shear cell the accessible range in ϕ is $0.86 \lesssim \phi \lesssim 0.97$. It should be noted that for the runs performed at fixed wetness, discussed in the previous chapters, we find $\phi = 0.965 \pm 0.005$, in reasonable agreement with previous reports on the maximum ϕ that can be obtained in our type of setup [61].

4.1.2   The contact number Z and its scaling with ϕ

We can perform a consistency check on our measurements of ϕ by looking at the corresponding averaged number of contacts per bubble Z. By comparing to theoretical results, we can check whether the measured values of Z and ϕ correlate as expected and hence we have another indication of ϕ.

We extract Z from the images as follows. Starting from experimental images such as Fig. 4.3(a), we first locate the center of mass of the bubbles. We then perform a Delaunay triangulation on the resulting grid of points. All grid points are thus connected to all their nearest neighbours. However, not all neighbours are actually in contact. To remove the false contacts we measure the pixel intensity in the corresponding "ϕ-plot", see Fig. 4.2(c), along the vectors connecting any two bubbles, see Fig. 4.4. We then count the number of contacting bubbles for bubble and calculate the average over a large number of bubbles and images. Examples for a wet and a dry foam are depicted in Fig. 4.3: the left picture is of a dry foam, for which the gap between the glass plate and the liquid is large, the bubbles are strongly deformed and stretched, while the right picture is of a wet foam, for which the gap between liquid and glass plate is small, the bub-
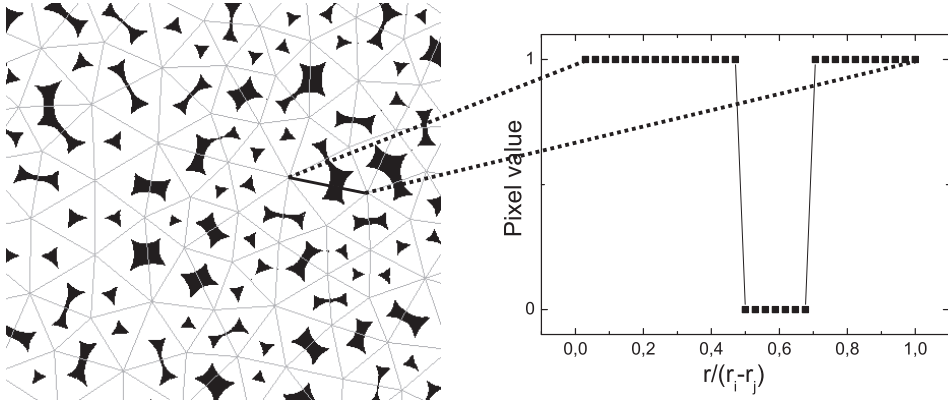
FIGURE 4.4: Plot of graph used to extract ϕ with Delaunay triangulation over-plotted. To calculate Z, vectors that connect two bubbles that do not touch are removed by looking for a dip in the pixel intensity along the vector.

bles barely touch and are marginally stretched in the vertical direction.

We have checked whether the measurements of ϕ and Z are consistent by comparing these to prior theoretical predictions of the scaling behavior of Z with ϕ. Simulations of frictionless two-dimensional systems [6, 23] show that Z tends to $Z_c = 4$ if ϕ approaches $\phi_c = 0.842$ at the jamming point J. Away from this critical point these authors find:

$$Z - Z_c = Z_0 \left(\phi - \phi_c \right)^{1/2}. \tag{4.1}$$

This implies that if we know Z we can infer the packing fraction ϕ. We can also directly obtain a value of Z_0 since for very compressed foams ($\phi \to 1, \Delta\phi \equiv \phi - \phi_c \to 0.158$), Z approaches 6. This gives us $Z_0 = 5.06$. Note that in the numerical simulations of O'Hern et al. $Z_0 = 3$ [6].

We extract both ϕ and Z from the following experimental runs. We shear a bidisperse monolayer of foam in the linear geometry from chapter 2 at a fixed driving velocity $v_0 = 0.26$ mm/s. We perform a scan in ϕ for a gap width W of 5 cm and a scan in ϕ for a gap width of 7 cm. We obtain 3000 images per packing fraction, and to obtain statistically independent packings, we only analyze every 100th image, thus averaging both ϕ and z over 30 images, each containing approximately 500 bubbles.

The result is plotted in Fig. 4.5: for both widths the data points follow the same trend and if we overplot the numerical prediction from Eq. (4.1)
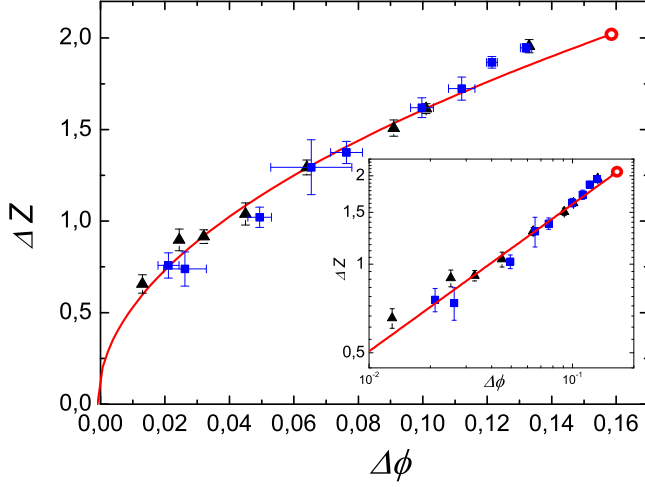
FIGURE 4.5: $Z - Z_c$ as a function of $\phi - \phi_c$, both averaged over 60 frames for a 5 cm gap (triangles) and a 7 cm gap (squares). Solid red line: $Z - Z_c = Z_0(\phi - \phi_c)^{0.5}$ with $Z_0 = 5.06$. Inset shows same plot on log-log scale. Open circle shows value used to calculate Z_0.

with $\phi_c = 0.842$ and $Z_0 = 5.06$ we obtain a reasonable match with the experimental datapoints. Note that we are not the first to have performed such an analysis. In fact Majmudar et al. [94] found the same scaling to hold in a frictional granular but their comparison to frictionless disc simulations seems inappropriate, whereas in our case the comparison is entirely valid. Moreover, the value of Z_0 the authors find in order to fit the data is anomalously high.

4.2 Scaling of the effective viscosity with ϕ

4.2.1 ϕ-dependence of β

Now that we can obtain good estimates of the packing fraction ϕ, we are in a position to investigate the variation of the flow behavior with ϕ, and in particular the functional dependence of the proportionality constant k on ϕ. In chapter 2 our drag force balance model yielded a k that sets the relative influence of the bubble-wall drag with respect to the bubble-
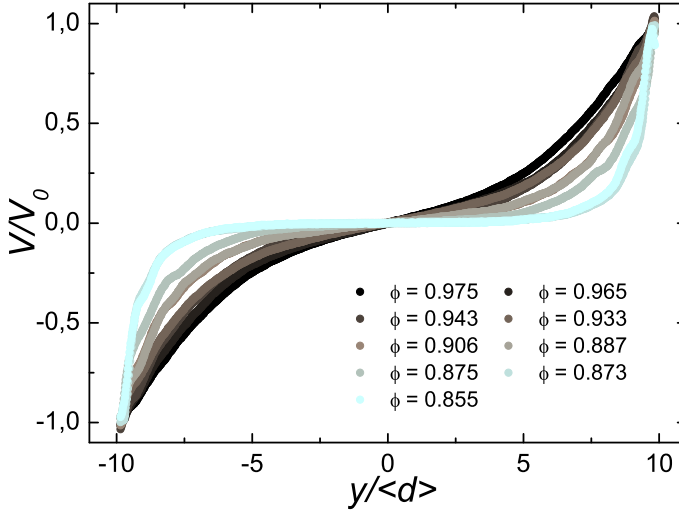
FIGURE 4.6: Velocity profiles from runs performed at a gap width $W = 5$ cm. For all runs, $v_0 = 0.26$ mm/s. Note that some profiles overlap and are thus hidden from view. The closer the density approaches the jamming point, the more shearbanded the velocity profiles become.

bubble drag and is given by $k \propto r_c/\kappa_c$ with r_c the radius of the flattened contact between the bubble and the wall and κ_c the radius of the flattened contact between neighbouring bubbles. Note that actual relation might well read $k \propto r_c^n/\kappa_c^m$, with n, m power law indices, but in principe the functional dependence of k on the two radii should assume a similar ratio.

While r_c is set by the buoyancy and hence does not vary strongly with the gap distance between glass plate and liquid surface — only becoming slightly smaller as the bubbles get stretched at large gaps — κ_c is strongly dependent on the gap size and hence on the packing fraction of the foam. We thus speculate that k will decrease with increasing ϕ as the size of the deformed facets between bubbles increases.

In order to extract k as a function of ϕ we extract averaged velocity profiles from runs at different wetness and fixed driving velocity. In Fig. 4.6 we plot velocity profiles obtained for a gap width $W = 5$ cm at a driving velocity $v_0 = 0.26$ mm/s and $0.855 \leq \phi \leq 0.975$. As ϕ is lowered, the profiles become more and more shearbanded, as expected.
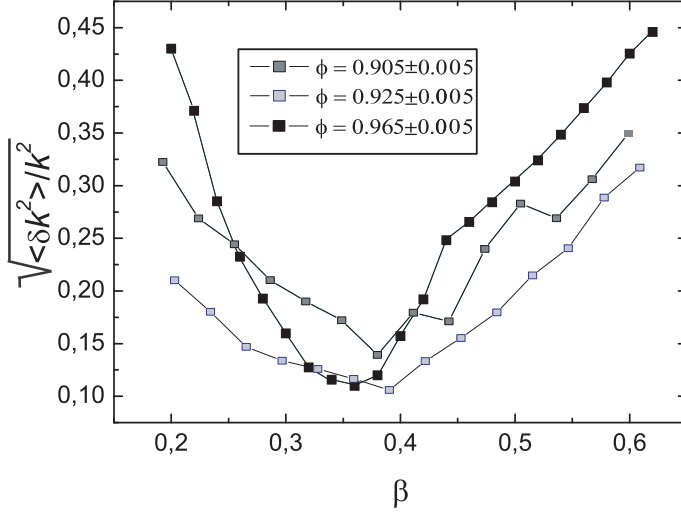
FIGURE 4.7: (a) variance in k values for all six runs performed at $\phi = 0.905$ (grey squares) and $\phi = 0.925$ (light grey squares). The variance at $\phi = 0.965$ (black squares) is data from Fig. 2.9(f). A clear minimum can be observed around $\beta = 0.38$.

We would like to fit solutions of the linear drag force balance model defined in Eq. (2.8) while keeping α and β fixed. The microscopic exponent α which governs the flow a bubble past a wall appears to be independent of the particularities of the foam flow (see section 2.4 and [95, 96]). On the other hand, it is not at all obvious that β, which governs the averaged bubble-bubble drag forces, does not depend on ϕ. As we have seen in chapter 2, β is set by the disorder in the system and the non-affine bubble motion that occurs in conjunction with that. Simulations [80] have shown that this non-affine behaviour strongly depends on ϕ, and therefore the averaged viscous drag could scale differently between different liquid fractions.

To see if this indeed occurs we perform a scan over the same six shear rates as employed in chapter 2 for a bidisperse foam at a gap width $W = 7$ cm, while first fixing $\phi = 0.905 \pm 0.005$ and then $\phi = 0.925 \pm 0.005$. We look for a minimum of the variance in k over the six velocity profiles as a function of β (see green and blue squares in Fig. 4.7). We subsequently fix this β and observe that the model fits best to all six runs performed at

91

$\phi = 0.905$ for $\alpha = 2/3, \beta = 0.38 \pm 0.05$ (see Fig. 4.7) and $k = 7.5$, whereas the model best matches the runs performed at $\phi = 0.925$ for $\alpha = 2/3, \beta = 0.39 \pm 0.05$ (see Fig. 4.7) and $k = 5.8$, thus strongly indicating that within our range of accessible liquid fractions β seems to be a constant while k varies. For comparison, we include the variance for the runs described in chapter 2, that were plotted in Fig. 2.9(f).
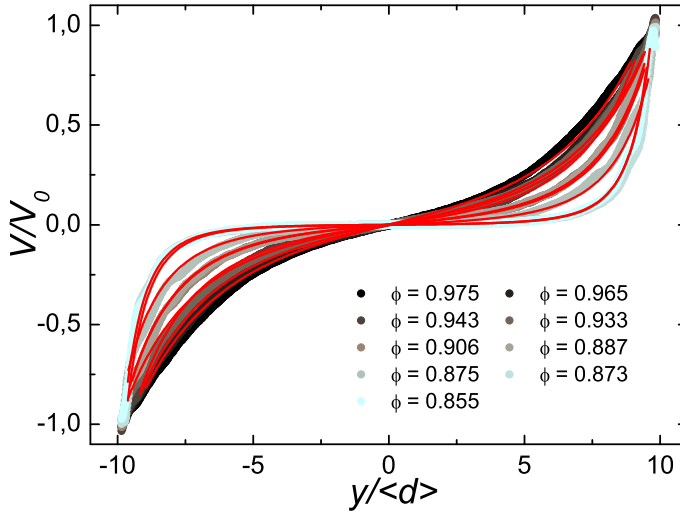

FIGURE 4.8: Velocity profiles from Fig. 4.6. Fits are solutions to linear drag force balance model with $\alpha = 0.67$ and $\beta = 0.36$ fixed. k is extracted from the fits and plotted in Fig. 4.9 as a function of $\phi - \phi_c$.

4.2.2 Scaling of k with ϕ

We measure velocity profiles at gap widths $W = 5$ cm, see Fig. 4.6, and $W = 7$ cm and fixed $v_0 = 0.26$ mm/s (the 3rd slowest driving velocity), for liquid fractions varying between $\phi = 0.855$ and $\phi = 0.975$. To these profiles we fit solutions of our drag force balance model with $\alpha = 0.67$ and $\beta = 0.36$ fixed while varying k, see Fig. 4.8. The best fit yields k and we plot it as a function of $\phi - \phi_c$, with ϕ_c the theoretically predicted and experimentally measured value of the unjamming packing fraction: $\phi_c = 0.842$ [33, 93, 97]. The result can be seen in Fig. 4.9.
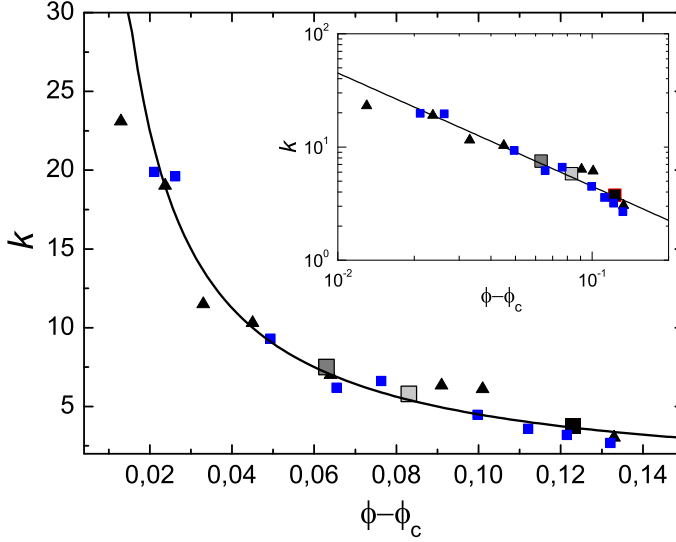
FIGURE 4.9: (b) Scaling of k with $\Delta\phi \equiv \phi - \phi_c$. Triangles: data obtained from fits depicted in Fig. 4.8 where $W = 5$ cm. Squares: data for gap of 7 cm. Large squares correspond to runs at $v_0 = 0.26$ mm/s from Fig. 4.7. Solid line: $0.45/\Delta\phi$. Inset: same data on log-log scale.

The large squares represent the k-value extracted from the strain rate sweeps detailed in Fig. 4.7. The blue squares represent k-values found by fitting the model to the runs performed at a gap of 7 cm, whereas the black triangles are from the 5 cm gap run. We remind the reader that these runs have also provided the $\Delta Z(\Delta\phi)$-scaling in Fig. 4.5 where the color coding is the same.

In Fig. 4.8 we observe increasingly shearbanded velocity profiles as we approach ϕ_c. This trend is reflected in the increase of k as we approach ϕ_c. This implies that the deformed contact radius κ_c between bubbles becomes smaller and smaller. Note that this trend is opposite to what was observed by Debrégeas et al. in [9]: there the authors find that the velocity profiles become less shearbanded with increasing liquid fraction (see inset of Fig. 2.2). We cannot explain this result and conclude it to be one of the many mysteries surrounding that work.

As a guide to the eye we have plotted $k \propto \Delta\phi^{-1}$, and we will now try to relate the measured scaling of k with a simple argument for which we

need to include a prediction from recent work by Denkov et al. [25].

In chapter 1 we have discussed the relation between the dimensionless overlap $\delta\xi$ and the deformed contact κ_c. From Eq. (1.16) we recall that the size of κ_c should depend on the deformation $\delta\xi$ as:

$$\kappa_c \propto (\delta\xi)^{1/2}. \tag{4.2}$$

Furthermore, in simulations of two-dimensional frictionless discs [6, 80] it was found that

$$\delta\xi \propto \Delta\phi. \tag{4.3}$$

Assuming that r_c does not vary much with ϕ, simple substitution thus gives us

$$k \propto 1/(\Delta\phi)^{1/2}. \tag{4.4}$$

The scaling we measure does not agree with this simple prediction. The inset of Fig. 4.9 clearly shows the scaling of k with $\phi - \phi_c$ is steeper than expected from the simple calculation presented above. However, the assumption that the bubble-bubble drag scales linearly with κ_c has been shown to be false in a recent paper by Denkov an coworkers. In fact, the authors show that the viscous dissipation inside foams scales as κ_c^2 instead. Inserting this in the above equations yields:

$$k \propto 1/(\Delta\phi), \tag{4.5}$$

which is fully consistent with our experimental results.

Note that in the above we have only focussed on the radius of the deformed facets. A proper analysis would include the size of the Plateau border around the contact, which is where the dissipation also occurs [21, 22]. For instance, in [96] the bubble-wall drag force scales as $F^{bw} \propto Ca^{0.64}\phi_l^{-0.26}$ and a proper treatment would entail such analysis, even though the functional dependence on the Plateau border size is always weak. Moreover, the Plateau border size itself does not vary by large amounts in the region of ϕ we measure in. Moreover, in all of these works, the functional dependence of the drag force with ϕ is smooth around ϕ_c and hence will not influence the critical scaling at that point.

4.3 Measures of jamming: Voronoi area distribution, $p(f)$ and shear modulus

In 1998, Liu and Nagel [2] introduced the jamming phase diagram in an attempt to describe jamming in a wide variety of materials that, while having a wildly dissimilar appearance, share similar behaviour under, for instance, an applied force. Foams (shaving foam), pastes (peanut butter), emulsions (mayonnaise) and granulates (sugar) can all carry a finite load like a solid, but will flow like a liquid once enough stress is applied. All of these systems consist of elementary building blocks (grains, droplets, bubbles) that are closely packed and jammed at rest and have to overcome steric hindrance and hence deform elastically before they can flow, giving rise to the combination of solid-like and liquid like behaviour.

The jamming diagram has led to an upsurge of scientific interest and in a short time, much theoretical progress has been made - in particular, simulation studies on soft two-dimensional frictionless discs at zero stress, zero temperature and varying packing density ϕ, close to "Point J" (see Fig. 4.10), have yielded much insight [6, 80, 98]. "Point J" corresponds to a critical packing fraction ϕ_c where systems unjam because the density of particles becomes too low for the system to bear a finite load.

If someone familiar with this recent work on the jamming transition in the (Σ, ϕ)-plane were to glance through this thesis, he or she should have to conclude that disordered two-dimensional foams seem to be the ideal candidate to experimentally probe the proposed behaviour [6,80,93] around the jamming transition in frictionless systems. Foam bubbles obey a Hookean interaction law upon compression, do not exhibit solid friction upon sliding and, if appropriately confined by a glass plate, the packing fraction can be varied over a considerable range.

In order to substantiate this idea we will present some highly exploratory and preliminary data on a few measures that are connected to the jamming framework. We will first apply a particular Voronoi tessellation called the navigation map to our experimental images to extract the distribution of free area per bubble in the spirit of Aste et al. [99]. Then, with help from this navigation map, we extract the distribution of contact forces $p(f)$ in the foam and investigate its scaling with ϕ and we conclude with the first preliminary measurements of the scaling of the static shear modulus G with ϕ.
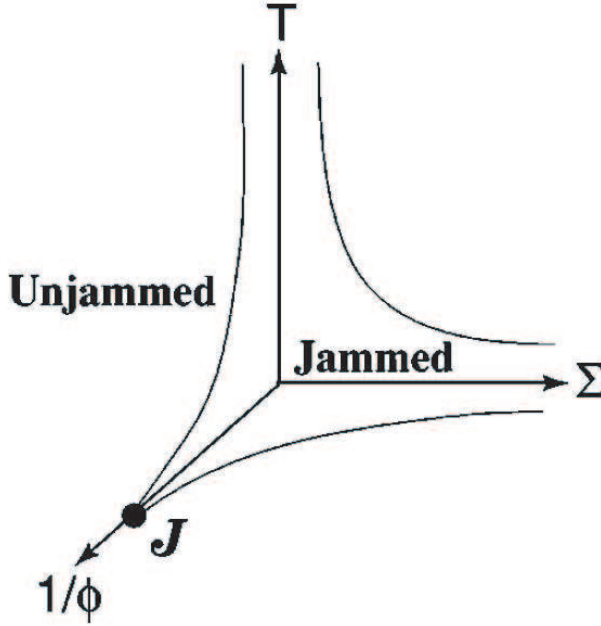
FIGURE 4.10: The jamming phase diagram as proposed in [6]: if the tempera-ture T, the applied stress Σ and the inverse particle density $1/\phi$ are sufficiently small, the system is jammed. Note that all foam experiments are performed in the (Σ, ϕ)-plane.

4.3.1 Voronoi area distribution

Granular thermodynamics

The thermodynamical description of granular materials, as introduced by Edwards and Oakeshott [100] tries to translate the concepts underpin-ning equilibrium thermodynamics to conglomerates of a-thermal particles such as grains. To this end the granular entropy is introduced as

$$S = \ln \Omega(V), \tag{4.6}$$

with $\Omega(V)$ the number of microstates that can be classified under a coarse-grained volume V. Note that it is assumed that all states are equally acces-sible. In this framework, for granular systems the volume thus takes the

role of energy and the global volume V_T of the granular packing is given. The granular temperature β_{gr} is then, as in equilibrium thermodynamics, defined through

$$\beta_{gr} = \frac{\partial S}{\partial V}. \tag{4.7}$$

In thermal systems, $\beta = 1/k_B T$. In granular systems β is related in a similar way to a compactivity χ: $\beta_{gr} = 1/\chi$.

The granular analogue of the Maxwell-Boltzmann distibution that describes the distribution of free volumes V in a $p(V)$ can be found by searching for the functional form of the probability distribution function which maximizes the entropy. Such maximization must be done under the condition that the average occupied volume is equal to $\bar{V}$. This yields:

$$p(V) = \frac{\Omega(V) e^{V/\chi}}{\sum_{V'} \Omega(V') e^{V'/\chi}}. \tag{4.8}$$

Aste and Di Matteo [101] find an analytical expression for $\Omega(V)$ under the assumption that the system consists of elementary cells each weighted according to $p(v) = \frac{1}{\chi} e^{-(v-v_{min})/\chi}$ with the compactivity $\chi = \langle v \rangle - v_{min}$ an intensive thermodynamic parameter accounting for the exchange of volume between the elementary cell and the surrounding volume 'reservoir'. The elementary space partitions that can be measured, such as Delaunay and Voronoi tesselations are assemblies of m such elementary cells, such that $\chi = \frac{\langle V \rangle - V_{min}}{m}$. The aggregate probability distribution function $f(V, m)$ reads:

$$f(V, m) = \frac{m^m}{(m-1)!} \frac{(V - V_{min})^{m-1}}{(\langle V \rangle - V_{min})^m} \exp\left(m \frac{V - V_{min}}{\langle V \rangle - V_{min}}\right). \tag{4.9}$$

This prediction has successfully been compared to free volume distributions that have been experimentally measured in monodisperse packings of frictional spheres in air and in solvent [99]. In these experiments the packing density has been varied been random loose packing (rlp) ($\phi \approx 0.55$) and random close packing (rcp) $\phi \approx 0.64$.

Experiment: Voronoi area distribution

For our two-dimensional foam system we will calculate the free *area* probability distribution $p(A)$. This procedure has been carried out for bidisperse two dimensional packings of hard discs by Lechenault et. al [102],

and for each species they observe a distribution similar to similar to Eq. (4.9) — here the discs are essentially undeformed and the density lies below random close packing. In contrast, we will investigate free area distributions in bi-disperse foams approaching ϕ_{rcp} ($= 0.842$ in foams) from the high density, jammed side. That is, we will extract $p(A)$ from the set of runs we have discussed before with ϕ varying between 0.855 and 0.975.
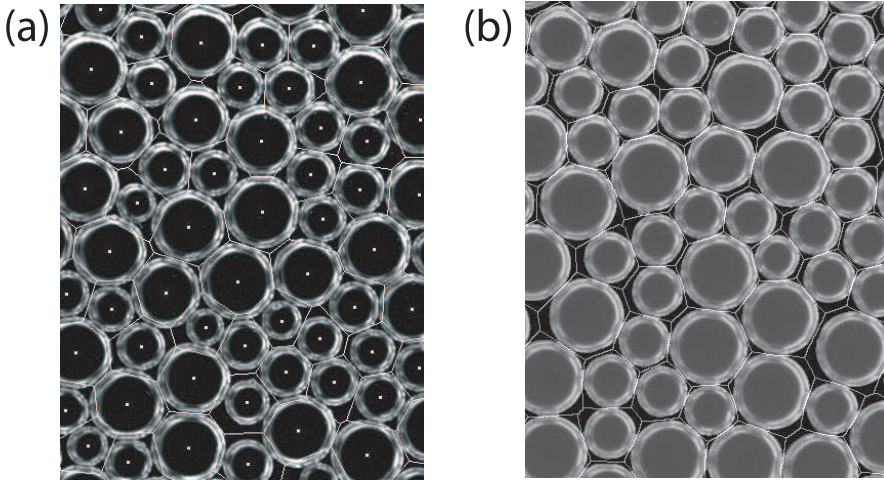

FIGURE 4.11: (a) Standard Voronoi tessellation of the bubble centers: For neighbours that differ in size Voronoi cell perimeters intersect bubbles. (b) The navigation map tessellation respects the bubble edges and follows the curvature of the contacts.

We measure the probability distribution of free areas $p(A)$ by calculating the Voronoi area distribution of the grid of points that represent the centers of mass of the bubbles. For a given grid of points, the Voronoi tessellation yields cells in which all points are closer to a certain grid point than to any other grid point [103]. The Voronoi cell perimeters are thus perpendicular bisections of the vectors connecting a grid point and its nearest neighbours, see Fig. 4.11(a). As a result, for a bidisperse packing, the Voronoi cell edges do in general not respect the bubble perimeter and thus the Voronoi cell does not represent the free area per bubble. For hard spherical objects one can get around this problem by weighting the grid points according to the sphere radius (Voronoi-Laguerre tessellation),

however, in our experiment, the bubbles are not only bidisperse, but in general also deformed and the flattened contacts can be curved.
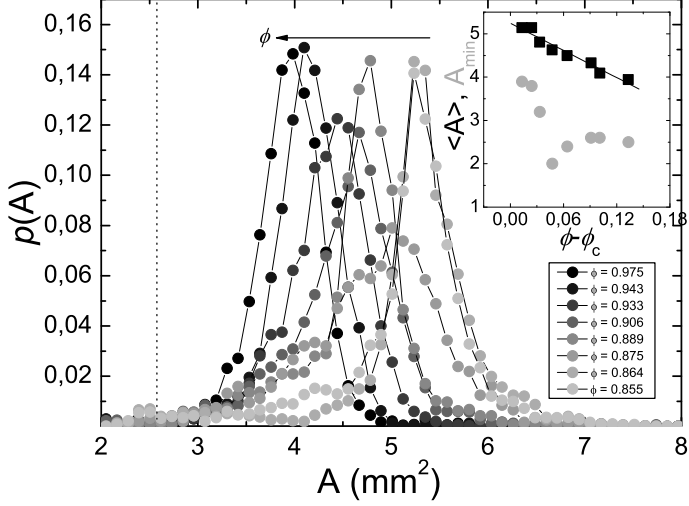

FIGURE 4.12: Distribution of Voronoi area for packings between $\phi = 0.875$ and $\phi = 0.975$. The average Voronoi area $\langle A \rangle$ (black squares) and A_{min} (red dots) are plotted as a function of ϕ in the inset. The vertical dashed line indicates the minimal free Voronoi area for the small bubbles at $\phi = 0.965$ which is given by $A_{min} = \frac{\pi}{4}(1.8)^2/0.965 = 2.63$ mm^2.

To fully take the effects of both deformations and bidispersity into account, we calculate what is called the navigation map [103, 104]. To this end, we take the Delaunay triangulation — which is the dual representation of the Voronoi tesselation — of the grid of bubble centers. Each triangle is divided in 4 areas: three areas each represent the part of a bubble that is inside the triangle and the fourth area corresponds to the interstice. We can illustrate this with a hexagonally ordered, monodisperse foam: in this case the Delaunay triangles connect three bubbles at angles of 60° and the interstice is exactly in the center of the triangle. For all pixels in the interstice we calculate whether they are closest to any point on the perimeter of one of the three bubble areas. The result is shown in Fig. 4.11(b): we obtain free areas per bubble that respect the bubble edges and follow the curvature of the contacts.

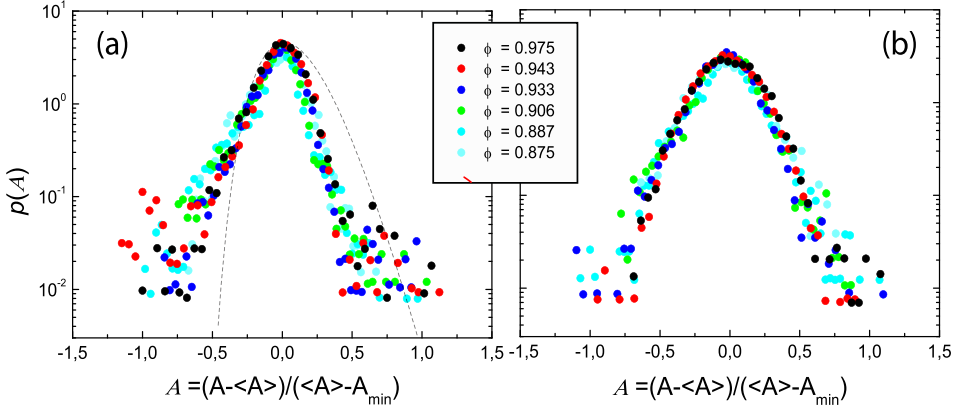We calculate $p(A)$ from the experimental data at a gap width $W = 5$

FIGURE 4.13: (a) Voronoi area distributions for small bubbles at various ϕ (see inset) centered around $\langle V \rangle$ and rescaled by the variance $\langle V \rangle - V_{min}$. Dashed line shows a solution to Eq. (4.9), highlighting the qualitative differences. (b) Voronoi area distributions for large bubbles centered around $\langle V \rangle$ and rescaled by the variance $\langle V \rangle - V_{min}$.

cm that also yielded ϕ and Z as well as the velocity profiles that were used to establish the scaling of k vs ϕ. We state the details: we have performed a scan over ϕ at fixed driving velocity $v_0 = 0.26$ mm/s. We have obtained 3000 images per packing fraction, and we calculate $p(A)$ over a central region of every 100th frame. We subsequently average the individual $p(A)$ distributions to improve statistics. We have measured $p(A)$ for $0.855 \leq \phi \leq 0.975$. We obtain bimodal distributions, which we can split according to the size of the bubbles inside the Voronoi areas. Distributions for the smaller bubbles are shown in Fig. 4.12: for increasing ϕ the average of the distribution shifts to smaller values (see black squares in inset of Fig. 4.12). From these distributions we can also extract A_{min} (red circles in inset of Fig. 4.12). We check that the value of A_{min} that we extract makes sense by calculating its value for $\phi = 0.965$ in the following way: from the size histograms presented in Chapter 2, we know that at that packing fraction, the average small bubble diameter equals 1.8 mm. The miminal free area for such a bubble (in a hexagonal packing of same sized bubbles) equals $A_{min} = \frac{\pi}{4}(1.8)^2/0.975 = 2.63$ mm^2, in good agreement with the value extracted at $\Delta\phi = 0.12$ (see inset of Fig. 4.12).
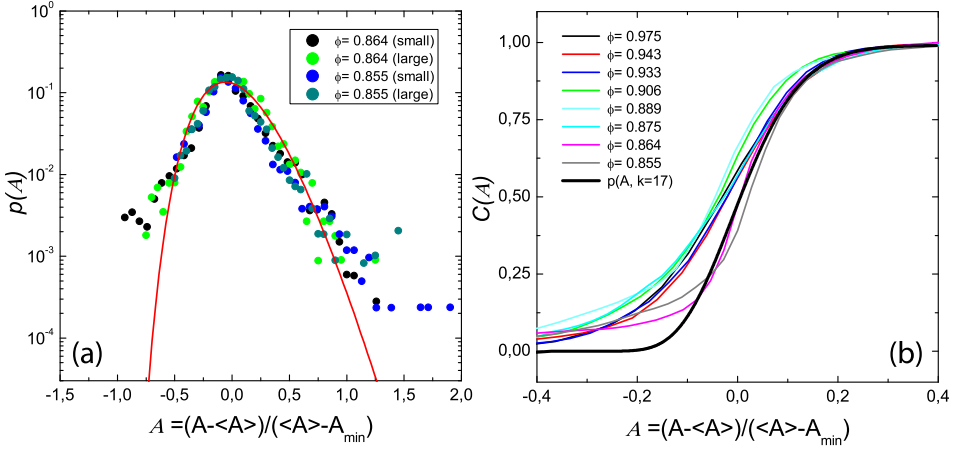
FIGURE 4.14: (a) Voronoi area distributions for small and large bubbles at $\phi = 0.864$ and $\phi = 0.855$ (see inset) centered around $\langle V \rangle$ and rescaled by the variance $\langle V \rangle - V_{min}$. Solid black line is solution to Astes prediction Eq. (4.9) with $m = 17$. (b) The cumulative sum $C(A)$ for all small bubble distributions evidences a sudden crossover to the Aste prediction: for the two lowest ϕ-values, $C(A)$ resembles the predicted $C(A, m = 17)$.

We rescale the distributions by $(A - \langle A \rangle)/(\langle A \rangle - A_{min})$ that is, we center the distributions around the average of the distribution and rescale the width by a free parameter $\langle A \rangle - A_{min}$ which is the variance of the distribution and which can be identified with the granular temperature χ. We plot all rescaled distributions, except those obtained for $\phi = 0.864$ and $\phi = 0.855$ in Fig. 4.13: the left figure (a) shows the collapse of Voronoi area distributions for the small bubbles and the right figure (b) shows the collapse for the large bubbles. Note that the collapse is optimized by variable values of A_{min} which are estimated from the unscaled distributions, see Fig. 4.12. The distribution of the small bubbles appears to be slightly skewed with exponential tails, while the distribution of the large bubbles appears to be symmetrical around $\langle A \rangle$. In this case it is hard to tell whether the tails are exponential or Gaussian. A striking result is thus that the distributions for small and large bubbles do not have the same shape. Furthermore, by comparing the distributions to the Aste prediction $f(V, m)$ were we replace V with A, see dashed line in Fig. 4.13(a)), we

see that both rescaled distributions have a markedly different shape than the analytical prediction.

The Voronoi area distributions of the runs that were performed closest to the jamming transition ($\phi = 0.864$ and $\phi = 0.855$) do not collapse on the master curves presented in Fig. 4.13. We instead plot the distributions for both the large bubbles and the small bubbles together in Fig. 4.14(a). We can observe a reasonable collapse and by overplotting the solution to Eq. (4.9) with $m = 17$ we see that close to ϕ_c the distributions appear to cross over to the shape predicted by this equation.

This is also evidenced in Fig. 4.14(b): here we plot the cumulative distribution $C(A)$ defined as:

$$C(A) \equiv \int_{A_{min}}^{A} p(A')dA'. \tag{4.10}$$

We compare the distibutions $C(A)$ for small bubbles, obtained at various ϕ, to the $C(A, m = 17)$ predicted by Aste et al. [99, 101] that we obtained by fitting to the data in Fig. 4.14(a). We see that the shape of $p(A)$ is the same for all runs except for the runs performed at $\phi = 0.864$ and $\phi = 0.855$. We further see that it quite suddenly crosses over to the shape predicted by Eq. (4.9) for these two runs closest to ϕ_c, indicating that one recovers the Aste prediction close to ϕ_c.

Discussion

We have thus seen that for densely packed two-dimensional foams the Voronoi area distributions $p(A)$ do not comply with the theoretical prediction by Aste et al., but that as one nears the unjamming density ϕ_c, the distributions do seem to cross over to this behaviour. This might be understood by considering the fact that the Aste distribution is well-defined and tested in hard granular materials at densities between ϕ_{rlp} and ϕ_{rcp} and for two-dimensional foams (and frictionless systems in general) $\phi_{rcp} = \phi_J$, such that we approach the region of densities in which Eq. (4.9) applies upon lowering the packing density of the foam.

Note however, that the value $m = 17$ that yields an acceptable agreement between $f(A, m)$ and $p(A)$ is remarkably high, when one interprets this value to be associated with the average number of nearby bubbles that border the free area per bubble, which is 6 for a two-dimensional packing.

4.3.2 The force distribution $p(f)$

In disordered systems the distribution of particle forces is often strongly heterogeneous. In granular systems in particular, forces are typically transmitted along force chains [15,105], which implies that part of the particles bear a very large load while another part hardly participates in transmitting forces. As a result, the distribution of contact forces $p(f)$ in such systems is generally broad, with frequent occurrence of very large interparticle forces.

Both theoretical and experimental investigations ([106] and references therein) generally yield force distributions that exhibit a peak around the average force in the system and a broad tail that is either exponential or Gaussian. In a recent Letter, [106], Tighe and coworkers show that if the proper constraints are taken into account, a Gaussian tail emerges, and it should be noted that the limited statistics available to experimentalists often impede a clear-cut distinction between a Gaussian or an exponential tail. O'Hern et al. [6] also argue that the way one averages over force distributions obtained from distinct packings influences the observed shape of the tail. In the same paper, these authors also identify the appearance of a peak in the force distribution with jamming, implying that for unjammed systems $p(f)$ decreases monotonously.

Extracting $p(f)$ from experimental images

We obtain $p(f)$'s for foams at varying ϕ from the navigation map Voronoi tessellations discussed in the preceding section. Since the tiles in this tessellation respect the bubble edges and follow their curvature, we can overlay the Voronoi cell edges with the images that have yielded ϕ, see Fig. 4.2. In this way we can extract the size of the deformed contacts between touching bubbles i and j which is $2\kappa_c$, as can be seen in Fig. 4.15. This contact size is related to the elastic force f_{ij} through the relation Eq. (1.7):

$$f_{ij} = f_i + f_j = \pi \kappa_c^2 2\sigma \frac{R_i + R_j}{R_i R_j}, \tag{4.11}$$

with κ_c the radius of the deformed contact and $R_{i,j}$ the radii of bubbles i and j respectively. Note that this relation is valid when deformations are small. Whether it breaks down for larger deformation we do not know, but simulations by Lacasse et al. [17] on the interaction law in three-
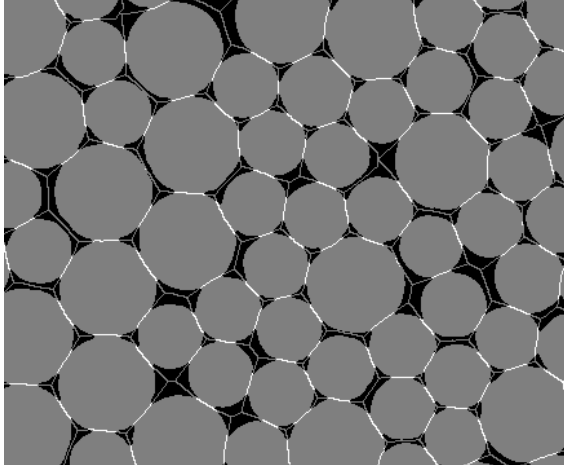
FIGURE 4.15: Illustration of the procedure used to extract $p(f)$: the Voronoi cell boundaries are plotted together with the ϕ plots. Where bubbles overlap, the cell boundaries are bright. The size of this contact is proportional to $\sqrt{f_{ij}}$.

dimensional emulsions provide good hopes that we can assume an interaction like Eq. (4.11) to hold for our two-dimensional foam. Note that since $\kappa_c^2 \propto \xi$ with ξ the overlap, this is the linear harmonic interaction we discussed before.

We use the same experimental images as in the previous section, and hence obtain force distributions at 8 different values of ϕ. For each ϕ we compute $p(f)$ over 30 frames. In Fig. 4.16 we show the normalised distributions for each ϕ. As ϕ decreases towards ϕ_c, we see the peak in $p(f)$ move towards $F = 0$, in accordance with the conjecture that the disappearance of the peak in $p(f)$ signals the jamming transition.

We cannot clearly distinguish the shape of the tails of $p(f)$ over more than two decades, be we do observe a trend in that the distributions seem to exhibit exponential tails near jamming, but become more and more Gaussian the more compressed the system becomes.

Averaging over distinct packings

Note that we have computed the averaged $p(f)$ by simply summing the distributions for each frame. In [98] O'Hern and coworkers argue that
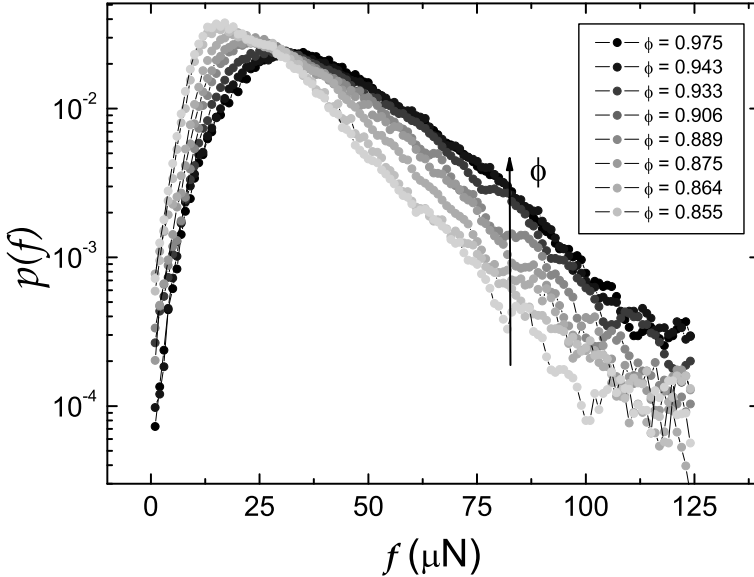
FIGURE 4.16: Force distribution functions obtained by averaging those of 30 different realisations. For decreasing ϕ the peak moves towards $f = 0$ and the shape of the tails appears to cross over from Gaussian to exponential.

the way one calculates the average force distribution from a set of distributions obtained for distinct particle configurations greatly influences the shape of the tails. These authors show that if one simply takes the histogram of all forces from all configurations and then normalises the forces by the force $\langle\langle f \rangle\rangle$ which is the average over all these forces, exponential tails will be seen. Note that this is not the same as the procedure we have followed to calculate the $p(f)$'s in Fig. 4.16. The alternative procedure that is analysed in [98] is to normalise the forces for each packing by their average $\langle f \rangle$ and then perform the summation, in which case one will observe Gaussian tails.

We plot force distributions for different ϕ obtained in the latter way in Fig. 4.17. We do not see a qualitative difference in the trend that the shape of the tails follow between Fig. 4.16 and Fig. 4.17. We do, however, see that the relative contribution of the large forces grows for packings which are closer to ϕ_c in accordance with [6, 16, 98].
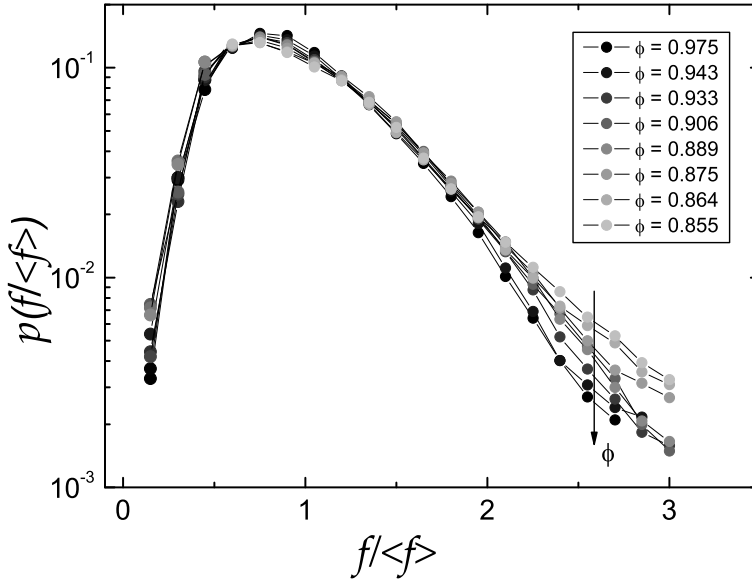
FIGURE 4.17: Force distribution functions obtained by averaging those of 30 different realisations that have each been rescaled by their average force $\langle f \rangle$. For decreasing ϕ the relative contribution of large forces increases and the shape of the tails appears to cross over from Gaussian to exponential.

Discussion

We have performed highly exploratory measurements on the shape of the force distribution $p(f)$ as a function of the distance to jamming. Despite limited statistics, we see globally the same trends as previous authors, e.g., the cross-over from Gaussian to exponential tails and a broadening of the distribution upon approaching ϕ_c. A signature of the precision with which we can measure is to check whether the forces on each bubble are in balance. We find that the error in the force balance per bubble is typically 30% of the sum of all forces on the bubble, which is rather high. This might be due to the fact that slight displacements of the Voronoi cell edges with respect to the bubbles results in a large overestimation of the contact forces due to the circular shape of the bubbles. Also note that the images we analyse are from a sheared foam which means that force balance is not necessarily satisfied. The strong shearbanding in the system, how-

ever, means that the region of interest is hardly flowing, implying that the system is at least close to force balance.

4.3.3 The shear modulus G

The nature of the phase boundaries separating the jammed and the flowing phase is one of the more crucial questions the jamming phase diagram has generated. The simulations [6, 80] have focused on the transition at point "J" (see Fig. 4.10), located at ϕ_c on the density axis, and have evidenced surprising behaviour at this point: the average number of contacts between particles jumps abruptly while the bulk and shear elastic moduli B and G vanish smoothly with critical exponents. Surprisingly, the elastic moduli scale differently: B scales as $(\phi - \phi_c)^{\alpha-2}$, while G scales as $((\phi - \phi_c)^{\alpha-3/2}$, where the exponent α depends on the interaction potential between particles. Irrespective of this interaction potential, the ratio G/K scales as $Z - Z_c$. As a result, jammed systems become much softer to a shear deformation than to a compression, the closer they are to ϕ_c. Furthermore, a length scale ξ related to correlated, vortical motions of the particles, is expected to diverge [6, 80].

In this section, we propose experiments on two-dimensional foams to establish the critical scaling of B and G with $\Delta\phi \equiv \phi - \phi_c$. We will show preliminary data on the shear modulus G to show this techniques' tremendous promise.

We measure the mechanical response of foams at point J in the following way: we trap a monolayer of bubbles in a Taylor-Couette geometry, consisting of two concentric cylinders, see Fig. 4.18(a). We further cover the bubbles with a glass plate, to precisely vary ϕ. The foam is driven by the Anton Paar DSR-301 rheometer which can measure and exert the extremely small stresses and rotations associated with the regime in which foams responds elastically. By using a grooved inner cylinder we shear the foam and hence measure G, see Fig. 4.18(a(i)) while by attaching a different and novel geometry, we will measure the response under compression and hence B, see Fig. 4.18(a(ii)).

The bubbles experience additional viscous drags with the glass plates, but we apply very small step strains (γ= 0.01 %) with the rheometer and only measure the stress after the viscous stresses have relaxed and the resulting signal reflects the elastic response (see Fig. 4.18(b)). One can easily extract the elastic moduli from this signal and by repeating the measure-
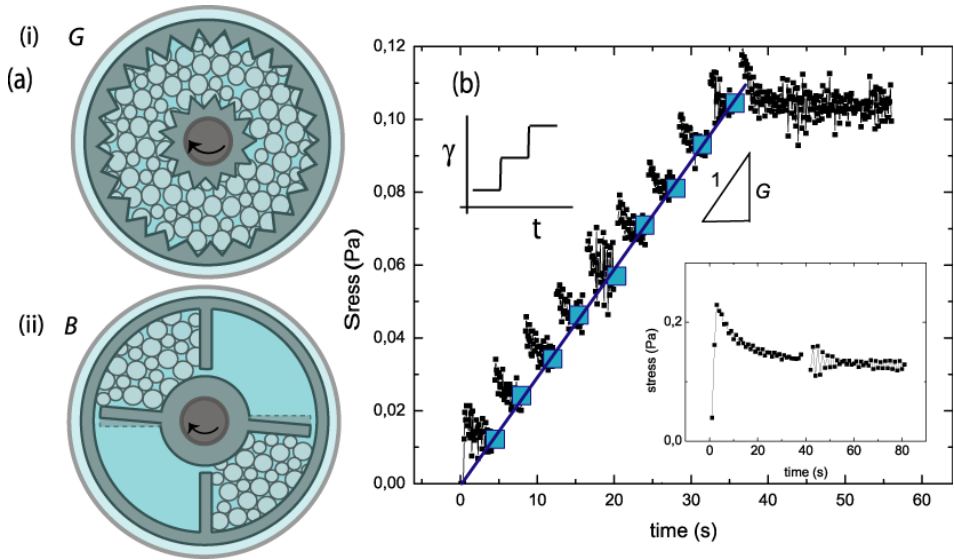
FIGURE 4.18: Schematic picture of the proposed experiments: a monolayer of foam bubbles is loaded in a Couette geometry with top plate and step strains are exerted by the inner cylinder, which is connected to a rheometer head: (i) setup to measure shear modulus G. (ii) setup to measure bulk modulus B. (b) Preliminary measurements of the shear response of a twodimensional foam to step strains: After a viscous transient (see inset), the stress signal reflects only the elastic stress and the slope of the straight line is the shear modulus G.

ments at varying packing fractions and different geometries we can establish the scaling of G and B with ϕ. By looking at the elastic response of the foam to deformations we stay inside the jammed region of the jamming phase diagram at all times and essentially measure along the zero stress, zero temperature axis, see Fig. 4.10.

In Fig. 4.19 we plot the measured stress as a function of time, while applying a small step strain every 4 seconds. We clearly see the viscous transient and the subsequent elastic signal, and while have not been able to exactly measure the density ϕ we have monotonously increased the gap between the fluid and the glass plate and thus we have monotonously increased ϕ. Fig. 4.19 shows the response of the foam at varying ϕ: the shear modulus G increases monotonically with ϕ. Clearly these measurements have to be expanded and performed in a quantitative manner to establish
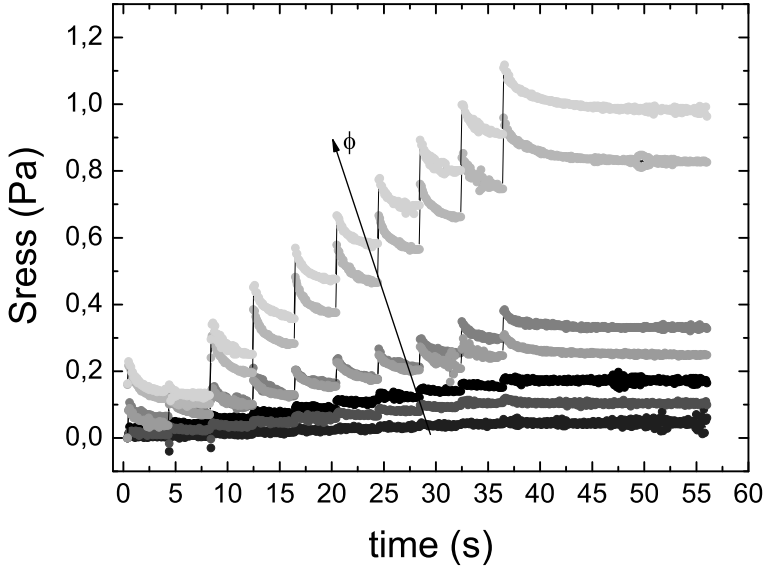
FIGURE 4.19: (a) A monolayer of foam bubbles is loaded in a Couette geometry and step strains are exerted by the inner cylinder, which is connected to a rheometer head, at varying ϕ denoted by arrow. The shear response of a two dimensional foam to step strains becomes increasingly strong and hence G increases when ϕ increases.

critical scaling of the shear modulus G, but nevertheless, these preliminary runs show the huge potential of confined foams to investigate the linear response of soft disc systems near jamming.

4.4 Conclusion

In this chapter, we have discussed a multitude of phenomena that strongly depend on the density ϕ of sheared or static two-dimensional foams. In particular, we have for the first time experimentally established scaling of the inverse foam consistency k and the contact number Z with $\Delta\phi$, and we have observed the predicted shift towards zero of the peak of $p(f)$ as we approached ϕ_c. Also, we have obtained the first indications that G indeed vanishes at point J, even though we cannot establish the scaling yet. In contrast, we have observed peculiar distributions of the Voronoi

area distributions that appeared to be independent of ϕ, except close to the transition, where a sudden crossover towards the prediction for a hard-sphere systems was observed.

Clearly these findings open all sorts of exciting inroads into the behaviour of foams as a function of the bubble density, and many could be put on a firm footing with simply more statistics and a closer approach of ϕ_c.

OUTLOOK

In this final concluding chapter we briefly will set our findings in perspective, focussing on some open issues and outlining emerging avenues for the study of the dynamics of foams as well as other complex, disordered materials. First, we will present a tentative explanation for the observed differences in interbubble drag force exponent β in chapters 2 and 3. Second, we will briefly discuss how major open questions concerning jamming might be answered by experiments on foams, and suggest to explore analogies between granular media and foams.

5.1 Viscous drag, fluctuations an kymographs

In this thesis we have focussed on the averaged stresses and strainrates — even though, clearly, disorder and fluctuations are crucial in setting the values of the averaged stresses. While the drag force between bubbles and the glass plate appears to scale robustly with the bubble velocity raised to a fixed exponent α, and while this behaviour has also been understood theoretically, it is the scaling exponent of the interbubble drag forces that appears to vary from one experimental geometry to the other and which theorists have only recently begun to investigate.

By tracking of bubble positions and velocities in foams it was recently revealed [75] that the globally measured viscous stresses (which are directly related to the interbubble drags) and the fluctuations in the foams are intimately related. Performing such analysis for all different geometries is beyond the scope of this thesis, we therefore aim instead to gain

$\dot{\gamma}$=0.05 $\dot{\gamma}$=0.0162 $\dot{\gamma}$=0.005

Linear with glass plate

Couette with glass plate r_i=0.105

Couette no glass plate r_i=0.105 m
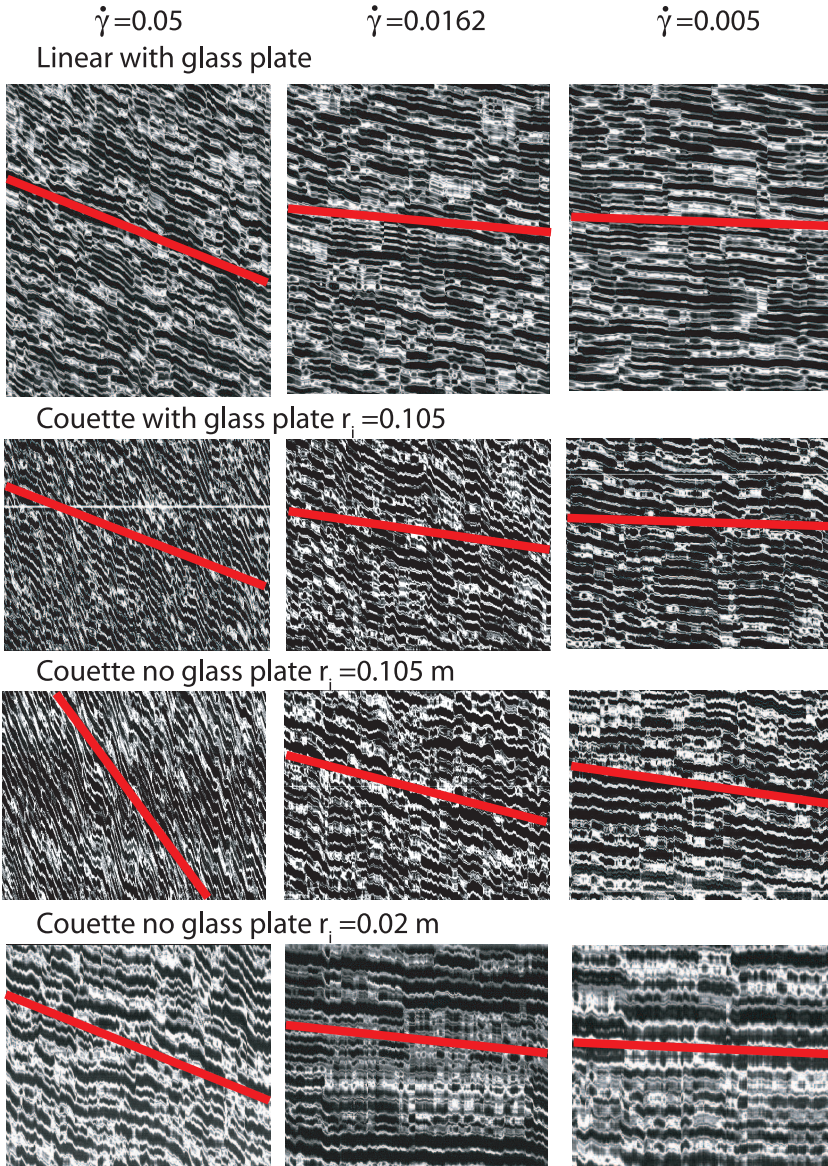
Couette no glass plate r_i=0.02 m

FIGURE 5.1: Kymographs (space-time plots) of the fluctuating foam flow at different local strain rates and in various experimental geometries. Solid lines indicate the average velocities at the corresponding positions in the experiments.

insight in the nature of fluctuations in our various experimental geometries by more simple qualitative methods.

We do this by drawing *kymographs* — which is a fancy word for space-time plots. To this end we select experimental runs where $v_0 \approx 0.8$ mm/s. in the linear geometry with a glass plate, the Couette geometry with and without glass plate (with inner radius $r_i = 10.5$ cm) and the Couette rheometry geometry ($r_i = 2$ cm). We determine where in each geometry the local strain rate $\dot{\gamma}_l$ equals 0.05 s^{-1}, 0.0164 s^{-1} and 0.005 s^{-1} and we draw the space-time plot of the corresponding image lines from 1000 frames.

The kymographs are plotted in Fig. 5.1 and are ordered along the columns by $\dot{\gamma}_l$ and along the rows by from top to bottom: the linear geometry, the Couette geometry with a top plate, the large Couette geometry without a top plate and the small rheometrical Couette geometry without top plate. We observe strong jittery fluctuations for the open geometries, whereas the fluctuations for the bounded geometries seem more smooth and slow, c.f. row 1 and 2 with row 3 and 4.

We thus seem to observe qualitatively different fluctuations depending on whether the foams are confined by a glass plate or not. This difference might give rise to the different scaling of β between the two geometries and a next step would be to quantify this notion by particle tracking.

Note further that the fluctuations in the instantaneous velocities and hence in the local strain rates are really large. The same holds for the average stresses one can measure by rheometry. While relating both highly noisy and strongly averaged quantities has basically been the focus of this thesis, investigating the local dynamics of these foams by bubble tracking will yield additional and deeper understanding of foam rheology.

5.2 Foam as a granular material: jamming and flow

In this section we speculate on possible experiments that can be performed with foam in the context of the jamming phase diagram. Also, we will suggest to translate key granular experiments to those with foams. In the last chapter we have already discussed a variety of experiments with which we have taken first steps towards probing the jamming transition with foam bubbles. We have extracted static measures such as $p(f)$ and $p(A)$ and G, which we can directly compare to theory.

113

Another measure that we could extract from our foam data is a length-scale ξ. There are two definitions, one for static and one for flowing packings. For static packings this lengthscale probes the spatial extension of force fluctuations [107], while for flowing packings it is associated with the spatial extension of correlated motion [97, 108, 109] in other words, with the size of the so-called dynamical heterogeneities. Since we can resolve the force network as well as the fluctuations in bubble motions both measures could in principle be extracted from experimental data, and we will certainly attempt this in the near future.

In two-dimensional foam systems, a further challenge lies in understanding the oscillatory rheology. Could the scaling of the visco-elastic moduli G', G'' for instance be related to the dynamics at the bubble scale? Would one observe the large scale rearrangements associated with shear reversal and shear start-up [72, 110]?

Finally, another promising route is to redo granular experiments, but then with foam bubbles. Recently, gravity-driven flow of bubbles in either silo's [111] and rotating drums [112] has been investigated and results similar to the granular case have been obtained. One experiment that would also be feasible is that of investigating chute flows [113] in three-dimensional bubble systems, to investigate the formation of shearbands, the interface between flowing and stationary regions and the existence of a critical tilt angle. Such experiments could strengthen the ties between two fascinating macroscopic and strictly athermal examples of soft matter.

Summary

Foams are aggregates of air bubbles that are surrounded by a thin layer of liquid. They are intrinsically unstable, but adding a surfactant like dishwashing fluid or soap to the fluid can prolong the lifetime of bubbles up to hours. Individual foam bubbles obey rather simple interaction laws: foam bubbles are elastic, that is, if they are deformed they will bounce back and if a foam bubble is sliding past another object it will feel a drag force. Furthermore, foam bubbles are often macroscopic (between 0.1 mm and 1 cm) meaning that they will not jiggle around at room temperature.

Despite the simplicity of its constituents a foam behaves in a complicated manner. Consider the collection of bubbles which constitute a column of shaving cream, for example. This conglomerate can carry its own weight like a solid and will bounce back when gently poked, while it will flow like a liquid once sufficiently strong forcing is applied. The threshold stress that leads to flow is often referred to as the *yield stress*. Furthermore, the faster one drives the foam, the less the foam will resist the flow, which is called *shear-thinning*. This behaviour is common to a larger class of materials such as sandpiles, emulsions (mayonnaise), pastes (peanut butter) and colloidal systems (toothpaste) which are all disordered packings of many particles.

The big challenge in the field of disordered materials is to relate the properties of the individual particles to the behavior of the material as a whole. In order to do this one needs to simultaneously measure the global behaviour and the motion and state of all the individual particles. However, the white colour of most of the materials mentioned above signals the

fact that these media strongly scatter light, and thus one cannot directly look inside.

In this thesis, we have gained insight in the connection between the local and global behaviour in foams by retreating to two dimensions. In chapter 2, we describe an experiment in which we induce flow in a single disordered layer of foam bubbles bound between the surface of a soapy solution and a glass plate. We obtain the averaged velocity profiles as a function of the applied shear rate and in addition we obtain information on the local flow behaviour by very careful measurements of the relation between forces and deformations in foam with a rheometer. We find that by only considering that the viscous drag forces on the bubbles need to balance — the drag forces result from the bubble sliding past another bubble or sliding past the confining glass plate — we can explain the observed shape of the velocity profiles. From the force balance we can deduce an expression for the average drag force between bubbles which we can compare to direct measurements with the rheometer. Surprisingly, we find that the average local drag force between neighbouring bubbles in a disordered, flowing foam is different from the actual local drag force between two bubbles that move past each other in an orderly fashion, as in the rheometer. We attribute the difference to the erratic flow that occurs in the disordered foam, which on average enhances the amount of drag a bubble experiences during flow. We substantiate this picture further by shearing an ordered, crystalline foam. In that case we see that our drag force balance model fits the date provided the local drag force between bubbles is indeed the same as the one we measured using rheomtry.

In chapter 3 we continue in the same vein, but this time we shear two-dimensional disordered foam layers in a circular geometry called a Couette cell. In this geometry, the foams are contained inside two concentric circles and the inner disc is rotating. In the linear geometry used in chapter 2 the effect of a yield stress in the foam cannot be observed. However, in a Couette geometry its signature should in principle be visible, due to the curvature in this system. Moreover, the Couette geometry allows for runs both with and without the glass top plate, and we have investigated the effect of the glass plate in further detail.

We again record average velocity profiles and by adapting our drag force balance model to the curved coordinates we extract the behaviour of the bubble-bubble drag force by fitting the model to the data. When

116

the foam is not confined by the glass plate, it appears to be a lot more shear thinning than when it is confined. We speculate that the presence of the glass plate alters the fluctuations in a disordered foam, much as the disorder itself did in chapter 2, and we suggest to measure the influence of the glass plate on the fluctuations by particle tracking. In both cases we observe no signature of a yield stress, in fact, if we image the velocity profiles while simultaneously measuring the global force-deformation rate with a rheometer, we find that locally, the foam does not cease to flow while globally the foam appears to be below the yield stress.

In chapter 4 we change gears and explore the applicability of foams to experimentally probe the nature of the jamming transition. The jamming framework was introduced to unify different classes of disordered materials that exhibit a transition between fluid-like and solid-like behaviour which is termed the jamming transition. Foams can be made to lose their solid-like behaviour by applying a stress larger than the yield stress or by lowering the packing density of foam bubbles. In order to vary this packing fraction, we vary the gap between glass plate and liquid surface (this gap was constant in chapters 2 and 3). In chapter 4 we thus explore the jamming transition as a function of density.

We first describe techniques we have developed to characterise the bubble density in our experimental geometry and then investigate the foam viscosity as a function of the distance to the transition. Finally, we explore mechanical and statistical measures that probe the physical nature of the jamming transition and we find promising indications that foams are indeed eminently suited to probe the jamming framework.

SUMMARY

Samenvatting

Schuim is een agglomeraat van luchtbellen die omringd zijn door een dun laagje vloeistof. Deze bellen zijn van nature instabiel, maar het toevoegen van een oppervlakte-actieve stof zoals afwasmiddel of zeep aan de vloeistof kan de levensduur van bellen verlengen tot uren. Individuele schuimbellen houden zich aan redelijk eenvoudige interactiewetten; zo zijn schuimbellen elastisch, dat wil zeggen als ze vervormd worden zullen ze willen terugveren teneinde hun evenwichtsvorm te hervinden, en als schuimbellen langs een ander object glijden zullen ze een wrijvingskracht ervaren. Verder zijn schuimbellen over het algemeen macroscopisch (0.1 - 10 mm) en dus zullen ze bij kamertemperatuur geen thermische beweging laten zien.

Ondanks het eenvoudige gedrag van zijn bouwstenen vertoont een schuim complex gedrag: Beschouw bijvoorbeeld de collectie van bellen die een klodder scheerschuim is. Dit conglomeraat kan zijn eigen gewicht dragen en zal terugveren als je er met een vinger tegenaan duwt, terwijl het zal stromen als een vloeistof wanneer voldoende kracht wordt uitgeoefend. De kritieke spanning die tot stroming leidt wordt vaak de *yield stress* (=lett. bezwijkspanning) genoemd. Verder is het zo, dat des te sneller je een schuim aandrijft, des te minder weerstand tegen stroming het schuim zal uitoefenen, wat ook wel *shear-thinning* gedrag genoemd wordt. Dit gedrag komt algemeen voor in een ruime klasse van materialen zoals zandhopen, emulsies (mayonaise), pasta's (pindakaas) en colloïdale systemen (tandpasta) die allemaal bestaan uit wanordelijke pakkingen van vele deeltjes.

De grote uitdaging in het veld van de wanordelijke materialen waartoe schuim behoort is om de eigenschappen van de individuele deeltjes te relateren aan het gedrag van het materiaal als geheel. Teneinde dit te kunnen doen zou je tegelijk het globale gedrag en de beweging en toestand van alle individuele deeltjes moeten meten. Echter, de witte kleur van de meeste van deze materialen geeft al aan dat deze media licht sterk verstrooien, en dus kan je niet zomaar binnenin kijken.

In dit proefschrift hebben we ons inzicht aangaande de connectie tussen lokaal en globaal gedrag in schuim vergroot door ons te beperken tot twee dimensies. In hoofdstuk 2 beschrijven we een experiment waarin we een lineaire afschuifstroming (*shear flow*) veroorzaken in een enkele laag schuimbellen die opgesloten zit tussen de oppervlakte van een vloeistof die bestaat uit een oplossing van afwasmiddel in water en een glasplaat. We meten gemiddelde snelheidsprofielen als functie van de uitgeoefende afschuifsnelheid (de *shear rate*) en daarbovenop verkrijgen we informatie over het lokale stromingsgedrag uit heel gevoelige metingen van de relatie tussen spanning (*stress*) en deformatie (*strain*) met een reometer. We ontdekken dat we de waargenomen vorm van de snelheidsprofielen kunnen verklaren door alleen maar aan te nemen dat de visceuze wrijvingskrachten die de bellen voelen, moeten balanceren. Deze wrijvingskrachten zijn het gevolg van het glijden van de bellen ten opzichte van de glasplaat en ten opzichte van andere bellen. Uit de krachtenbalans die we opstellen kunnen we een uitdrukking voor de de gemiddelde wrijvingskracht tussen schuivende bellen afleiden die we kunnen vergelijken met directe metingen die we hebben gedaan met de reometer.

Verassend genoeg vinden we dat de gemiddelde lokale wrijvingskracht tussen naburige bellen in een wanordelijk, stromend schuim verschilt van de werkelijke lokale wrijvingskracht tussen bellen die op een nette, ordelijke manier langs elkaar heen bewegen en die we kunnen meten met de reometer.

We schrijven het verschil tussen de twee toe aan de wanordelijke stroming die optreedt in het wanordelijke schuim en die de gemiddelde hoeveelheid wrijving op een schuimbel tijdens stroming doet toenemen. We kunnen deze interpretatie versterken door een schuifstroming op een geordend schuim uit te oefenen, en in dat geval leiden we uit onze wrijvingskrachtenbalans af dat de lokale wrijving tussen bellen in het experiment inderdaad dezelfde is als die in de reometer.

120

In hoofdstuk 3 gaan we voort op de ingeslagen weg, maar ditmaal brengen we een afschuiving aan op wanordelijke, tweedimensionale bellenlagen in een circulaire geometrie, genaamd de Couette cel. In deze geometrie bevindt het schuim zich tussen twee concentrische cylinders, waarvan de binnenste ronddraait. Deze geometrie maakt het mogelijk experimenten te doen waarbij het schuim wel of niet bedekt is met een glasplaat zodat we het effect van de wrijvingskracht uitgeoefend door de glasplaat verder kunnen onderzoeken. Verder zouden we de effecten van de *yield stress*, die in de lineaire geometrie onzichtbaar waren in deze cylindrische opstelling moeten kunnen zien.

We meten wederom gemiddelde snelheidsprofielen en door ons wrijvingskrachtmodel aan te passen aan het gekromde coördinatenstelsel kunnen we weer het gedrag van de wrijvingskracht tussen bellen afleiden. We vinden dat het schuim zich veel meer *shearthinning* gedraagt als het niet is afgesloten met de glasplaat dan wanneer het dat wel is, en we speculeren dat de aanwezigheid van de glasplaat de fluctuaties in het schuim verandert, op dezelfde manier als de wanorde dat deed in hoofdstuk 2. Verrassend genoeg zien we in beide configuraties geen effecten van een *yieldstress*. Het is zelfs zo dat we, door tegelijkertijd snelheidsprofielen en de globale *stress-strain*-relatie te meten, vinden dat het schuim lokaal nog steeds stroomt wanneer het globaal gezien beneden de *yield stress* zou moeten zijn.

In hoofdstuk 4 verleggen we de aandacht en richten we ons op de toepasbaarheid van schuimsystemen in het onderzoeken van de fysische aard van de *jamming*-overgang. Het *jamming*-fasediagram is recent geïntroduceerd met als doel het gedrag van verschillende klassen van materialen die een overgang tussen vast en vloeibaar gedrag laten zien, onder één noemer te vangen. We hebben al gezien dat schuim zijn elastische gedrag kan verliezen door een spanning groter dan de *yield stress* uit te oefenen. Een alternatieve route is echter het verlagen van de dichtheid van de schuimbellen. We kunnen deze dichtheid variëren door de afstand tussen het vloeistofoppervlak en de glasplaat — die in hoofdstuk 2 en 3 constant was — te vergroten of te verkleinen. Op deze manier kunnen we dus de *jamming*-overgang als functie van de dichtheid verkennen in schuim.

We beschrijven eerst technieken die we ontwikkeld hebben om de bellendichtheid in ons experiment te karakteriseren, waarna we de viscositeit

van het schuim als functie van de afstand tot de *jamming*-overgang on-derzoeken. Tenslotte verkennen we mechanische en statistische maten die inzicht verschaffen in het fysische wezen van de *jamming*-overgang. We vinden veelbelovende aanwijzingen dat schuim inderdaad uitstekend geschikt is om het deze overgang te gaan begrijpen.

Publication List

[1]   Gijs Katgert, Matthias. E. Möbius and Martin van Hecke,
       Rate Dependence and Role of Disorder in Linearly Sheared Two-Dimensional Foams,
       Phys. Rev. Lett **100**, 058301 (2008).
[2]   Matthias. E. Möbius, Gijs Katgert and Martin van Hecke,
       Relaxation and Flow in Linearly Sheared two-dimensional Foams,
       submitted to Phys. Rev. Lett. (2008).

Curriculum Vitae

Ik ben geboren op 25 juni 1981 te Leiden. Mijn jeugd bracht ik door in diezelfde stad en ook bezocht ik daar het Dr. W.A. Visser 't Hooftlyceum, waar ik in 1999 mijn VWO-diploma behaalde. Ik ging vervolgens natuurkunde studeren aan de Universiteit Utrecht. Ik studeerde in 2004 af in de experimentele natuurkunde onder begeleiding van Prof. Dr. P. van der Straten. Het onderwerp van mijn scriptie was de laserfrequentie stabilisatie in een Bose-Einstein-Condensatie experiment. In januari 2005 trad ik in dienst bij de Stichting voor Fundamenteel Onderzoek der Materie (FOM), als onderzoeker in opleiding aan de Universiteit Leiden. Onder begeleiding van Prof. dr. M.L. van Hecke onderzocht ik de stroming alsook de statische eigenschappen van twee-dimensionaal schuim. De resultaten van dit onderzoek zijn verzameld in dit proefschrift. Gedurende mijn promotie-onderzoek heb ik een winterschool bezocht in Les Houches (Frankrijk) en korte scholen in Utrecht en Enschede. Ik heb verder conferenties bezocht in Noordwijk, Amsterdam, Lunteren, Veldhoven, Potsdam (Duitsland), Napels (Italie), Tampa en New Orleans (Verenigde Staten). en ik heb voordrachten over mijn werk gegeven in Noordwijk, Amsterdam, Veldhoven, Saclay, Sofia, Tampa en New Orleans. Tenslotte heb ik in Leiden geassisteerd by het practicum "Signaalverwerking en Ruis".

Dankwoord

Bibliography

[1] D. Weaire and S. Hutzler, *The Physics of Foams* (Clarendon Press, Oxford, 1999).

[2] A.J. Liu and S.R. Nagel, Nature **396**, 21 (1998).

[3] P.A. Kralchevsky and K. Nagayama, *Particles at Fluid Interfaces and Membranes*, *1st edition* (Elsevier, Amsterdam, 2001).

[4] S.A. Koehler, S. Hilgenfeldt and H.A. Stone, Phys. Rev. Lett. **82**, 4232 (1999).

[5] G. Verbist, D. Weaire and A.M. Kraynik, J. Phys. Cond. Matt. **8**, 3715 (1996).

[6] C.S. O'Hern, L.E. Silbert, A.J. Liu and S.R. Nagel, Phys. Rev. E **68**, 011306 (2003). *ibid.* Phys. Rev. Lett. **88**, (2002).

[7] A. Saint-Jalmes and D.J. Durian, J. Rheology **43**, 1411 (1999).

[8] J. Lauridsen, M. Twardos, and M. Dennin, Phys. Rev. Lett. **89**, 098303 (2002).

[9] G. Debrégeas, H. Tabuteau and J.-M. di Meglio, Phys. Rev. Lett. **87**, 178305 (2001).

[10] E. Janiaud, D. Weaire and S. Hutzler, Phys. Rev. Lett. **97**, 038302 (2006).

[11] S.J. Cox, Coll. Surf. A **263**, 81 (2005).

[12] B. Dollet, F. Elias, C. Quilliet, C. Raufaste, M. Aubouy and F. Graner, Phys. Rev. E, **71**, 031403 (2005).

[13] J.N. Israelachvili and R.M. Pashley, Nature **300**, 341 (1982).

[14] P. Somasundaran, S. Simpson, R.K. Jain, I.B. Ivanov, V. Raghuraman, J. Colloid Interface Sci., **225**, 243 (2000).

[15] S. Zhou, Q. Long, D. Wang and A.D. Dinsmore, Science 312, 1631 (2006).

[16] J. Brujić, S.F. Edwards, I. Hopkinson, and H. A. Makse, Physica A. **327**, 201 (2003).

[17] M.-D. Lacasse, G.S. Grest, D. Levine, T.G. Mason and D.A. Weitz, Phys. Rev. Lett., **76**, 3448 (1996).

[18] P. Aussillous and D. Quéré, Europhys. Lett. **59**, 370 (2002).

[19] F.P. Bretherton, J. Fluid Mech. **10**, 166 (1961).

[20] N.D. Denkov, V. Subraminian, D. Gurovich and A. Lips, Coll. Surf. A **263**, 129 (2005).

[21] N.D. Denkov, S. Tcholakova, K. Golemanov, V. Subramanian, and A. Lips Coll. Surf. A **282-283**, 329 (2006).

[22] E. Terriac, J. Etrillard and I. Cantat, Europhys. Lett. **74**, 909 (2006).

[23] D. Durian, Phys. Rev. Lett. **75**, 4780 (1995).

[24] D.A. Reinelt and A.M. Kraynik, J. Coll. Interf. Sci. **132**, 491, (1989).

[25] N.D. Denkov, S. Tcholakova, K. Golemanov, K.P. Ananthapadmanabhan, and A. Lips, Phys. Rev. Lett. **100**, 138301 (2008); S. Tcholakova, N.D. Denkov, K. Golemanov, K.P. Ananthapadmanabhan, and A. Lips, Phys. Rev. E **78**, 011405 (2008).

[26] M.M. Nicholson, Proc. Cambridge Philos. Soc. **45**, 288 (1949).

[27] D.Y.N. Chan, J.D. Henry Jr. and L.R. White, J. Coll. Interf. Sci. **79**, 410 (1981).

[28] N.D. Vassileva, D. van den Ende, F. Mugele and J. Mellema, Langmuir **21**, 11190 (2005).

[29] P.A. Kralchevsky, I.B. Ivanov and A.D. Nikolov, J. Coll. Interf. Sci. **112**, 108 (1986).

[30] V.N. Paunov, P.A. Kralchevsky, N.D. Denkov and K. Nagayama, J. Coll. Interf. Sci. **157**, 100 (1993).

[31] L. Bragg and J.F. Nye, Proc. R. Soc. Lond. A **190**, 474 (1947).

[32] H.M. Princen, J. Colloid Interface Sci. **91**, 160 (1983).

[33] F. Bolton and D. Weaire, Phys. Rev. Lett **65**, 3449 (1990).

[34] A. van der Net, W. Drenckhan, D. Weaire and S. Hutzler, Soft Matter **2**, 129-134, (2006).

[35] S.A. Khan, C.A. Schnepper and R.C. Armstrong, J. Rheology **32** 69 (1988).

[36] E. Pratt and M. Dennin, Phys. Rev. E **67**, 089303 (2003).

[37] R. Höhler and S. Cohen-Addad, J. Phys. Cond. Matt. **17**, 1041 (2005).

[38] A.D. Gopal and D.J. Durian, Phys. Rev. Lett. **91**, 188303 (2003).

[39] F.Bolton and D. Weaire, Phil. Mag. B **63** , 795 (1991).

[40] P. Marmottant, F. Graner, Eur. Phys. J. E. **23**, 337 (2007).

[41] R. Höhler, S. Cohen-Addad and V. Labiausse, arXiv:cond-mat/0610279.

[42] P. Saramito, J. Non-Newt. Fl. Mech. **145**, 1 (2007).

[43] S.Bénito , C.-H. Bruneau , T. Colin , C. Gay and F. Molino, Eur. Phys. J. E, **25** 225 (2008).

[44] H.A. Barnes, J.F. Hutton and K. Walters, *An Introduction to Rheology*, Elsevier Science, Amsterdam (1989).

[45] W.H. Herschel and R. Bulkley, Koll. Zeitschrift **39**, 291 (1926).

[46] T.G. Mason, J. Bibette and D.A. Weitz, J. Coll. Interf. Sci. **179**, 439 (1996).

[47] L. Bécu, S. Manneville and A. Collin, Phys. Rev. Lett. **96**, 108203, (2006).

[48] H.M. Princen, J. Colloid Interface Sci. **105**, 150 (1985).

[49] H.M. Princen and A.D. Kiss, J. Colloid Interface Sci. **112**, 427 (1986).

[50] H.M. Princen and A.D. Kiss, J. Colloid Interface Sci. **128**, 176 (1989).

[51] T.G. Mason, J. Bibette and D.A. Weitz, Phys. Rev. Lett. **75**, (1995).

[52] D.J. Durian, D.A Weitz and D.J. Pine, Science **252**, 686 (1991).

[53] J. Lambert, I. Cantat, R. Delannay, R.Mokso, P.Cloetens, J.A. Glazier and F. Graner, Phys. Rev. Lett. **99**, 058304 (2007).

[54] K. Brakke, Exp. Math. **1**, 141, (1992).

[55] T. Okuzono and K. Kawasaki, Phys. Rev. E **51**, 1246 (1995).

[56] N. Kern, D. Weaire, A. Martin, S. Hutzler and S.J. Cox, Phys. Rev. E **70**, 041411 (2004).

[57] D.J. Durian Phys. Rev. E **55**, 1739 (1997).

[58] S. Tewari, D. Schiemann, D.J. Durian, C.M. Knobler, S.A. Langer, and A.J. Liu, Phys. Rev. E **60**, 4385 (1999).

[59] J.A. Glazier, M. P. Anderson and G. S. Grest, Phil. Mag. B **62**, 615 (1990).

[60] R.M.C de Almeida, G.L. Thomas and F. Graner, Physica A **371**, 67 (2006).

[61] C. Raufaste, B. Dollet, S. Cox, Y. Jiang and F. Graner, Eur. Phys. J. E **23**, 217 (2007).

[62] A. Kabla and G. Debrégeas, Phys. Rev. Lett. **90**, 258303 (2003).

[63] S. Asakura and F. Oosawa, J. of Poly. Sci. **33**, 183 (1958).

[64] C. Stanley Smith, Scientific American, (1954).

[65] M. Fátima Vaz and M.A. Fortes, J. Phys. Cond. Matt. **9**, 8921 (1997).

[66] Y. Wang, K. Krishan and M. Dennin, Phys. Rev. E **73** 031401 (2006).

[67] E. Janiaud and F. Graner, J. Fluid. Mech. **532**, 243 (2005).

[68] C. Gilbreth, S. Sullivan, and M. Dennin, Phys. Rev. E **74** 031401 (2006).

[69] Y. Wang, K. Krishan and M. Dennin, Phil. Mag. Lett. **87**, 125 (2007).

[70] M. Dennin, Phys. Rev. E **70**, 041406 (2004).

[71] J.Lauridsen, G.Chanan and M. Dennin, Phys. Rev. Lett. **93**, 018303 (2004).

[72] A. Kabla, J. Scheibert and G. Debregeas, J. Fluid Mech. **587**, 45 (2007).

[73] M. Twardos and M. Dennin, Phys. Rev. E 71, 061401 (2005).

[74] J.M. Andreas, E.A. Hauser and W.R. Tucker, J. Phys. Chem. **42**, 1001 (1938).

[75] M.E. Mobius, G. Katgert and M. van Hecke, *Submitted to Phys. Rev. Lett.*.

[76] A.J. Liu, S. Ramaswamy, T.G. Mason, H. Gang and D.A. Weitz, Phys. Rev. Lett. **76** 3017, (1996).

[77] V.J. Langlois, S.Hutzler and D. Weaire, Phys. Rev. E **78**, 021401 (2008).

[78] J. Remmers, E. Woldhuis, B.P. Tighe, M. van Hecke and W. van Saarloos, *in preparation*.

[79] J. Goyon, A. Colin, G. Ovarlez, A. Ajdari and L. Bocquet, Nature **454**, 84 (2008).

[80] W.G. Ellenbroek, E. Somfai, M. van Hecke and W. van Saarloos, Phys. Rev. Lett. **97**, 258001 (2006).

[81] I. Cheddadi, P. Saramito, C. Raufaste, P. Marmottant and F. Graner, Eur. Phys. J. E, *in press* (2008).

[82] R.J. Clancy, E. Janiaud, D.Weaire and S. Hutzler, Europ. Phys. J. E, **21**, 123 (2006).

[83] K. Krishan and M. Dennin, arXiv:cond-mat.soft/0806.3313.

[84] S. Rodts, J. C. Baudez and P. Coussot, Europhys. Lett. **69**, 636 (2005).

[85] G. Ovarlez, S. Rodts, A. Ragouilliaux, P. Coussot, J. Goyon and A. Colin, Phys. Rev. E **78**, 036307 (2008).

[86] G. Katgert, M.E. Möbius and M. van Hecke, Phys. Rev. Lett. **100**, 058301 (2008).

[87] M. Dennin, J. Phys. Condens. Matter **20**, 283103 (2008).

[88] F. Varnik, L. Bocquet, J.-L. Barrat and L. Berthier, Phys. Rev. Lett. **90**, 095702 (2003).

[89] N. Huang and D. Bonn, J. Fluid Mechanics **590**, 497 (2007).

[90] S. Timoshenko and J.N. Goodier, *Theory of Elasticity* (McGraw-Hill Book Company, New York , 1951).

[91] B. Lautrup, *Physics of Continuous Matter: Exotic and Everyday Phenomena in the Macroscopic World*, IoP Publishing (2005).

[92] S.J. Cox and E. Janiaud, Phil. Mag. Lett. **88**, 693 (2008).

[93] P. Olsson and S. Teitel, Phys. Rev. Lett. **99**, 178001 (2007).

[94] T.S. Majmudar, M. Sperl, S. Luding and R.P. Behringer, Phys. Rev. Lett. **98**, 058001 (2007).

[95] I. Cantat, N. Kern and R. Delannay, Europhys. Lett. **65**, 726 (2004).

[96] C. Raufaste, *PhD-thesis*, `http://tel.archives-ouvertes.fr/docs/00/19/32/48/PDF/TheseRaufaste.pdf` (2007).

[97] F. Lechenault, O. Dauchot, G.Biroli and J.-P. Bouchaud, Europhys. Lett. **83**, 46003 (2008).

[98] C.S. O'Hern, S.A. Langer, A.J. Liu and S.R. Nagel, Phys. Rev. Lett. **88**, 075507 (2002).

[99] T. Aste, T. Di Matteo, M. Saadatfar, T. Senden, M. Schröter and H. L. Swinney, Europhys. Lett. **79**, 24003(2007).

[100] S.F. Edwards and R.B.S. Oakeshott, Physica A **157** (1989).

[101] T. Aste and T. Di Matteo, Phys. Rev. E **77**, 021309 (2008).

[102] F. Lechenault, F. da Cruz, O. Dauchot and E. Bertin, J. Stat. Mech. P07009 (2006).

[103] A. Okabe, B. Boots, K. Sugihara and S.N. Chiu, *Spatial Tessellations: Concepts and Applications of Voronoi Diagrams* 2nd Edition. John Wiley & Sons Limited, Chichester (2000).

[104] V.A. Luchnikov, N.N. Medvedev, L. Oger and J.-P. Troadec, Phys. Rev. E **59**, 7205 (1999).

[105] T.S. Majmudar and R.P. Behringer, Nature **435**, 1079 (2005).

[106] B.P. Tighe, A.R.T. van Eerd and T.J.H. Vlugt, Phys. Rev. Lett. **100**, 238001 (2008).

[107] W.G. Ellenbroek, *PhD-thesis*, `http://www.sas.upenn.edu/wouterel/thesis.pdf`.

[108] A.S. Keys, A.R. Abate, S.C. Glotzer and D.J. Durian, Nature Physics **3**, 260 (2007).

[109] L. Berthier, G. Biroli, J.-P. Bouchaud, L. Cipelletti, D. El Masri, D. L'Hôte, F. Ladieu and M. Pierno, Science **310**, 1797 (2005).

[110] M. Toiya, J. Stambaugh and W. Losert, Phys. Rev. Lett. **83**, 088001 (2004).

[111] Y. Bertho, C. Becco and N. Vandewalle, Phys. Rev. E **73** 056309 (2006).

[112] D. Weaire, V. Langlois, M. Saadatfar and S. Hutzler, *Granular and Complex Materials*, *World Scientific Lecture Notes in Complex Systems* (eds. T. Aste, T. Di Matteo and A. Tordesillas) **8**, 1 (2007).

[113] Y. Forterre and O. Pouliquen, J. Fluid Mech. **467** 361, (2002).